

**MECHANICS OF THE CYTOSKELETON: EXAMINING  
THE DYNAMICS OF CYTOPLASMIC TRANSPORT  
THROUGH FLUORESCENCE MICROSCOPY**

Thesis by

Rajan P. Kulkarni

In Partial Fulfillment of the Requirements

for the Degree of

Doctor of Philosophy

California Institute of Technology

Pasadena, California

2006

(Defended January 18, 2006)

© 2006

Rajan P. Kulkarni

All Rights Reserved

## Acknowledgements

My research accomplishments are due in large part to the advice and support of my advisor, Scott Fraser. I would like to especially thank him for taking a chance on me and cultivating my research abilities. He gave me the freedom and independence to pursue whatever subject I found interesting, and I took full advantage of his generosity and support. Thanks to his guidance, I have been able to explore many different areas of biology and chemistry and learn an incredible amount about science and research methods.

I would also like to acknowledge my thesis committee, Professors Harry Gray, Michael Elowitz, and Mark Davis, for their support and helpful suggestions about my projects. It has been a pleasure to work with Mark Davis on aspects of polyplex transport through the cell and to work with Michael Elowitz on decision making and the significance of network design on developmental outcomes in *Bacillus subtilis*. I am also deeply grateful for Harry Gray's guidance and support on all my projects. I only hope that I can be as good of a scientist as they are.

Much of my thanks goes to members of the Fraser laboratory, my scientific home for the past three years. David Koos has been pleasurable to discuss science with. I have especially enjoyed conversations with Michael Liebling, Cyrus Papan, Julien Vermot, and Mike Tyzska. Mag Bak-Maier and I worked on the zebrafish project together, and her assistance with fish manipulation was especially helpful. David Wu's assistance with MATLAB coding on the ICS project was invaluable. Even though I only got to know Reinhard Koster as he was leaving, we were able to work together on a project; he taught me much about zebrafish and got me initially interested in that organism. A special kudos to Helen McBride; her support for me over the last three years has been absolutely invaluable. I couldn't have made it in the lab without her encouragement, advice, and support, through times both good and bad. Finalmente, muchos abrazos a Aura Keeter; era gran placer hablar con ella de varias cosas: sujetos científicos, nuestras familias, la fé, y cualquiera otra cosa que pudiera pensar.

I thank Paul Wiggins, Paul Grayson, Marianne Bronner-Fraser, and Justin Bois for helpful advice over the years. Collaborating with Arun Majumdar's group at Berkeley has been especially fruitful, especially due to the efforts of Balaji Kannan and Kenneth Castelino. I appreciate the technical assistance of Jeremy Heidel and Swaroop Mishra in the Davis lab. Swaroop was instrumental in making polyplexes and providing cells at any time. I would like to thank Gurol Suel, Chiraj Dalal, Avigdor Eldar, and David Sprinzak from the Elowitz lab for their assistance. Joe Levine – you are the MATLAB master (second only to Michael). Finally, I couldn't have begun work there without the help of Jon Young.

It has been fun to work on the resonator project with Andrea Martin. I am gratified to see her transformation from someone deathly afraid of common enzymes to learning the minutiae of protein crystallography and structure. I hope that we can continue such fruitful collaborations in the future.

I would like to thank David Copenhaver for his support and friendship over the past five years of both medical school and graduate school and for teaching me much about anatomy, medicine, and Nicaragua. ¡Qué feliz estaría si estuviera en Granada!

Finally, I am grateful to my family for their constant and unwavering support, especially during my years at Caltech. I cannot fully express my gratitude for their unconditional love and involvement. Mom, Dad, Prita – this thesis wouldn't have been possible without your encouragement.

This thesis is dedicated to the memory of Aaji and Azoba, my grandparents. This thesis represents the culmination of their dream that one of their grandchildren become a doctor. I thank them for their faith in my efforts and will continue my research in their memory.

## Abstract

The cellular cytoplasmic space contains many different molecules and complexes confined within a small volume. Understanding how objects are transported in this crowded space is important for many potential applications. In this work, we examined various aspects of cytoskeletal mechanics, including microtubule-mediated and diffusive transport using advanced fluorescence microscopy techniques. Spatio-temporal image correlation spectroscopy (ICS) was employed to first examine microtubule-mediated transport of non-viral polyplexes within endosomes through the cytoplasm. ICS analysis of these polyplex-loaded endosomes revealed that they utilized microtubule motors for intracellular trafficking and exhibited different transport behaviors for short (<10 seconds) versus long (~60 seconds) correlation times. These results indicated that, while motor biases may be present for short periods of time, resulting in a net directional velocity, the overall long term motion of the polyplexes is best described as a random walk-like process.

Multiple particle tracking (MPT) was next used to independently confirm these results. The labeled endosomes demonstrated enhanced diffusion at short times ( $t < 7$  seconds), with their mean square displacement (MSD) scaling as  $t^{1.25}$ . For longer time intervals, their MSD scaled as  $t^{0.7}$ . This crossover from an enhanced diffusion to a subdiffusive regime is explained by considering the action of motor proteins and the thermal bending modes of the microtubule network.

We then developed an assay to examine the pH characteristics of the polyplex-loaded endosomes as a function of time and distance from entry. Certain nonviral vectors, including poly-L-lysine (PLL) and cyclodextrin-containing polymers (CDP),

cannot buffer the endocytic vesicles, while polyethyleneimine (PEI), CD-PEI, and CDP-imidazole can. When combined with cell uptake and luciferase expression data, we found that there was no correlation between buffering capacity and gene expression.

Finally, we developed multi-photon fluorescence recovery after photobleaching (FRAP) to determine diffusion rates in developing zebrafish growth cones *in vivo*.

Leader growth cones had consistently longer recovery times compared to followers. This difference was abolished by perturbing the actin cytoskeleton, thus indicating that diffusion is important during axon navigation. Collectively, these findings reveal important biophysical aspects of intracellular transport that impact diverse physiological processes.

## Table of Contents

Acknowledgements.....	iii
Abstract.....	v
Table of Contents.....	vii
Figures and Tables.....	x
Chapter 1: Introduction.....	1
1.1 Introduction to the Cytoskeleton.....	1
1.2 Crowding.....	3
1.3 Transport Mechanisms.....	8
Active Transport.....	8
Diffusion.....	11
1.4 Fluorescence Microscopy Methods.....	13
Confocal Microscopy.....	13
FCS/ICS.....	15
Fluorescence Recovery After Photobleaching (FRAP).....	17
1.5 Overview of Thesis.....	20
1.6 References.....	27
Chapter 2: Quantitating Intracellular Transport of Polyplexes by Spatio-Temporal Image Correlation Spectroscopy.....	32
2.1 Abstract.....	32
2.2 Introduction.....	33
Viruses and Non-Viral Polyplexes.....	33
Image Correlation Spectroscopy.....	34
2.3 Results.....	37
Fluorescent Microsphere Images.....	37
Fluorescence Imaging of Polyplexes in HeLa cells.....	38
Spatio-Temporal ICS Analysis.....	39
2.4 Discussion.....	42
Implications of Two Fit Regimes.....	42
2.5 Conclusions.....	45
2.6 Materials and Methods.....	46
Cells.....	46
Fluorescent Microsphere Preparation.....	46
DNA Polyplexes.....	46
Fluorescence Microscopy.....	47
Theory of Spatio-Temporal ICS Analysis.....	48
Spatio-Temporal Image Autocorrelation Methods and Analysis.....	52
2.7 Appendix A: Comparison of ICS to Single/Multiple Particle Tracking Methods.....	60
2.8 References.....	69

Chapter 3: Intracellular Transport Dynamics of Endosomes Containing DNA Polyplexes Along the Microtubule Network.....	73
3.1 Abstract.....	73
3.2 Introduction.....	74
3.3 Results and Discussion.....	76
3.4 Materials and Methods.....	81
Cells.....	81
DNA Polyplexes.....	82
Fluorescence Microscopy.....	82
Multiple Particle Tracking.....	83
3.5 References.....	87
Chapter 4: Single Cell Kinetics of Intracellular, Non-Viral, Nucleic Acid Delivery Vehicle Acidification and Trafficking.....	88
4.1 Abstract.....	88
4.2 Introduction.....	89
4.3 Results.....	91
Fluorescence pH Assay.....	91
Intracellular pH Measurements.....	93
Transfection Data.....	95
4.4 Discussion.....	96
4.5 Materials and Methods.....	103
Labeled oligonucleotide.....	103
Delivery vectors.....	104
Formulation of labeled complexes.....	104
PEGylation of complexes.....	105
Cells.....	105
Fluorescence Microscopy.....	105
pH Calibration Assay.....	106
In Vitro Transfection Imaging.....	107
Plasmid uptake and expression.....	107
4.6 References.....	119
Chapter 5: Assessing <i>in vivo</i> differences in protein mobility between pioneer versus follower growth cones with multi-photon fluorescence recovery after photobleaching (FRAP).....	122
5.1 Abstract.....	122
5.2 Introduction.....	123
5.3 Results.....	125
One- and Two-Photon FRAP in Small Cellular Compartments <i>in vivo</i> .....	125
Leaders Have Slower Diffusion Kinetics than Followers.....	127
Differences Between Leaders and Followers Depend on the Actin Cytoskeleton.....	128
5.4 Discussion.....	130
Quantitative One- and Two-Photon FRAP Measurements <i>in vivo</i> .....	130
Protein Dynamics in Growth Cones.....	132

5.5 Methods.....	134
Fish Maintenance.....	134
Embryo Preparation and Pharmacological Treatments.....	134
Imaging Details.....	134
FRAP Measurements and Analysis.....	135
Two-Photon FRAP Measurements and Analysis.....	136
Data Analysis.....	137
5.6 References.....	145
Chapter 6: Conclusions.....	148
6.1 Thesis Summary.....	148
6.2 Future Directions.....	149
6.3 Concluding Remarks.....	152
6.4 References.....	153

## Figures and Tables

Figure 1.1: A Diagram of Correlation Spectroscopy .....	24
Figure 1.2: An Overview of Spatio-Temporal Image Correlation Spectroscopy .....	25
Figure 1.3: Diagram of FRAP.....	26
Table 2.1: Effective Diffusion Coefficients and Velocity Values for Selected Nonviral Polyplexes.....	54
Figure 2.1: Chemical Structures for $\beta$ -CD and PEI.....	55
Figure 2.2: Temporal Image Correlation Analysis of 200 nm beads in glycerol.....	56
Figure 2.3: Two Trajectories of 100-nm PEI Polyplexes.....	57
Figure 2.4: An Example of Temporal ICS Analysis of Intracellular Polyplexes.....	58
Figure 2.5: The Effects of Nocodazole on Intracellular Directed Transport.....	59
Figure S1: Histogram of Number Density of Microspheres.....	64
Figure S2: Plot of Average MSD for 100-nm PEI Particles.....	66
Figure S3: Plot of D vs. S/N ratio for ICS and MPT.....	67
Figure S4: Plot of D vs. Number of Images Analyzed for ICS and MPT.....	68
Figure 3.1: Plot of MSD of Polyplex-Loaded Endosomes as Function of Time Lag....	84
Figure 3.2: Cartoon of Thermal Bending and Deformation of MT Network.....	85
Figure 3.3: Schematic of Particles Embedded in MT Mesh.....	86
Figure 4.1: Fluorescence Spectra of SNARF-4F dye.....	109
Figure 4.2: Average Diameters of Particles Used.....	111
Figure 4.3: Images of PLL Particles in Cell.....	112
Figure 4.4: Schematic of Cell Depicting Regional Analysis.....	114
Figure 4.5: Plot of Average pH of all Cells and Regions as Function of Time.....	115
Figure 4.6: Regional pH Values as Function of Time and Region.....	116
Figure 4.7: Gene Delivery Efficiency for Particles Used.....	117
Figure 4.8: Measure of DNA Uptake for Each Type of Particle.....	118
Table 5.1: GFP Diffusion Rates in Different Compartments and Growth Cones... ..	139
Table 5.2: GFP and YFP-actin Recovery Rates for Leaders and Followers.....	140
Figure 5.1: Single- and Two-Photon FRAP Analysis.....	141
Figure 5.2: Further Examples of FRAP Experiments.....	142
Figure 5.3: Fluorescence Recovery Traces for one- and two-photon FRAP.....	143
Figure 5.4: Measurement of Diffusion in Growth Cones.....	144

## **Chapter 1: Introduction**

### **1.1 Introduction to the Cytoskeleton**

The cytoplasm of any given eukaryotic cell contains thousands of different enzymes, molecules, organelles, and other factors required for growth and maintenance of cell viability. For example, the enzymes range from heat shock proteins involved in protecting the cell from environmental damage to the cytochrome enzyme complexes that are used for the generation of cellular energy in the form of adenosine triphosphate (ATP). The small molecules include charged ions, such as sodium or calcium cations, or neutral molecules like glucose, which are important as enzyme cofactors or as energy sources. Organelles within the cell compartmentalize cellular functions and keep reactive species (such as oxygen radicals in the mitochondria) from interacting with other structures. All these factors work in concert to ensure that the cell remains viable. In many cases, diverse interactions between enzymes allow the cell to sample its environment, adapt to changing conditions, and perform physiological functions.

The cell's cytoskeleton is one of the most important components for performing these functions and maintaining viability. The cytoskeleton provides shape and internal structure and allows the cell to move through its environment. It separates the chromosomes during mitosis and allows the two daughter cells to split apart, and it allows for intracellular trafficking of organelles and endosomes, shuttling materials from one location to another. As an example of the cytoskeleton's importance, progressive cell collapse and death can occur if it is significantly perturbed.

The diverse functions of the cytoskeleton depend on the activities of three families of protein molecules that polymerize to form filaments within the cytoplasm. Intermediate filaments, often composed of monomers of vimentin or keratin, help to impart the cell with tensile strength and resistance to deformation. Actin filaments (also called microfilaments), composed of monomers of actin, allow the cell to explore its local environment and are necessary for long-range cell movements. Microtubules, which consist of tubulin heterodimers, are critical for intracellular transport of endosomes and other organelles and for segregating chromosomes during cell division. In addition, there are a number of accessory proteins that are required for modulating the activity of these filamentous networks, which include the motor proteins that allow objects to move along these networks.

These cytoskeletal networks undergo rapid and dynamic changes that allow the cell to rapidly adapt to its environment. Each is composed of individual protein subunits polymerized into long filaments, arranged in large helical assemblies through noncovalent interactions (both hydrogen bonds and van der Waals forces) between the subunits. Because such linkages are weak compared to covalent bonds, the individual protein subunits can rapidly assemble and disassemble from the filament [1]. Additionally, both actin filaments and microtubules have distinct polarities, with subunits preferentially adding at the plus end and leaving from the minus end due to ATP or GTP hydrolysis. This asymmetry can result in treadmilling, whereby the filament maintains a constant length but subunits are constantly added to the plus end and hydrolyzed from the minus end at the same rate, or dynamic instability, in which rapid disassembly of the polymer occurs at the minus end due to nucleoside triphosphate hydrolysis [1]. Such

cytoskeletal dynamics allow the cell to rapidly liberate actin or tubulin subunits in order to quickly respond to changing environmental conditions.

Cells have evolved complex and intricate mechanisms for regulating cytoskeletal assembly and for using these networks for internal transport. The diversity of forms and functions of these networks is regulated by many accessory proteins that can sequester free subunits or bind to the ends of the filaments themselves, or are motor proteins that transport cargo (described in more detail in section 1.3). The dynamics of polymerization and depolymerization and the function of motor proteins fundamentally affect processes including intracellular transport and cell motility. Molecules and objects within the cell must navigate these networks in order to reach their final destinations. Understanding the dynamics of the cytoskeleton and the cytoplasm is therefore important for elucidating mechanisms for cell viability and intracellular transport for applications as diverse as drug delivery to creating artificial cell grafts.

## **1.2 Crowding**

Intracellular biochemical reactions occur in an environment that is crowded with proteins, macromolecular complexes, small solutes, and organelles. The concentration of each macromolecular species within the cytoplasm can vary widely; collectively, these species occupy anywhere from 20-30% of the total cellular volume [2-5]. Within this environment, certain proteins (actin, tubulin, and intermediate filament protein subunits) can form long filamentous networks in the cell. These networks allow the cell to transport endosomes and other objects throughout the cytoplasm; however, they also create transient and permanent barriers to free diffusion and can result in localized

compartments in which macromolecular species can become concentrated, thus raising their effective localized concentrations and activities [5-8].

Given all these species and complexes within the cytoplasm, we can estimate the average mesh size of a typical eukaryotic cell with a diameter of 20  $\mu\text{m}$ . If macromolecules comprise approximately 25% of the total cellular volume, this would lead to a mesh spacing of roughly 25-30 nm, using an average protein diameter of 27 nm<sup>3</sup> [2, 9]. Certain areas of the cell may be more or less crowded than this, depending on the concentration of macromolecules present. In general, objects larger than 30 nm cannot freely diffuse in the cytoplasm but rather must be transported along the actin or tubulin networks in order to move about the cell (see section 1.3 for more details). This crowding results in perturbations of the rates and equilibria of macromolecular interactions and of diffusion and transport kinetics.

In the cytoplasm, nonspecific interactions between macromolecular solutes (due to proximity) add to the total free energy of the system and can affect enzymatic reaction rates and activities. Such nonspecific interactions, which can be either repulsive or attractive, do not necessarily depend on the specific primary or secondary structure of the proteins but rather on their global properties, including net charge, dipole moment, surface polarity, and overall protein shape [5].

Macromolecular crowding impacts reaction rates because of steric repulsion between large molecules. Because proteins are 2 nm or larger in diameter, they occupy a certain volume in the cytoplasm. Other molecules cannot physically occupy the same space because they will be repelled as they approach too close. Such repulsion creates an excluded volume which limits the locations that other proteins in the cell can inhabit.

This steric exclusion can result in localized concentrations of certain molecules in more open areas of the cell and increased or decreased rates of biochemical reactions, depending on the specific circumstances [10-13]. For example, Lindner and Ralston found that the rate of spectrin self-association was increased ten-fold in a crowded dextran solution [14]. However, most classical biochemical studies have been performed in buffered solutions, where the concentration of macromolecules is very dilute. Although these classical experiments do yield qualitative information about protein activities, we would ultimately like to know how such species behave in their native environment, the cytoplasm.

The porous nature of the cytoskeleton and the differing sizes of macromolecules within the cytoplasm have significant implications when considering the effects of volume exclusion. For a region containing a known quantity of macromolecules in a confined environment, the volume available to a distinct, spherical test molecule is defined as the fraction of the total space that can be occupied by the center of mass of the test molecule [5]. The molecules already present can undergo nonspecific interactions as described and experience steric repulsion with each other; they are not too closely packed, and there is some space in between neighboring molecules. If the test molecule is small relative to the species already present in the crowded space, then it can access most of the “free” space, space that contains no macromolecules. However, if the test molecule is of comparable size or larger, then the volume that it can occupy is significantly reduced because the center of this molecule cannot fit in between the small spaces created by the macromolecules due to steric repulsion and the incompressibility of the molecules already present. As a result of this crowding effect, the available effective

volume for each molecule can be significantly reduced, thus raising its effective activity and chemical potential [5, 8, 15, 16]. We can account for the effects of volume exclusion by calculating the nonideal contribution to the total chemical potential ( $\mu$ ) of a given species  $i$  [2]:

$$\mu_i = \mu_i^{ideal} + \mu_i^{nonideal} . \quad (1)$$

The ideal contribution is what we classically expect for the chemical potential in the absence of crowding or volume exclusion effects:

$$\mu_i^{ideal} = \mu_i^0 + kT \ln c_i , \quad (2)$$

where  $c_i$  is the concentration,  $\mu_i^0$  is the standard chemical potential,  $k$  is Boltzmann's constant, and  $T$  is the temperature.

The nonideal contribution is the change in free energy due to the interaction of a molecule of species  $i$  and all other molecules in solution

$$\mu_i^{nonideal} = kT \ln \gamma_i , \quad (3)$$

where  $\gamma_i$  is the activity coefficient of the molecule.

These can be combined to yield

$$\mu_i = \mu_i^0 + RT \ln a_i , \quad (4)$$

where  $a_i = \gamma_i c_i$  is an effective concentration called the thermodynamic activity.

In very dilute solutions, the assumption that  $a_i = c_i$  generally holds because of the absence of many solute-solute interactions. However, in crowded or concentrated solutions, this is no longer true and the nonideal contribution (through  $\gamma_i$ ) must be properly considered, and the volume exclusion can increase the activity of certain species by orders of magnitude [2].

This increase in solute activity generally favors macromolecular association and increases reaction rate. Equilibrium constants can increase by as much as three orders of magnitude, depending on the shape factors of the species involved [2]. For instance, Rivas et al. have shown that the activity coefficient of fibrinogen is ten times higher in a solution of 80 g/L of bovine serum albumin compared to buffer, implying that the activity of fibrinogen in its native environment (blood plasma) is greater than classically understood [17]. Similar effects have been seen for other systems, including multimerization of proteins and hemoglobin activity [18-20].

An important consequence of macromolecular crowding is the reduction of diffusion rates, especially for larger proteins. It is estimated that the diffusion constants of proteins within the cytoplasm (such as green fluorescent protein, GFP) are reduced anywhere from three to ten-fold or more compared to their diffusion constants in pure water [3, 21, 22]. Furthermore, such crowding can effectively reduce the dimensionality of diffusion, especially in long, narrow cytoplasmic structures in which the cell membrane or an organelle presents an impassable barrier to motion in certain directions. These structures can limit the degrees of translational motion available to a given species and therefore constrain diffusion to a two or even one-dimensional process. In such narrow and crowded structures as developing neuronal axons or growth cones, such restrictions and barriers to diffusion must be considered in order to properly understand how protein trafficking can affect growth and development rates.

Cells have clearly evolved mechanisms to adapt to and perhaps even exploit their crowded environments in order to carry out basic functions. The presence of such diffusion restrictions and other corral-like structures in the cell can actually increase rates

of reaction and assist the cell in carrying out biochemical reactions and functions as discussed. Indeed, further investigations by Rivas et al. have shown that crowding by dextran increases oligomerization of tubulin [19], while Drenckhahn et al. have demonstrated that the formation of filamentous actin is accelerated in the presence of crowding agents [23]. Similarly, Minton has indicated that crowding may increase the rate of protein folding [7].

In prokaryotic cells, diffusion is the main method for protein and macromolecular transport within the intracellular space. However, eukaryotes have evolved a number of ways to overcome the slow rates of diffusion that the crowded environment imposes, especially for large objects ( $> 20$  nm), which are discussed in the following section.

### **1.3 Transport Mechanisms**

#### **Active Transport**

There are a number of mechanisms for transport within the cytoplasm. Free diffusion, discussed in detail below, is generally limited to small inorganic and organic molecules and proteins, since the cytoskeleton forms a mesh with spacing of roughly 30 nm. Small proteins such as GFP can freely diffuse through the cytoplasm, albeit more slowly than in pure water because of increased intracellular viscosity [9, 24-26]. Large complexes, such as macromolecular clusters, viruses, or organelles, cannot freely diffuse and must be transported in vesicles in order to move about the cell in a timely manner. For such transport, the actin and tubulin networks are necessary [1].

Actin and tubulin are present in the cytoplasm as globular, individual proteins as well as polymerized filaments. The dynamics of polymerization and depolymerization of

these filamentous networks is discussed in Section 1.1. Both actin filaments and microtubules have a polarity, with subunits preferentially added to the plus ends in a nucleoside phosphate-dependent manner and hydrolyzed from the minus ends. These processes are controlled by the cell for locomotion and division [27, 28]. Rapid turnover of the actin network is used by the cell to alter its shape; a similar process with microtubules is used to arrange chromosomes during cell division [1].

In addition to these global movements, localized transport of vesicles and other organelles along either network can occur with the assistance of the respective actin- and microtubule-associated motor proteins, myosin and kinesin/dynein. These motor proteins share certain features; they are all two-headed processive motors, in that they proceed one step at a time along the appropriate network. The motors can take hundreds of steps each before pausing and falling off the filament. They also walk in a hand-over-hand mechanism [29-31] and utilize ATP as their energy source.

Cells contain many different isoforms of each of the motor proteins. Myosin II, present in muscle cells, can form large aggregates due to interactions in the tail regions of individual subunits. These aggregates are responsible for force generation in muscle [1]. However, the form of myosin responsible for cytoplasmic transport, myosin V, does not form such structures. Similarly, there are diverse isoforms of kinesin and dynein. Most of these forms are involved in vesicle or organelle transport along microtubules.

Although vesicles can be transported by myosin V along the actin network, it is significantly more likely that such transport will occur along the microtubule network using kinesin or dynein motors [1]. The kinesin motors move objects in an anterograde (away from the nucleus) direction, while the dynein motors move cargo in a retrograde

fashion [1, 32]. Though the kinesin motor can attach to cargo without the assistance of any other factors, dynein requires the presence of a large protein complex called dynactin in order to be coupled to its cargo.

Typical vesicles have both kinesin and dynein along their surfaces and can thus travel along microtubules in both directions; this can lead to interesting behavior whereby the vesicle oscillates back and forth about a point due to alternating activity between the two motors. However, in many cases, when attached in series to a vesicle, the motors function cooperatively and processively to travel multiple steps in sequence in a single direction; such cooperativity allows the vesicle to be transported in a directed manner [29]. The distance that the vesicle can travel before stalling or reversing depends on the characteristics of each of the motors. Recent single molecule studies of myosin V, kinesin, and dynein have found that the individual molecular step sizes under load are 36 nm, 8 nm, and 8 nm, respectively [30, 31, 33, 34], with each motor able to take approximately one hundred steps before stalling.

Though vesicles and organelles can be transported from one end of a cell to another at velocities of up to 2  $\mu\text{m}/\text{second}$ , the exact mechanism for how the motors cooperate to allow transport at these rates is still unknown. Vesicles containing different types of motors can nonetheless exhibit biases to move preferentially in one direction; perhaps phosphorylation or another regulatory activity helps to silence certain motors or enhance others. There is much interest in understanding the mechanics of cytoplasmic transport in order to optimize delivery of exogenous agents and to potentially control cell behaviors.

**Diffusion**

Small species (< 20 nm) in the cytoplasm can fit in between the mesh spaces of the cell and therefore do not require motor transport in order to move through the cytoplasm. Instead, such species undergo random Brownian motion. Brownian motion occurs because all molecules have an internal thermal energy directly proportional to the external temperature. This thermal energy causes molecules suspended in a solution to bounce about and constantly collide with other molecules. These collisions mean that molecules travel through a solution in a random walk fashion, with a complex and tortuous path. Because such motions are random, we cannot predict where a given molecule will be at a precise moment [1]. However, we can determine the location probability distribution of a group of molecules, assuming that they started at a known position. This distribution can be mathematically described by Fick's first law of diffusion, which states that the rate of diffusion of molecules from one place to another is proportional to the concentration difference between the two locations:

$$J_x = -D \frac{dN}{dx}, \quad (5)$$

where  $J_x$  is the flux of molecules (the number that go through a given unit area per second),  $D$  is the diffusion constant for the molecule (see below),  $N$  is the number of molecules per unit volume, and  $x$  is the distance over which the molecules travel.

Within the cell, crowding reduces the average mean free path of the molecules (the distance that a molecule can travel before colliding with another molecule), and proteins or small solutes will often encounter many other species in the process of diffusing through the cell [15, 16, 21]. Such interactions will affect the time and path that these molecules actually take. The mobility of a species can be found by calculating the

diffusion constant. The diffusion constant is related to the size of the molecule and the viscosity of its solution through the Stokes-Einstein equation:

$$D = \frac{kT}{6\pi\eta r}, \quad (6)$$

where  $k$  is Boltzmann's constant,  $T$  is the temperature,  $\eta$  is the viscosity of the solution, and  $r$  is the hydrodynamic radius of the particle.

The size of the molecule and the solution viscosity play important roles in determining the diffusion characteristics. The hydrodynamic radius of the molecule represents the size of the molecule after it has been surrounded by its hydration shell of water. There can be many water molecules surrounding charged molecules, thus significantly increasing the hydrodynamic radius relative to the molecule's actual radius. The solution viscosity represents how "thick" the solution is, or rather how difficult it is for other molecules to diffuse through. Notably, intracellular crowding can hinder diffusion by increasing the net viscosity. There is still some debate as to the exact contribution that cytoplasmic crowding makes to intracellular viscosity. Verkman has found that, for small species, the cytoplasm behaves almost as if it were a water solution [9, 25]. However, others have found that the presence of other proteins, macromolecules, and organelles significantly increases the net effective viscosity relative to pure water [35, 36]. The exact quantitative change on viscosity evidently depends on the nature of the molecule and the type of cell being studied.

## **1.4 Fluorescence Microscopy Methods**

### **Confocal Microscopy**

Confocal microscopy, first invented by Marvin Minsky almost fifty years ago, represents a significant advance over standard brightfield or fluorescence microscopy. This type of microscopy allows for visualization of deep intracellular structures and the construction of three-dimensional images by capturing optical stacks of a given sample. Confocal microscopy uses adjustable pinholes, placed in front of the detection element, to reject out-of-plane light (and hence out-of-focus light) and create virtual optical sections. The resolution and depth of these optical sections is determined by the properties of the microscope optics, including the type and quality of objective lens used, and the size of the pinhole. By reducing the size of the pinhole, more out-of-focus light can be rejected, resulting in sharper images with fine details illustrated.

Most contemporary applications of confocal microscopy involve the imaging of fluorescent molecules (called fluorophores) within cells or other biological systems. In ordinary fluorescence microscopy, it is difficult to distinguish the subcellular localization of fluorophores within a cell because the microscope collects fluorescence from all optical planes in the sample. With confocal microscopy, fluorescence localized to specific organelles or regions within a cell can easily be identified and separated as long as the specimen is sufficiently thin. Furthermore, it is relatively facile to reconstruct a virtual three-dimensional representation of the cell by scanning through the different focal planes of the sample. The advent of inexpensive, fast computers and ultrasensitive photomultiplier tubes (the component of the microscope that detects the fluorescence light) has allowed for rapid image collection and capture of rapid cellular events in real

time. Complex intracellular dynamics can be imaged using fast time-lapse confocal microscopy.

The typical, commercially available confocal microscope consists of the microscope body, the laser scan head (which also contains the optics components, pinhole, and photomultiplier tubes), a controller unit, and a computer to process and display the images. Images are generated by scanning a laser of given wavelength through the sample. The x-y direction scanning is performed by directing the laser beam with a precisely controlled scan mirror placed between the dichroic mirror and the objective lens of the microscope. The dichroic mirror is designed to reflect certain wavelengths and transmit others. In the confocal microscope it ensures that the incident laser light only interacts with the sample and does not return to the detector; the dichroic only allows fluorescent light of the desired wavelength to pass to the detector element. The laser light interacts with fluorophores in the sample, and the resulting fluorescence light is passed through the dichroic mirror to an emission filter (to eliminate any stray laser light that may have passed through) before encountering a variable pinhole in front of the photomultiplier tube (or other type of detector). More or less fluorescence light from the sample is allowed to pass through to the detector by adjusting the size of this pinhole, which modulates the effective depth of the optical field. The actual thickness of the z-section is determined by the numerical aperture of the objective lens, the wavelength of laser light, and the size of the pinhole.

In addition to capturing detailed static images, the confocal microscope can be used for advanced quantitative imaging techniques. Advanced electronic controls within the confocal controller unit (such as the acousto-optical tunable filter for very rapidly

modulating laser intensity) allow the user to quickly switch between different lasers or attenuate the illumination profile when scanning through the sample. This ability to vary the properties of the excitation light in milliseconds allows for advanced techniques such as image correlation spectroscopy (ICS) or fluorescence recovery after photobleaching (FRAP) to be performed with the confocal microscope, as described below.

### **Fluorescence Correlation Spectroscopy (FCS)/Image Correlation Spectroscopy (ICS)**

As part of this study, we have replicated spatio-temporal ICS and determined the relevant parameters to analyze various aspects of cytoskeletal dynamics *in vivo*. ICS, as first described by Petersen et al. [37], is a spatial corollary to fluorescence correlation spectroscopy (FCS). FCS, as initially detailed by Magde et al. [38-40], involves measuring the fluctuations in the fluorescence signal as molecules pass through a fixed laser beam; dynamic information can then be obtained from these fluctuations by calculating the autocorrelation function  $G(\tau)$  to obtain a statistical average of the environment (see Figure 1.1). The autocorrelation function is plotted as a function of the time lag,  $\tau$ , and then fit with the appropriate functional equation (i.e., diffusion equation, flow equation, and so forth) to obtain quantitative dynamical information about the system.

FCS has recently been utilized to measure diffusion constants of small proteins both in the cell membrane and cytoplasm [41-44]. It works well for small proteins that can freely diffuse through the probe volume and for rapid processes occurring on the microsecond to millisecond time scale. However, not all cellular processes occur on such

a rapid time scale; for example, the viruses and non-viral polyplexes examined in this thesis perceptibly travel through the cytoplasm on the order of seconds to minutes. FCS would not be useful for examining these particular processes (or anything else that occurred on similar time scales) because the samples would be photobleached before any dynamic information could be obtained. Instead, ICS is a suitable alternative technique for measuring physical processes that occur on these time scales.

In ICS, a scanning laser beam (usually within a standard confocal microscope) is used to generate an image of a given cell or region and to simultaneously measure the fluorescence intensities of objects within the image, as depicted in Figure 1.2 [37, 45, 46]. The intensity information from each pixel in the image is then used to calculate the both the spatial and temporal autocorrelation functions. The spatial intensity fluctuations are calculated by choosing one pixel in the image and then multiplying the intensity of that pixel by every other pixel in the image as a function of the distance (in both x- and y-dimensions) from the original pixel. By repeating this process for every pixel in the image, as a function of  $\Delta x$  and  $\Delta y$  (which is simply the distance of the new pixel from the pixel originally chosen), we can then find the average intensity values, which can then be used to generate the autocorrelation functions. The spatial autocorrelation curve is then plotted as  $g(\Delta x, \Delta y)$  versus  $\Delta x$  and  $\Delta y$ . The temporal intensity fluctuations are calculated for each pixel in the time-resolved image series and then averaged to obtain the temporal autocorrelation function (full mathematical details for all calculations are given in section 2.6). Similar to FCS, the temporal autocorrelation curve is plotted separately as  $g(\tau)$  versus  $\tau$ .

The spatial autocorrelation curve can be fit to determine the laser beam radius and the number of fluorescent objects in each image (also called number density). The temporal autocorrelation curve can be fit with similar equations as described for FCS to determine diffusion and flow information. ICS allows us to obtain such information about an entire image plane rather than just for a fixed point as for FCS. Additionally, ICS can provide quantitative information about objects smaller than the optical diffraction limit; however, such objects must be identifiable as discrete puncta for optimal performance. A major benefit of this technique is that it provides information about aggregate behavior in a region of interest by measuring statistical fluorescence fluctuations.

Recent studies have used ICS to determine the number of receptors on a cell surface and their degree of aggregation [47-49]. These original implementations of ICS did not include a temporal component. More recently, Srivastava et al. and Wiseman et al. have described combined temporal and spatial autocorrelations; however, they have been primarily applied to model bead systems [50, 51], though they suggested that it could be extended to analyze cytoplasmic dynamics. In principle, spatio-temporal ICS is not limited to these systems and can be useful for determining intracellular properties; indeed, we have successfully extended this methodology for intracellular imaging studies (see below and Chapter 2).

### **Fluorescence Recovery after Photobleaching (FRAP)**

A complementary method for determining intracellular kinetic diffusion parameters is fluorescence recovery after photobleaching (FRAP). In a typical FRAP

experiment, the object of interest is scanned at low laser intensity to acquire background fluorescence values; then, a specific region is rapidly illuminated with a pulse of focused, high-intensity laser light (Figure 1.3). The aim of this brief high intensity pulse is to cause the fluorophores within that volume to irreversibly lose their fluorescence, a process known as photobleaching. Following the bleach, the laser is switched back to low intensity (as before the bleach pulse) so that the recovery of unbleached fluorophores from surrounding regions diffusing into the bleached area can be measured. The data can then be analyzed qualitatively by comparing recovery curve profiles among different experimental conditions. Additionally, using models developed by Axelrod and others [52-54], it is possible to measure the diffusion coefficient and mobile fraction of the fluorescent species in the sample. The major benefit of FRAP is that the bleach region can be determined by the experimenter based on the geometry of the cell [55, 56]. Since FRAP measures changes in fluorescence intensities, it can be used in cells where the fluorophores are not spatially distinct, such as in cells where GFP is constitutively expressed within the cytoplasm. Thus, FRAP is highly versatile, allowing both qualitative and quantitative information to be obtained about kinetic processes.

Initial biological applications of FRAP involved measuring lateral diffusion of lipids and proteins within cell membranes. The discovery of green fluorescent protein (GFP) and its use to non-invasively tag molecules throughout the cell has vastly increased the use of FRAP as a means to measure intracellular protein dynamics. The behavior of these GFP-tagged molecules can easily be examined using modern microscopic equipment. In addition, fluorescent proteins alone can be used as reporters of diffusion in different cellular compartments or during specific cell behavior. An added

advantage is that unlike the previously employed dyes which had to be injected but bleached quickly, the fluorescent proteins are more photostable and can be introduced noninvasively. They also enable examination of cellular processes in more complex tissues as well as within whole organisms.

The vast majority of FRAP experiments to date have employed traditional one-photon lasers at high intensities (i.e., Ar ion laser). However, one drawback of traditional one-photon FRAP lies in the conical excitation profile that is created by the beam focusing elements. Although the laser intensity is focused to a point, there is still notable light radiation throughout the illumination cone. Because of the increased laser intensity required for the bleach pulse, molecules within this cone will be bleached in addition to molecules in the focal plane, thus reducing the apparent diffusion coefficient and recovery fractions in one-photon FRAP.

One solution to this problem lies in the use of two-photon excitation. Two-photon excitation microscopy relies on the principle that two photons, absorbed nearly simultaneously by a fluorophore, can produce an excitation equivalent to the absorption of one photon of twice its energy. The probability of two-photon absorption is greatest at the focal point and decays so rapidly that there is no appreciable fluorescence at any other plane. Hence, there is minimal bleaching in out-of plane regions; two-photon microscopy also allows for cells and tissues in much deeper regions to be sampled<sup>1</sup>. Thus, using two-photon FRAP we are able to derive more precise kinetic and quantitative information about the nature of the species of interest *in vitro* and *in vivo*.

---

<sup>1</sup> Another feature of two-photon non-linear excitation is the ability to potentially excite multiple fluorophores with a single wavelength. For example, GFP, CFP, and YFP can all be simultaneously excited at 900 nm because of the broad two-photon absorption profile of these three proteins. This effect can be avoided by choosing different excitation wavelengths.

## 1.5 Overview of Thesis

The main goal of this thesis was to explore the dynamics of the cytoskeleton with regards to transport processes, including both diffusion and active transport involving microtubules and their associated motors. Specifically, we wanted to quantitatively examine how cells overcome the limitations imposed by crowding and are able to transport objects within endosomes to various cytoplasmic locations by measuring the velocity and pH kinetics of these endosomes over time. We also wanted to quantify the rates of diffusion of small proteins in zebrafish neuronal growth cones (a very small and crowded compartment) *in vivo* and determine which cytoskeletal processes might affect these diffusion rates. Understanding the dynamics of these processes will aid in designing therapeutics that can overcome kinetic barriers in endosome delivery and will facilitate our knowledge of how macromolecular crowding affects biochemical processes *in vivo*.

This chapter has provided a brief overview of the concepts of macromolecular crowding and microtubule-mediated active transport processes and of the microscopy techniques that were utilized for these studies. In Chapter 2, we describe how image correlation spectroscopy was applied to measure the kinetics of endosome trafficking of non-viral polyplexes traveling towards the nucleus. Specifically, we quantitated the velocities and diffusive-like behavior of these endosome-enclosed polyplexes through the cytoplasm. We found that the polyplexes displayed two distinct types of behaviors as they traveled through the cytoplasm, with overall rates of transport relatively slow. At short correlation times (<10 seconds) the polyplexes were transported with a net directional velocity, while at longer correlation times they were transported in a random

walk-like process. These behaviors can be explained by a memory effect of the microtubules that is lost at long correlation times. These data show that ICS is a powerful tool for quantitating transport parameters in real time in biological systems.

We then wanted to further explore the interesting microtubule-mediated dynamics of these polyplexes in terms of the mechanics of the microtubule motors and thermal contributions to transport. Chapter 3 details the microtubule-mediated transport of these endosome-enclosed polyplexes. The endosomes were tracked using multiple particle tracking to determine the individual and average mean squared displacements (MSD). From these measurements, we found that the MSD scaled as  $t^{1.25}$  at times less than seven seconds, while the MSD scaled as  $t^{0.7}$  at longer times. This crossover from enhanced diffusion to a subdiffusive regime can be explained by considering the processivity of the kinesin and dynein motors and the thermal bending modes of the microtubule network itself. At short times, the external driving force provided by the motors is highly correlated and results in the enhanced diffusion regime. At longer times, the motor activities are uncorrelated, which leads to the subdiffusive regime. Since the endosomes are not completely entrapped in the microtubule mesh, thermal effects modulate the time exponents. This model of endosome motion along microtubules can explain transport of many intracellular objects.

Since it takes many hours for the polyplexes to reach the nucleus from the cell membrane, and there is little indication that these polyplexes even escape the endosomes, we wondered about the pH kinetics of the endosomes as the polyplexes were trafficked through the cytoplasm. Chapter 4 describes a novel assay that was developed to measure pH kinetics *in vivo* and relates our findings. From these studies we identified that the

labeled polyplexes were indeed enclosed within endosomes, as we could track endosome acidification over time. Additionally, we found that certain polyplex types could buffer better than others, but that buffering capability did not correlate very strongly with gene uptake or expression. Certain polyplexes that had high gene expression did not buffer the endocytic compartment well. It therefore appears that endosomal pH is not the major factor that determines polyplex escape or gene delivery and that there are other barriers to delivery that must first be overcome. These findings will have significant implications for the design of newer polycations for gene delivery.

The diffusion of green fluorescent protein (GFP) was examined in various regions of developing zebrafish neurons *in vivo* using FRAP; these experiments are described in Chapter 5. We developed and enhanced multi-photon FRAP methods to accurately measure these rates of diffusion *in vivo*. The initial goal was to quantify the rates of diffusion in various types of neuronal growth cones (leaders, followers, off-tract followers). However, we found that diffusion was consistently slower in leaders and off-tract followers than for followers. Furthermore, these differences were found to be modulated by the actin network. Depolymerization of the actin network using cytochalasin caused these diffusion differences to be abolished, while disrupting the microtubule network had little effect on diffusion kinetics. These results suggest that the actin network creates a mesh with a given pore size and that this pore size might be important for mobility and dynamic organization within the cell. Leader neurons, which display slower diffusion rates, might have smaller pores, which would temporally increase local concentrations of proteins and signaling molecules. Such temporal effects may be significant for proper cellular navigation and development of the embryo. These

results provide an important step towards our ability to observe and measure such biophysical processes within developing organisms.

Finally, Chapter 6 summarizes the work presented in this thesis and concludes with an overview of possible future experiments that might be undertaken based on the results presented here.

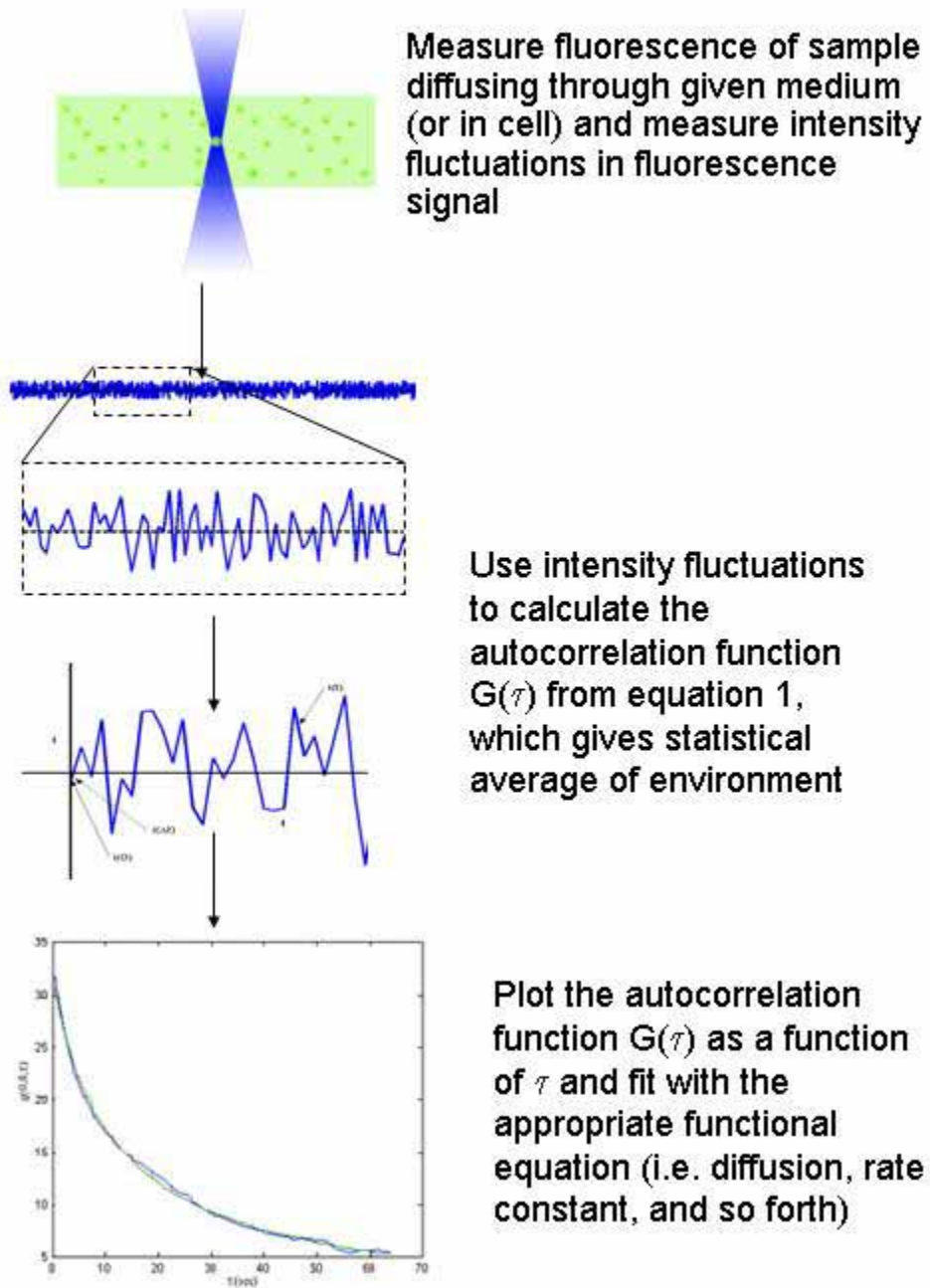
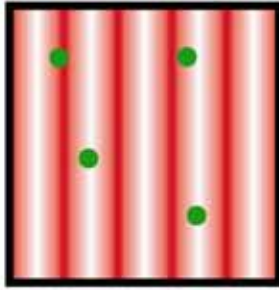
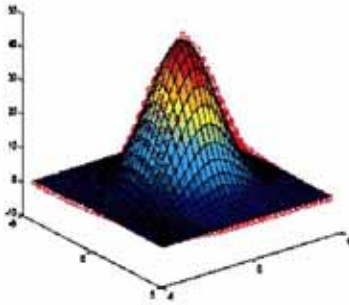


**Figure 1.1:** A diagram of correlation spectroscopy.



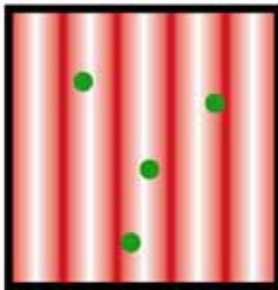
Scan entire image and measure pixel intensities.

Compute spatial intensity fluctuations by multiplying intensity of each pixel by every other pixel in the image. Find average values as a function of  $\Delta x$  and  $\Delta y$ .



Generate autocorrelation curve. Autocorrelation curve is plotted as  $g(\Delta x, \Delta y)$  versus  $\Delta x$  and  $\Delta y$ .

Fit spatial autocorrelation curve to find beam radius and number density.



Can repeat process for every image in a time series.

Can also perform temporal autocorrelation to determine dynamic information.

**Figure 1.2:** An overview of spatio-temporal image correlation spectroscopy.

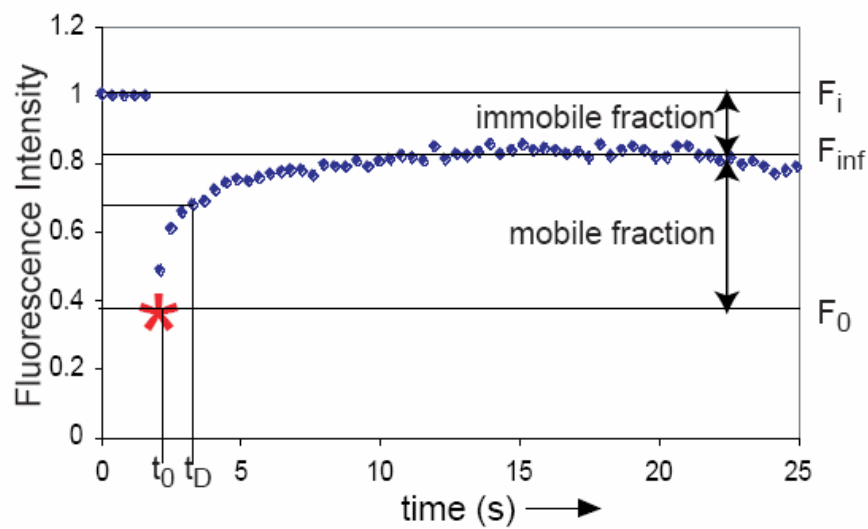
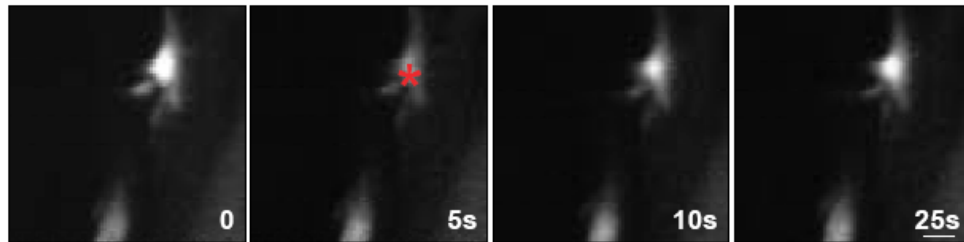
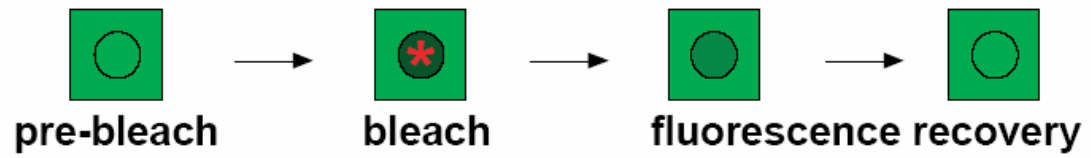


**Figure 1.3:** Diagram of FRAP. A region within a zebrafish neuron (indicated by a star) is photobleached at time  $t_0$ ; the fluorescence decreases from  $F_i$  to  $F_0$ . The characteristic diffusion time  $t_D$  indicates the time at which half of the fluorescence has recovered (to the maximal value at  $F_{inf}$ ). The mobile and immobile fractions are indicated.

## 1.6 References

1. Bray, D., *Cell Movements: From Molecules to Motility*, 2nd edition. 2001.
2. Ellis, R.J., *Macromolecular crowding: obvious but underappreciated*. Trends Biochem Sci, 2001. **26**(10): p. 597-604.
3. Ellis, R.J., *Macromolecular crowding: an important but neglected aspect of the intracellular environment*. Curr Opin Struct Biol, 2001. **11**(1): p. 114-9.
4. Ellis, R.J. and A.P. Minton, *Cell biology: join the crowd*. Nature, 2003. **425**(6953): p. 27-8.
5. Minton, A.P., *The influence of macromolecular crowding and macromolecular confinement on biochemical reactions in physiological media*. J Biol Chem, 2001. **276**(14): p. 10577-80.
6. Hall, D. and A.P. Minton, *Macromolecular crowding: qualitative and semiquantitative successes, quantitative challenges*. Biochim Biophys Acta, 2003. **1649**(2): p. 127-39.
7. Minton, A.P., *Influence of macromolecular crowding upon the stability and state of association of proteins: predictions and observations*. J Pharm Sci, 2005. **94**(8): p. 1668-75.
8. Minton, A.P., *Models for excluded volume interaction between an unfolded protein and rigid macromolecular cosolutes: macromolecular crowding and protein stability revisited*. Biophys J, 2005. **88**(2): p. 971-85.
9. Seksek, O., J. Biwersi, and A.S. Verkman, *Translational diffusion of macromolecule-sized solutes in cytoplasm and nucleus*. J Cell Biol, 1997. **138**(1): p. 131-42.
10. Hall, D. and A.P. Minton, *Effects of inert volume-excluding macromolecules on protein fiber formation. I. Equilibrium models*. Biophys Chem, 2002. **98**(1-2): p. 93-104.
11. Hall, D. and A.P. Minton, *Effects of inert volume-excluding macromolecules on protein fiber formation. II. Kinetic models for nucleated fiber growth*. Biophys Chem, 2004. **107**(3): p. 299-316.
12. Takahashi, K., S.N. Arjunan, and M. Tomita, *Space in systems biology of signaling pathways--towards intracellular molecular crowding in silico*. FEBS Lett, 2005. **579**(8): p. 1783-8.

13. Zorrilla, S., M. Jimenez, P. Lillo, G. Rivas, and A.P. Minton, *Sedimentation equilibrium in a solution containing an arbitrary number of solute species at arbitrary concentrations: theory and application to concentrated solutions of ribonuclease*. Biophys Chem, 2004. **108**(1-3): p. 89-100.
14. Lindner, R.A. and G.B. Ralston, *Macromolecular crowding: effects on actin polymerisation*. Biophys Chem, 1997. **66**(1): p. 57-66.
15. Zimmerman, S.B. and A.P. Minton, *Macromolecular crowding: biochemical, biophysical, and physiological consequences*. Annu Rev Biophys Biomol Struct, 1993. **22**: p. 27-65.
16. Zimmerman, S.B. and S.O. Trach, *Estimation of macromolecule concentrations and excluded volume effects for the cytoplasm of Escherichia coli*. J Mol Biol, 1991. **222**(3): p. 599-620.
17. Rivas, G., J.A. Fernandez, and A.P. Minton, *Direct observation of the self-association of dilute proteins in the presence of inert macromolecules at high concentration via tracer sedimentation equilibrium: theory, experiment, and biological significance*. Biochemistry, 1999. **38**(29): p. 9379-88.
18. Minton, A.P., *The effect of volume occupancy upon the thermodynamic activity of proteins: some biochemical consequences*. Mol Cell Biochem, 1983. **55**(2): p. 119-40.
19. Rivas, G., J.A. Fernandez, and A.P. Minton, *Direct observation of the enhancement of noncooperative protein self-assembly by macromolecular crowding: indefinite linear self-association of bacterial cell division protein FtsZ*. Proc Natl Acad Sci U S A, 2001. **98**(6): p. 3150-5.
20. Ross, P.D. and A.P. Minton, *Analysis of non-ideal behavior in concentrated hemoglobin solutions*. J Mol Biol, 1977. **112**(3): p. 437-52.
21. Elowitz, M.B., M.G. Surette, P.E. Wolf, J.B. Stock, and S. Leibler, *Protein mobility in the cytoplasm of Escherichia coli*. J Bacteriol, 1999. **181**(1): p. 197-203.
22. Luby-Phelps, K., *Cytoarchitecture and physical properties of cytoplasm: volume, viscosity, diffusion, intracellular surface area*. Int Rev Cytol, 2000. **192**: p. 189-221.
23. Drenckhahn, D. and T.D. Pollard, *Elongation of actin filaments is a diffusion-limited reaction at the barbed end and is accelerated by inert macromolecules*. J Biol Chem, 1986. **261**(27): p. 12754-8.

24. Arrio-Dupont, M., G. Foucault, M. Vacher, P.F. Devaux, and S. Cribier, *Translational diffusion of globular proteins in the cytoplasm of cultured muscle cells*. Biophys J, 2000. **78**(2): p. 901-7.
25. Lukacs, G.L., P. Haggie, O. Seksek, D. Lechardeur, N. Freedman, and A.S. Verkman, *Size-dependent DNA mobility in cytoplasm and nucleus*. J Biol Chem, 2000. **275**(3): p. 1625-9.
26. Verkman, A.S., *Solute and macromolecule diffusion in cellular aqueous compartments*. Trends Biochem Sci, 2002. **27**(1): p. 27-33.
27. Howard, J. and A.A. Hyman, *Dynamics and mechanics of the microtubule plus end*. Nature, 2003. **422**(6933): p. 753-8.
28. Pollard, T.D., *The cytoskeleton, cellular motility and the reductionist agenda*. Nature, 2003. **422**(6933): p. 741-5.
29. Kural, C., H. Kim, S. Syed, G. Goshima, V.I. Gelfand, and P.R. Selvin, *Kinesin and dynein move a peroxisome in vivo: a tug-of-war or coordinated movement?* Science, 2005. **308**(5727): p. 1469-72.
30. Yildiz, A., J.N. Forkey, S.A. McKinney, T. Ha, Y.E. Goldman, and P.R. Selvin, *Myosin V walks hand-over-hand: single fluorophore imaging with 1.5-nm localization*. Science, 2003. **300**(5628): p. 2061-5.
31. Yildiz, A., M. Tomishige, R.D. Vale, and P.R. Selvin, *Kinesin walks hand-over-hand*. Science, 2004. **303**(5658): p. 676-8.
32. Schliwa, M. and G. Woehlke, *Molecular motors*. Nature, 2003. **422**(6933): p. 759-65.
33. Hirakawa, E., H. Higuchi, and Y.Y. Toyoshima, *Processive movement of single 22S dynein molecules occurs only at low ATP concentrations*. Proc Natl Acad Sci U S A, 2000. **97**(6): p. 2533-7.
34. Mallik, R., B.C. Carter, S.A. Lex, S.J. King, and S.P. Gross, *Cytoplasmic dynein functions as a gear in response to load*. Nature, 2004. **427**(6975): p. 649-52.
35. Dauty, E. and A.S. Verkman, *Molecular crowding reduces to a similar extent the diffusion of small solutes and macromolecules: measurement by fluorescence correlation spectroscopy*. J Mol Recognit, 2004. **17**(5): p. 441-7.
36. Luby-Phelps, K., P.E. Castle, D.L. Taylor, and F. Lanni, *Hindered diffusion of inert tracer particles in the cytoplasm of mouse 3T3 cells*. Proc Natl Acad Sci U S A, 1987. **84**(14): p. 4910-3.

37. Petersen, N.O., P.L. Hoddellius, P.W. Wiseman, O. Seger, and K.E. Magnusson, *Quantitation of membrane receptor distributions by image correlation spectroscopy: concept and application*. Biophys J, 1993. **65**(3): p. 1135-46.
38. Elson, E.L. and D. Magde, *Fluorescence Correlation Spectroscopy. I. Conceptual Basis and Theory*. Biopolymers, 1974. **13**(1): p. 1-27.
39. Magde, D., E.L. Elson, and W.W. Webb, *Thermodynamic fluctuations in a reacting system - Measurement by fluorescence correlation spectroscopy*. Phys Rev Lett, 1972. **29**(11): p. 705-708.
40. Magde, D., E.L. Elson, and W.W. Webb, *Fluorescence correlation spectroscopy. II. An experimental realization*. Biopolymers, 1974. **13**(1): p. 29-61.
41. Kettling, U., A. Koltermann, P. Schwille, and M. Eigen, *Real-time enzyme kinetics monitored by dual-color fluorescence cross-correlation spectroscopy*. Proc Natl Acad Sci U S A, 1998. **95**(4): p. 1416-20.
42. Schwille, P., U. Haupts, S. Maiti, and W.W. Webb, *Molecular dynamics in living cells observed by fluorescence correlation spectroscopy with one- and two-photon excitation*. Biophys J, 1999. **77**(4): p. 2251-65.
43. Schwille, P., J. Korlach, and W.W. Webb, *Fluorescence correlation spectroscopy with single-molecule sensitivity on cell and model membranes*. Cytometry, 1999. **36**(3): p. 176-82.
44. Wachsmuth, M., W. Waldeck, and J. Langowski, *Anomalous diffusion of fluorescent probes inside living cell nuclei investigated by spatially-resolved fluorescence correlation spectroscopy*. J Mol Biol, 2000. **298**(4): p. 677-89.
45. Petersen, N.O., *Scanning fluorescence correlation spectroscopy. I. Theory and simulation of aggregation measurements*. Biophys J, 1986. **49**(4): p. 809-15.
46. Thompson, N.L., A.M. Lieto, and N.W. Allen, *Recent advances in fluorescence correlation spectroscopy*. Curr Opin Struct Biol, 2002. **12**(5): p. 634-41.
47. Huang, Z. and N.L. Thompson, *Imaging fluorescence correlation spectroscopy: nonuniform IgE distributions on planar membranes*. Biophys J, 1996. **70**(4): p. 2001-7.
48. Rocheleau, J.V., P.W. Wiseman, and N.O. Petersen, *Isolation of bright aggregate fluctuations in a multipopulation image correlation spectroscopy system using intensity subtraction*. Biophys J, 2003. **84**(6): p. 4011-22.

49. Wiseman, P.W., F. Capani, J.A. Squier, and M.E. Martone, *Counting dendritic spines in brain tissue slices by image correlation spectroscopy analysis*. J Microsc, 2002. **205**(Pt 2): p. 177-86.
50. Srivastava, M. and N.O. Petersen, *Image cross-correlation spectroscopy: A new experimental biophysical approach to measurement of flow diffusion of fluorescent molecules*. Methods Cell Sci., 1996. **18**: p. 47-54.
51. Wiseman, P.W., J.A. Squier, M.H. Ellisman, and K.R. Wilson, *Two-photon image correlation spectroscopy and image cross-correlation spectroscopy*. J Microsc, 2000. **200** (Pt 1): p. 14-25.
52. Axelrod, D., D.E. Koppel, J. Schlessinger, E. Elson, and W.W. Webb, *Mobility measurement by analysis of fluorescence photobleaching recovery kinetics*. Biophys J, 1976. **16**(9): p. 1055-69.
53. Brown, E.B., E.S. Wu, W. Zipfel, and W.W. Webb, *Measurement of molecular diffusion in solution by multiphoton fluorescence photobleaching recovery*. Biophys J, 1999. **77**(5): p. 2837-49.
54. Koppel, D.E., D. Axelrod, J. Schlessinger, E.L. Elson, and W.W. Webb, *Dynamics of fluorescence marker concentration as a probe of mobility*. Biophys J, 1976. **16**(11): p. 1315-29.
55. Nehls, S., E.L. Snapp, N.B. Cole, K.J. Zaal, A.K. Kenworthy, T.H. Roberts, J. Ellenberg, J.F. Presley, E. Siggia, and J. Lippincott-Schwartz, *Dynamics and retention of misfolded proteins in native ER membranes*. Nat Cell Biol, 2000. **2**(5): p. 288-95.
56. White, J. and E. Stelzer, *Photobleaching GFP reveals protein dynamics inside live cells*. Trends Cell Biol, 1999. **9**(2): p. 61-5.

## **Chapter 2: Quantitating Intracellular Transport of Polyplexes by Spatio-Temporal Image Correlation Spectroscopy**

### **2.1 Abstract**

Quantitatively understanding how non-viral gene delivery vectors (polyplexes) are transported inside cells is essential before they can be optimized for gene therapy and medical applications. In this study, we employed spatio-temporal Image Correlation Spectroscopy (ICS) to follow polymer-nucleic acid particles (polyplexes) of various sizes and analyze their diffusive-like and flow behaviors intracellularly in order to elucidate the mechanisms responsible for their transport. ICS is a quantitative imaging technique that allows the assessment of particle motion in complex systems, though it has not been widely used to date. We find that the internalized polyplexes are able to utilize microtubule motors for intracellular trafficking and exhibit different transport behaviors for short (<10 seconds) versus long (~60 seconds) correlation times. This motion can be explained by a memory effect of the microtubule motors. These results reveal that, while microtubule motor biases may be present for short periods of time, resulting in a net directional velocity, the overall long-term motion of the polyplexes is best described as a random walk-like process. These studies suggest that spatio-temporal ICS is a powerful technique for assessing the nature of intracellular motion and provides a quantitative tool to compare the transport of different objects within a living cell.

## 2.2 Introduction

### Viruses and Non-Viral Polyplexes

Viruses, sometimes called nature's own nanotechnology, have one purpose: to replicate themselves. While eukaryotic viruses vary in size from 20-500 nm and have many different shapes, they are rather similar in structure. They consist of a nucleic acid core (RNA or DNA) and a surrounding protein capsid shell. Many viruses also possess a lipid-protein envelope surrounding the capsid. Viruses propagate themselves by infecting a given cell and hijacking that cell's machinery to create thousands of copies [1]. While many known viruses have different target cells and mechanisms of infectivity, eukaryotic viruses must in general penetrate a cell after binding to a specific receptor, persist through uncoating of the capsid, and release genetic material into the cytoplasm for further replication [2]. This mechanism differs markedly from the familiar bacteriophage, which need only inject its DNA into a target bacterial cell. Because of this major difference, eukaryotic viruses have evolved strategies for recognizing and targeting specific cells which allow them to propagate themselves for further infectivity [2].

Because of the specificity and efficiency of viruses, there has been interest in using them as delivery vectors for gene therapy. By removing the genes controlling replication, propagation can be prevented. Indeed, viral delivery vectors have been the primary choice given their receptor target specificity and delivery efficacy [3]. However, while initially promising, many virus-based gene therapy trials resulted in failures, and currently non-viral vectors are now also being considered for DNA delivery. Non-viral vectors generally consist of a cationic polymer or lipid mixture that is combined with DNA at defined ratios to form a nanoscale complex (termed a polyplex). Typical

polymers used to form polyplexes include polyethyleneimine (PEI), polylysine (PLL), and beta-cyclodextrin ( $\beta$ -CD). These polymers are positively charged and electrostatically associate with the negatively charged DNA strands [4]. The sizes of the polyplexes can be tuned by adjusting the volumes and concentrations of polymer and DNA mixed together; typically, such polyplexes range from 50-250 nm in diameter. Nonviral polyplexes have been shown to deliver genes of interest to cells in culture, albeit at low efficiency rates when compared to viral techniques [4-6]. They are also difficult to target to specific cells because there is no receptor-specific mechanism for uptake. Instead, polyplexes enter cells through the nonspecific endocytosis (pinocytosis) pathway and take significantly longer than viruses to deliver their DNA to the nucleus. There is comparatively little knowledge of what happens as the nonviral complexes travel through the cytoplasm towards the nucleus. Understanding such non-viral gene delivery requires knowledge of how they behave within cells, including the mechanisms involved in polyplex trafficking such as endocytosis, cytoplasmic transport, endosomal escape, and nuclear localization [3-5]. Recent reports have indicated the presence of significant bottlenecks in the delivery process, especially problems with endosomal escape [6]. Measuring these dynamics, especially transport parameters, is important to understand both how such delivery methods compare to viruses and how to improve their efficiencies.

### **Image Correlation Spectroscopy**

Confocal microscopy allows for good visualization of small quantities of fluorescently labeled species. However, only a few studies of cytoplasmic transport have

focused on quantitative biophysical parameters such as effective diffusion constants or transport velocities [6-8]. Most experiments measuring these parameters have focused on examining small injected oligonucleotides or proteins [9-13]. In contrast, polyplexes that range in size from 75-250 nm or larger enter by endocytosis and become enclosed in endosomes [14]. For transport of such large entities (>30 nm) such as the polyplexes used for gene therapy, issues such as crowding and microtubule transport become critical [15, 16].

Here, we describe spatio-temporal image correlation spectroscopy (ICS), a technique for characterizing the behavior of polyplexes and other subcellular particles. Image correlation spectroscopy, as first described by Petersen et al. [17], is an imaging corollary to fluorescence correlation spectroscopy (FCS). FCS, as initially detailed by Magde et al. [18-20], involved measuring the statistical fluctuation in the fluorescence signal at a single point as molecules passed through a fixed laser beam; dynamic information was obtained from these fluctuations. FCS has recently been utilized to measure diffusion constants of small proteins both in the cell membrane and cytoplasm [21-24]; it works well for measuring rapid processes occurring on the microsecond to millisecond time scale. In contrast, ICS is useful for measuring processes occurring on a slower time scale (seconds to minutes) for spatially distinct objects such as polyplexes within the cell.

In spatio-temporal ICS, a scanning laser beam (usually within a confocal microscope) is used to measure the fluorescence intensities of objects within a cell [17, 25, 26]. The intensity information from each pixel in the image is then used to calculate the autocorrelation functions. Diffusion and flow information about an entire image

plane, rather than just a fixed point, can be obtained with this method. ICS can provide quantitative information about objects smaller than the optical diffraction limit; however, such objects must be identifiable as discrete puncta for optimal performance. A major benefit of this technique is that it provides information about aggregate behavior in a region of interest by measuring statistical fluctuations. Previous studies have used ICS to determine the number of receptors on a cell surface and their degree of aggregation [27, 28]. These original implementations of ICS did not include a temporal component. More recently, Srivastava et al. [29] and Wiseman et al. [30, 31] have described combined temporal and spatial autocorrelations. Although these studies have focused on model systems such as beads, the authors suggested that the method can be extended to analyze cytoplasmic dynamics. Here, we have successfully extended this methodology for live intracellular imaging studies.

We have measured the effective diffusion constants and transport velocities of polyplexes to understand how they behave when introduced to cells, specifically, how they are transported intracellularly. Our method allows us to continuously monitor intracellular polyplex behavior for up to 5 minutes. Polyplexes have quantitatively different behaviors for short correlation times (<10 seconds) than for longer correlation times. For short intervals, the motion of the polyplex is highly correlated and has a pronounced memory effect (it continues to move along the same straight path as in the previous time step). For longer intervals, the memory effect is lost, and the motions can best be described as a random walk. These behaviors can be thought of in terms of the action and processivity of the microtubule motors (kinesin and dynein) that transport endosomal cargo through the cell. This study demonstrates the potential of spatio-

temporal image correlation spectroscopy for analyzing aspects of intracellular dynamics, which will ultimately be important for monitoring and assessing the efficacy of cellular delivery agents.

## 2.3 Results

### Fluorescent Microsphere Images

The fidelity of our spatio-temporal ICS algorithms were validated using fluorescent microspheres. By imaging microspheres (beads) of known sizes, the number density and diffusion coefficients of the beads can be measured to determine the accuracy of the number density algorithm and to compare the experimental diffusion values with those predicted by the Stokes-Einstein equation ( $D=kT/6\pi\eta r$ , where  $k$  is Boltzmann's constant,  $T$  is the temperature,  $\eta$  is the fluid viscosity, and  $r$  is the particle radius). Beads were placed in either pure water or a 50% glycerol solution. Figure 2.2a shows a representative image from one of twenty-five experiments. Each sequence of images was processed to threshold detector noise (by manual inspection), and the spatial autocorrelation was determined (Figure 2.2b). The autocorrelation curve was fit using Equation S4 and the number densities calculated from the  $g(0,0)$  value for each image (Figure 2.2c,d). In this example, ICS yields a number density of 27 beads from the spatial autocorrelation of Figure 2.2a; a direct count indicated 29 beads in the image. The average error for ten such data sets (25 frames each) was  $6.3 \pm 2.5\%$ ; a sample analysis is shown in Figure S1a. Thus the number density yields a reasonable estimate of the number of beads in each image.

The next step was to validate the diffusion measurements from the temporal autocorrelation trace  $g(0,0,\tau)$ . Equation S8 was utilized as the fit equation because there was a constant convective flow in the sample, yielding both effective diffusion and directed velocity terms. For these microspheres, the effective diffusion term corresponds to the classical diffusion constant for particles freely moving in a fluid, and the velocity term is the velocity due to convective flow. Figure S1b shows the ICS-determined experimental diffusion coefficients compared to theoretical values from the Stokes-Einstein equation ( $n=7$  samples each, standard deviation  $< 10\%$  for each group); the experimental values are mostly within ten percent of the predicted ones. Objects that diffuse with rates of  $5 \times 10^{-9} \text{ cm}^2/\text{s}$  represent the effective maximum limit of the scanning spatio-temporal ICS method using the setup described above, imaged at the maximum frame rate of 10 Hz. Fortunately, intracellular diffusive processes have been reported to be about two orders of magnitude slower, making them suitable candidates for temporal ICS analysis.

### **Fluorescence Imaging of Polyplexes in HeLa cells**

To explore the intracellular motions of different sizes and types of polyplexes, both  $\beta$ -CD polyplexes with diameters of 80, 180, and 220 nm and PEI polyplexes of 100 nm diameter were analyzed; all polyplexes were complexed with Cy5-labeled oligonucleotides. Specifically, the cytoplasm was imaged continuously for at least 300 frames (corresponding to at least 100 seconds), and these images were used to determine polyplex transport parameters. This extended trajectory (which is at least five times longer than previous work [6]) allows for a more detailed picture of the motions of these

polyplexes as they travel through the cell and engage the transport networks to ultimately traffic to the perinuclear region.

As the polyplexes traveled through the cell, we noted that individual polyplexes mostly displayed confined motions in a small region of the cell (with particle trajectories confined to a 500 nm x 500 nm area) [32] or remained stationary over a one hundred second trajectory. A few particles escaped these constraints and rapidly traveled through the cytoplasm in a correlated fashion, continuing along directed pathways with speeds of up to 0.5  $\mu\text{m/s}$ . However, these correlated trajectories typically lasted for ten seconds or less; afterwards, the polyplexes displayed independent behavior and could even return to the starting position. Occasionally a polyplex would travel quickly for a few seconds, then stall, and perhaps continue in a different direction; two such trajectories are shown in Figure 2.3. In general, the trajectories appeared Brownian, with no preferred direction within the cell over this time scale. Similar behavior has been described by Lidke et al. for endosomal trafficking of EGF-quantum dot complexes by microtubule associated proteins [33]. Given these random trajectories, it is not surprising that it usually takes four to five hours for most polyplexes to reach the perinuclear region. In contrast, intracellular viral motion has been shown to often be directed towards the nucleus. For influenza virus, the individual viral particles reach the nucleus within ten minutes of entering the cell because they directly engage the dynein motors [8].

### **Spatio-Temporal ICS Analysis**

Spatio-temporal ICS was then employed to analyze the aggregate diffusion-like and velocity characteristics of the polyplexes. As mentioned, the motion of the

polyplexes empirically resembled a random walk process punctuated by occasional bursts of rapid, directed motion, suggesting the existence of a diffusive (stochastic) process with a putative velocity component throughout the entire trajectory [8]. Of the temporal fit equations, Equations S8 and S9 yield both an effective diffusive term as well as an alternating velocity term. We fit the temporal autocorrelation curve with both equations to see whether both a diffusive term and a directed velocity value could be determined for the polyplexes. These values can ideally be utilized to characterize a cell's microtubule dynamics since the microtubules and their motors are instrumental for endosomal trafficking [34-36]. The velocity component may provide a measure of the activity of the microtubule motors as the polyplex cargoes are transported through the cytoplasm.

Correlation analysis involves examining the average of many simultaneous processes within a system. In this method, the motions of all particles within the region are considered simultaneously. Particles that appear to be temporarily immobile are included in the overall correlation function because they represent important intermediate stages in the overall path. Intensities at all possible time points are compared and  $\tau$  values for all  $\Delta t$  values in a given time-resolved image series are calculated; Figure 2.4 shows a representative example of this analysis for a 60 second trajectory.

From the fits to the temporal correlation curves for all image series, we found a resolvable distinction between two temporally distinct motion regimes – a short correlation period (<10 s) and a longer correlation period (noticeable by ~60 s of correlation time for all data sets). The short correlation period was determined by fitting Equation S8 or S9 to the correlation traces and determining the time at which the velocity term was greater than the effective minimum detectable value of 0.01  $\mu\text{m/s}$  (the limit of

this setup). In most cases, this was for  $\tau$  values of ten seconds, and we chose this as the short correlation period. The longer correlation period was determined by finding the times at which the correlation traces generally reached the minimum  $g(0,0,\tau)$  value and leveled off for at least ten seconds; this was for correlation times of roughly sixty seconds. To confirm the existence of these two regimes, the data was additionally processed using single particle tracking (SPT) analysis [8]; a more detailed comparison of ICS versus SPT is given in Appendix A. For 65 particles from three cells in the 100-nm PEI data set, the slope of the average mean square displacement curve was found to drop noticeably after ten seconds correlation time, as previously determined from correlation analysis (Figure S2). From such analyses, we find that ICS is a useful and more rapid alternative to SPT for determining the average kinetic behavior of multiple intracellular particles.

The polyplexes' motion was characterized by directed motion and diffusion on short time scales and mostly random motion on long time scales. While both the effective diffusion and velocity values differed between the two correlation regimes, the velocity term showed greatest variation (Table 2.1). Velocity values averaged  $0.05 \mu\text{m/s}$  for short correlation times (for all polyplexes) and approached zero for longer correlation times. Effective diffusion terms ranged from  $2.8\text{-}4.5 \times 10^{-11} \text{ cm}^2/\text{s}$  for short correlation times and  $1.4\text{-}2.2 \times 10^{-11} \text{ cm}^2/\text{s}$  for long correlation times. From the 100-second movies, we found that polyplex motion is highly variable and that shorter trajectories are not sufficient to fully characterize their behavior.

To confirm the role of microtubules in polyplex motion, nocodazole was added to the cells after allowing for internalization. Nocodazole is a drug that specifically causes

microtubule depolymerization and would be expected to significantly hinder microtubule-dependent processes, including transport [6, 8]. After addition, the motions of the polyplexes were dramatically reduced when compared to untreated cells (shown in Figure 2.5a); three sample trajectories are shown in Figure 2.5b. For a cell similar to one depicted in Figure 2.5b, the effective diffusion coefficient was found to be  $2.9 \times 10^{-13} \text{ cm}^2/\text{s}$  with no meaningful velocity term, two orders of magnitude smaller than for untreated cells. These nocodazole results illustrate the importance of microtubules for intracellular transport of polyplexes.

## **2.4 Discussion**

### **Implications of Two Temporal Fit Regimes**

The idea of two temporal regimes of intracellular motion is not unique to this system; indeed, similar findings have been reported for micron beads moving in the cytoplasm and chromosome motion in the nucleus [34, 37, 38] describing random walk processes. The benefit of our analysis is that it provides information about the system while requiring minimal fit parameters. Polyplex movement is dependent on microtubule transport and the two temporal regimes may also be described in terms of the activity of the microtubules and their motors (kinesin and dynein). For short intervals, the microtubule motors display a memory effect and are able to transport the polyplexes in a nonrandom, directed linear fashion. However, after this interval (which generally lasts up to 10 s), the motors may either pursue a different path or remain in place, and the correlation function decays further. Similar results have been reported by Caspi et al. for transport of micron-sized beads in cytoplasm [34, 37]. For short correlation times, the fits

to the polyplex data yield an average velocity of  $0.05 \mu\text{m/s}$ , independent of size or type; Ichikawa et al. report similar values ( $0.05 \mu\text{m/s}$ ) for endosomal motion [36]. The velocity value represents an average of all particles within a region and not merely individual ones; it can also be thought of as an indirect measure of the activity of the microtubule motors.

This behavior is in contrast to polyplex motion at long correlation times; at long times the velocity term approaches zero when fit to equation S8 or S9. This does not mean that the polyplexes are not transported, but rather the velocity vectors sum to almost zero and particle motion is reflected primarily by the diffusion term. Cumulatively, these data suggest that the particles have a “persistence time” over which transport motion is correlated and continues in that direction without much deviation. After that time, particle motion appears stochastic again. Direct visualization indicates that the directed behavior, during which the particles move a few microns, last for up to roughly ten seconds before the particle stalls or changes direction (Figures 2.3, 2.5a). Over the image series, a given particle may not necessarily move far from its starting position. After many hours of motion, most polyplexes arrive in the perinuclear space.

Overall, the polyplexes exhibit a back and forth movement about their starting positions, similar to what has been reported for individual influenza viruses in one stage of their trajectories [8]. This movement is due to microtubule transport by both minus- and plus-end directed motors [36]. The “persistence time” can be related to the activities of the kinesin and dynein motors. For short periods of time, one group of motors predominates, and the action of these motors propels the polyplex cargo [8]. Competition between different motors oriented in all directions on the endosomal compartment as well

as shifting of cargo between different microtubule tracks causes the measured velocities to be lower than the maximal velocities reported for individual kinesin or dynein motors *in vitro* [39]. We observed many instances of polyplexes being transported initially in one direction for up to ten seconds and then appearing to be transferred to a neighboring microtubule track and moving along a different path. This process continues for several iterations until the particle stalls. This is the only type of motion observed for these polyplexes; in contrast, influenza virus also displays a dynein-dependent, directional stage of motion [8].

Opposite to what might be expected, the effective diffusion terms increase with increasing size of the polyplexes. For instance, the 220 nm  $\beta$ -CD polyplexes (nominal diameter) have the largest effective diffusion constant (Table 2.1). As noted above, this term is only one component of intracellular motion because the particles are hindered by the crowded cytoplasm and cannot move freely. The velocity component, the major determinant of directed motion at short times, is not significantly different among the polyplexes at short times. Aside from the nominal diameter, it is the characteristics of the endosome, powered by kinesin and dynein, that primarily determine diffusion and velocity [6, 36, 40]. Based on the average velocity measurements and effective diffusion constants for the  $\tau$  values, we estimate that motor activity increases slightly with increasing endosome size.

The behavior of these polyplexes provides information about certain aspects of the intracellular environment, including microtubule transport. More generally, spatio-temporal ICS studies provide information about intracellular dynamics and other macromolecular characteristics. In comparison to MPT, ICS can extract a greater amount

of data on a statistically broader basis. ICS can be used to assess the transport characteristics of modified polyplexes and their trafficking efficiencies relative to viruses or other DNA delivery systems, or to analyze the relative importance of transport within the full pathway of polyplex delivery and gene expression. For example, polyplexes with attached ligands can be tested to determine which ligands increase transport velocities, or whether chemical modifications increase nuclear delivery; this information will be useful in developing new agents that have increased transport and efficacy. Spatio-temporal ICS is a powerful technique for assessing the stochastic nature of this motion and calculating number densities, effective diffusion, and velocity values for all correlation times.

## **2.5 Conclusions**

In this work, we have used spatio-temporal image correlation spectroscopy to characterize the aggregate diffusion and velocity characteristics of intracellular polyplexes in real time. Using the standard fit equations described, these trajectories show a distinction between short and long correlation times, indicating that the motion of intracellular polyplexes is often vectorially directed for short periods of time (up to 10 seconds) but is stochastic for longer periods; these motions are dependent upon the activity of microtubule motors. Spatio-temporal ICS extends the power of fluorescence correlation spectroscopy into processes that occur on the time scale of many biological and cellular events and it offers an overall picture of the dynamics in an intracellular environment. The dynamics of polyplexes described here should have general implications for the endocytic pathway and transport mechanisms for large (>30 nm) objects in the crowded cellular environment.

## 2.6 Materials and Methods

### *Cells*

HeLa cells were grown in 10-cm culture dishes (Becton-Dickinson) at 37°C in a humid 5% CO<sub>2</sub> atmosphere. Each dish held 10 mL of growth media (DMEM with 10% fetal bovine serum, 100 U/mL penicillin, 100 U/mL streptomycin, 10 mM HEPES, 0.1 mM non-essential amino acids, and 2 mM L-glutamine; Irvine Scientific). The cells were passaged once a week and plated onto cover slip-bottom tissue culture plates (Labtek) for imaging experiments (1.5 mL per well). Cells were incubated for 24 hours before transfection.

### *Fluorescent microsphere preparation*

Green fluorescent microspheres of sizes 200 nm, 500 nm, 1 μm, and 2 μm (FluoSpheres, Molecular Probes) were diluted 1:100 in either pure water or a 50% glycerol solution, placed onto a cover slip (50 μL), and imaged on the confocal microscope.

### *DNA polyplexes*

See Figure 2.1 for a schematic illustration of the chemical structures of the polymers. β-cyclodextrin-containing polymers (CD) were synthesized as described previously [40]. The polymers were modified with adamantane-poly(ethylene glycol)5000 to prevent particle aggregation in the presence of salt [40]. Adamantane is a small hydrophobic molecule that associates with the cyclodextrin by forming an inclusion compound within the hydrophobic cavity. Without adamantane-PEG modification, the

polyplexes aggregate excessively in solution [40]. All DNA used to generate polyplexes was fluorescently labeled with Cy5 dye. To form  $\beta$ -CDP/DNA polyplexes, equal volumes of a 1 mg/mL  $\beta$ -CD polymer solution and a 0.1 mg/mL Cy5-labeled oligonucleotide solution (both in H<sub>2</sub>O) were incubated at room temperature for 30 minutes. The 25-kDa branched polyethyleneimine (PEI)/DNA polyplexes were formulated similarly. Equal volumes of a 0.067 mg/mL PEI solution and a 0.1 mg/mL Cy5-oligo solution (both in 20 mM HEPES, 50 mg/mL glucose) were incubated at room temperature for 30 minutes. Subsequently, 2  $\mu$ L of a 20 mg/mL mPEG5000-SPA (in H<sub>2</sub>O) was added and allowed to incubate at RT for another 15 minutes. Both the  $\beta$ -CDP/DNA and PEI/DNA complexes had a 5:1 nitrogen:phosphate ratio. The size of the polyplexes (dependent on the concentrations of precursor and DNA) was measured by dynamic light scattering (Brookhaven Instruments). The sizes referred to as 80 nm, 100 nm, 180 nm, and 220 nm are the effective mean diameters (by dynamic light scattering) of four different samples of monodisperse polyplexes, with variance of 3% or less. Both the PEGylated  $\beta$ -CDP/DNA and PEI/DNA polyplexes have been shown to enter and move within cells as non-aggregated particles via transmission electron microscopy studies [40].

### *Fluorescence Microscopy*

An inverted Zeiss LSM 510 META confocal microscope was used for all fluorescence and brightfield measurements. Scan parameters (pixel time, scan area, and laser intensity) were varied to maximize the signal-to-noise ratio while minimizing frame time. Excitation of the green fluorescent microspheres was achieved with the 488 nm line of the argon ion laser, and excitation of Cy5 was achieved with the 633 nm He-Ne laser

line. The fluorescence signal was detected through a variable confocal pinhole set to 1.5 Airy units, which was chosen to maximize the S/N ratio while minimizing out-of-plane light. At least three hundred consecutive images were taken of each cell, with individual image frame rates varying between 1-2 Hz.

### *Theory of Spatio-Temporal ICS Analysis*

Temporal correlation spectroscopy involves the calculation of the normalized autocorrelation function,  $g(t)$ , of a fluctuating fluorescence signal,  $i(t)$ , at a given time  $t$ . A normalized temporal autocorrelation function can be expressed as:

$$g(\tau) = \frac{\langle \delta i(t) \delta i(t + \tau) \rangle}{\langle i \rangle^2}, \quad (\text{S1})$$

where  $\delta i(t) = (i(t) - \langle i \rangle)$ ,  $\langle i \rangle$  is the average intensity over all time points, and  $\tau$  represents a temporal shift (measured as a change in time from the starting  $t$ ).

An autocorrelation function can be similarly calculated in the spatial domain. Consider an image of  $M$  by  $N$  pixels, with the variables  $x$  and  $y$  representing pixel intensities as a function of discrete image space.  $x$  and  $y$  are spatial indices, measured as a function of distance (in  $\mu\text{m}$ ) from the upper left corner of a given image; each point  $(x,y)$  has an associated pixel intensity  $i(x,y)$ . The spatial autocorrelation function is defined as

$$g(\xi, \eta) = \frac{\langle \delta i(x, y) \delta i(x + \xi, y + \eta) \rangle}{\langle i \rangle_{x,y}^2}, \quad (\text{S2a})$$

where  $\delta i(x,y) = (i(x,y) - \langle i \rangle_{x,y})$  and the spatial mean intensity is defined as

$$\langle i \rangle_{x,y} = \frac{1}{MN} \sum_{x=1}^M \sum_{y=1}^N i(x, y), \quad (\text{S2b})$$

and where  $\xi$  and  $\eta$  represent spatial lag variables measured as a change in position from the starting  $x$  and  $y$  values. Alternatively, the spatial autocorrelation function can be calculated by taking the Fourier transform of the power spectrum of the data, as described by Petersen et al. [17].

If the two autocorrelation functions are used simultaneously, the result is the combined spatio-temporal autocorrelation function for spatio-temporal ICS, and is defined as

$$g(\xi, \eta, \tau) = \frac{\langle \delta i(x, y, t) \delta i(x + \xi, y + \eta, t + \tau) \rangle}{\langle i(t) \rangle_{x,y} \langle i(t + \tau) \rangle_{x,y}}, \quad (\text{S3})$$

where  $\langle i \rangle_{x,y}$  denotes a spatial average (but not a temporal average) over  $x$  and  $y$  at time point  $t$ . The spatial intensity fluctuations are defined as  $\delta i(x, y, t) = (i(x, y, t) - \langle i(t) \rangle_{x,y})$  and  $\tau$  is the correlation time.

Once the spatio-temporal autocorrelation function has been calculated, the resulting curves must be fit to obtain physical information about the systems. The temporal and spatial domains of Equation S3 may be treated separately by calculating both  $g(\xi, \eta, 0)$  and  $g(0, 0, \tau)$ . The two can be separated since the  $g(0, 0, 0)$  term needed to fit  $g(0, 0, \tau)$  (the temporal autocorrelation portion, Equation S6) is obtained from the spatial autocorrelation equation for all  $\tau=0$ . Separating the two terms reduces the computational power required. The spatial autocorrelation portion was fit by non-linear least squares with a two-dimensional Gaussian function as previously described by Petersen [17]:

$$g(\xi, \eta, 0) = g(0, 0, 0) e^{-\frac{(\xi^2 + \eta^2)}{w^2}} + g_0, \quad (\text{S4})$$

where  $g(0, 0, 0)$  is the zero spatial lag value,  $w$  is the calculated  $e^{-2}$  beam radius in the focal plane, and  $g_0$  is a component residual resulting because the autocorrelation does not

decay to zero due to limited sampling size; all three variables are fit parameters for this equation.

The number of particles per image (also called number density) can be obtained from the zero lag value  $g(0,0,0)$  from the following equation, where *pixelsize* is the edge length of each square pixel in the image [17]

$$n = \frac{MN * (pixelsize)^2}{g(0,0,0)\pi w^2}. \quad (S5)$$

By calculating the spatial correlation per image, the number density for each image in the series can be determined.

The temporal autocorrelation portion of Equation S3 can now be fitted. For ease of computation, the following equation was used to evaluate  $g(0,0,\tau)$  for each value of  $\tau$  [31]

$$g(0,0,\tau) = \frac{1}{T-\tau} \sum_{t=1}^{T-\tau} \frac{1}{MN} * \sum_{x=1}^M \sum_{y=1}^N \frac{\langle \tilde{\delta}i(x,y,t) \tilde{\delta}i(x,y,t+\tau) \rangle}{\langle i(t) \rangle_{x,y} \langle i(t+\tau) \rangle_{x,y}}, \quad (S6)$$

where T is the total number of time points and  $\tau$  ranges from 0 to T-1.

The temporal autocorrelation equation can provide information about the dynamics of the system. Past experiments on intracellular behaviors involving microtubules have indicated the presence of a diffusive-like term and often a directed velocity term for short periods of time. In this case, the effective diffusion term represents Brownian processes that follow a random walk model. Using the value of  $g(0,0,\tau)$  from above, the following equation (with zero velocity) can be fit by least squares to obtain an effective diffusion term:

$$g(0,0,\tau) = \frac{g(0,0,0)}{\left(1 + \frac{\tau}{\tau_d}\right) \left[1 + \left(\frac{\langle w \rangle}{z}\right)^2 \left(\frac{\tau}{\tau_d}\right)\right]^{1/2}} + h_0, \quad (\text{S7})$$

where  $\langle w \rangle$  is the average beam radius, as determined from the spatial autocorrelation,  $\tau_d$  is the best fit characteristic diffusion time,  $h_0$  is a fitting offset parameter accounting for cases when the correlation function does not decay to zero at long lag times, and  $z$  is the beam radius in the axial direction (determined from the point spread function) [41]. The effective diffusion term  $D$  then can be calculated from  $\tau_d$  using the following relation:

$$D = \langle w \rangle^2 / 4\tau_d.$$

Equation S7 can be expanded to allow for a directed velocity term in addition to the effective diffusion term for a single population. This velocity term corresponds to motion superimposed upon that expected by a random walk process.

$$g(0,0,\tau) = \frac{g(0,0,0)}{\left(1 + \frac{\tau}{\tau_d}\right) \left[1 + \left(\frac{\langle w \rangle}{z}\right)^2 \left(\frac{\tau}{\tau_d}\right)\right]^{1/2}} \exp\left[-\left(\frac{\tau}{\tau_f}\right)^2 \frac{1}{\left(1 + \frac{\tau}{\tau_d}\right) \left[1 + \left(\frac{\langle w \rangle}{z}\right)^2 \left(\frac{\tau}{\tau_d}\right)\right]^{1/2}}\right] + h_0, \quad (\text{S8})$$

where  $v$  is the calculated velocity,  $\tau_f$  is the characteristic velocity time ( $\tau_f = w/v$ ), and the other constants are as above [41].

Alternatively, equation S7 can be expanded to allow for directed velocity and diffusion for two different populations. In this case, objects alternate between diffusive motion and directed transport. An example of such motion would be directional velocity due to the concerted action of microtubule motors on a vesicle.

$$g(0,0,\tau) = \frac{g(0,0,0)}{\left(1 + \frac{\tau}{\tau_d}\right) \left[1 + \left(\frac{\langle w \rangle}{z}\right)^2 \left(\frac{\tau}{\tau_d}\right)\right]^{1/2}} + g(0,0,0) \exp\left(-\left(\frac{\tau}{\tau_f}\right)^2\right) + h_0, \quad (\text{S9})$$

where the variables are as previously described [30].

Equations S7, S8, and S9 are the standard equations used in FCS and ICS for fitting autocorrelation functions to find diffusion and velocity terms. The fit functions for diffusion (S7), diffusion plus velocity for one population (S8), and diffusion plus velocity for two populations (S9) were calculated for each temporal correlation function, and the appropriate fit was selected based on the minimum residual value (maximum  $R^2$  value) for the fits.

### *Spatio-Temporal Image Autocorrelation Methods and Analysis*

The z-direction point spread function (PSF) was determined by taking a z-stack of 100 nm-diameter fluorescent microspheres. Fluorophore photobleaching (from continuous laser excitation) limited the maximum continuous observation times to 3-5 minutes; these times can be extended by employing pauses in laser illumination when scanning. No specific correction for photobleaching was performed for these data series.

ICS analysis was performed as described above. Images were manually thresholded by inspection to reduce the background contribution to the average intensity terms. Spatial autocorrelation functions for the images in each fluorescence time series were then calculated using Equation S2a. The spatial component of these correlation functions were then averaged and fit by non-linear least squares using Equation S4 to obtain the value for the beam radius. Next, the temporal correlation functions were separately calculated using Equation S6. These functions were then fit with either the

diffusion (S7), diffusion plus flow (S8), or diffusion alternating with flow equations (S9).

All calculations and fitting procedures were performed using MATLAB software.

### **Acknowledgements**

David Wu was instrumental in writing the MATLAB code used for data analysis. We thank Jeremy Heidel and Swaroop Mishra for assistance in making the polyplexes, Tania Demyanenko for assistance with tissue culture, and Mag Bak, Nils Petersen, Paul Wiggins, Paul Grayson, Michael Liebling, Helen McBride, Mary Dickinson, and Elaine Bearer for helpful discussion and comments. This work was supported by a grant from the NICHD to Scott Fraser and a NDSEG Fellowship to Rajan Kulkarni.

Short $\tau$ (10 s)	D coefficient ( $\times 10^{-11}$ cm <sup>2</sup> /s)	Velocity ( $\mu$ m/s)	Long $\tau$ (~ 60 s)	D coefficient ( $\times 10^{-11}$ cm <sup>2</sup> /s)	Velocity ( $\mu$ m/s)
80 nm Cyclodextrin (n=32)	2.8 $\pm$ 0.8	0.049 $\pm$ 0.020		1.4 $\pm$ 0.6 p<.0001	0.007 $\pm$ 0.008 p<.0001
180 nm Cyclodextrin (n=14)	3.2 $\pm$ 1.4	0.058 $\pm$ 0.021		1.8 $\pm$ 0.6 p<.003	0.008 $\pm$ 0.009 p<.0001
220 nm Cyclodextrin (n=16)	4.4 $\pm$ 1.2	0.056 $\pm$ 0.034		2.2 $\pm$ 0.8 p<.0001	0.005 $\pm$ 0.007 p<.0001
100 nm PEI (n=38)	3.1 $\pm$ 1.1	0.052 $\pm$ 0.031		1.6 $\pm$ 1.1 p<.0001	0.006 $\pm$ 0.009 p<.0001

**Table 2.1:** Effective diffusion coefficients and velocity values for selected nonviral polyplexes for both short correlation times (10 seconds) and long correlation times (~60 seconds, see text). The effective diffusion coefficients decrease somewhat for longer correlation times but the velocity terms (determined by fitting Eq. S8) are reduced by an order of magnitude to essentially zero. Values are reported as mean  $\pm$  standard deviation for the number of independent observations (in parentheses). P values are generated by comparing each parameter at short versus long  $\tau$  values.

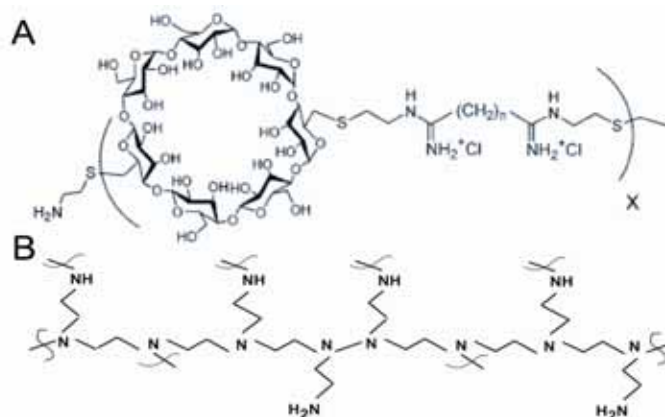


**Figure 2.1:** (A) Chemical structures for  $\beta$ -cyclodextrin (CD) and (B) polyethyleneimine (PEI) polymers used for complexing with DNA to create the nanometer-size polyplexes of interest. The PEI is a highly branched polymer with many free amino groups, as illustrated in the structure, while the CD has a small cavity created by the cyclized sugar moieties.

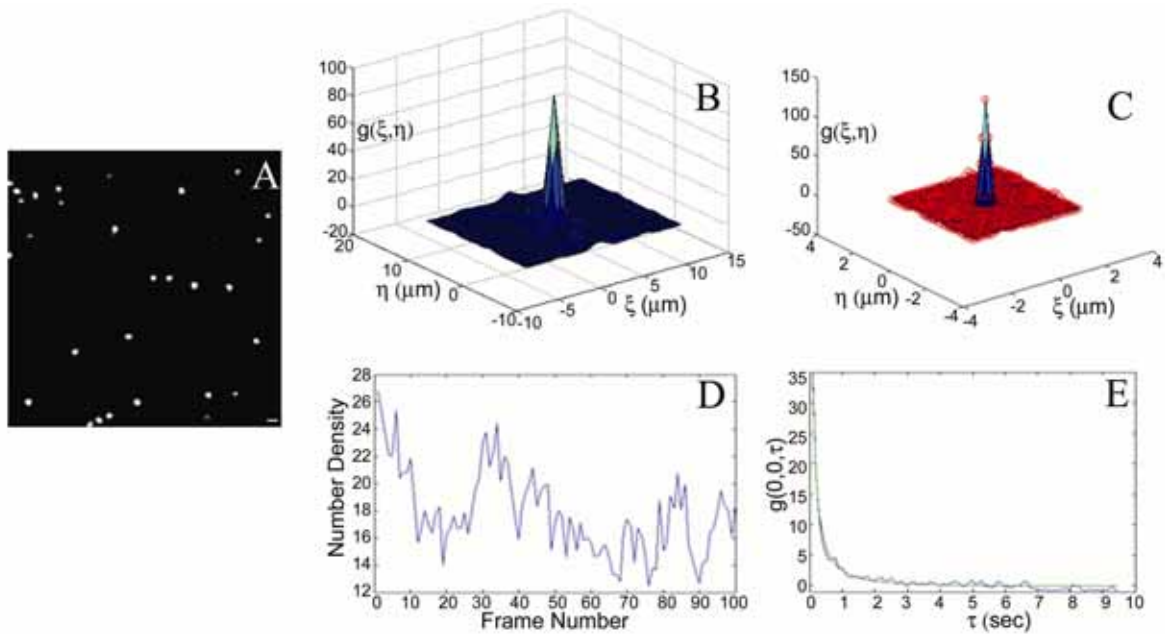


**Figure 2.2:** Temporal image correlation analysis of 200 nm beads in a 50% glycerol solution. (A) The first figure from the time series of 300 images (captured at 10 Hz); 29 beads are present in this image. Scale bar = 1  $\mu\text{m}$ . (B) The average spatial correlation analysis of the raw spatial correlations for each of the first 100 images from this time series is shown in blue. (C) The least squares fit (shown by the red circles) of equation 4 to the spatial autocorrelation in (B). The data is fit for  $\eta$  and  $\xi$  values from -2 to +2. (D) A graph of the number density of particles for the first hundred frames of the data set. The density values are within 10% of the values obtained by direct visualization (not shown). (E) The least squares fit of equation 8 to the temporal autocorrelation curve of the data series. The diffusion coefficient for this curve is measured to be  $2.62 \times 10^{-9} \text{ cm}^2/\text{s}$ , compared to the theoretical Stokes-Einstein value of  $3.12 \times 10^{-9} \text{ cm}^2/\text{s}$ .

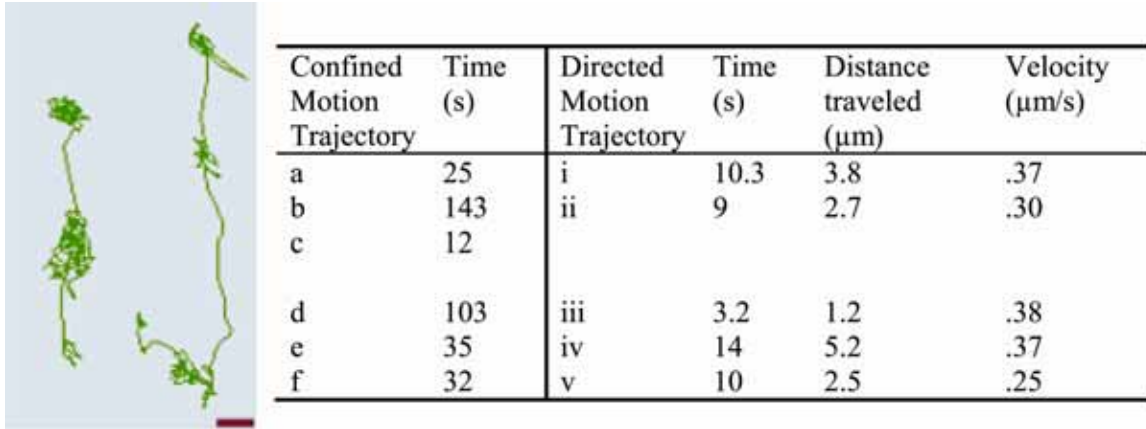


**Figure 2.3:** Two 200-second trajectories of 100-nm PEI polyplexes showing both confined motion (indicated by lettered regions) punctuated by bursts of directed motion (indicated by numbered regions). Both trajectories are of polyplexes within the cell shown in Figure 2.5a. In general, the polyplexes spend much of the time constrained to small regions of 1-2  $\mu\text{m}$  or less. Occasionally, the polyplexes are transported in a directed fashion towards a different region of the cell, as seen by the long, more straight trajectories in between. Time spent in each of the regions, along with distance and linear velocity information (between endpoints for directed motion trajectories), is provided in the table. The scale bar is 1  $\mu\text{m}$  long.

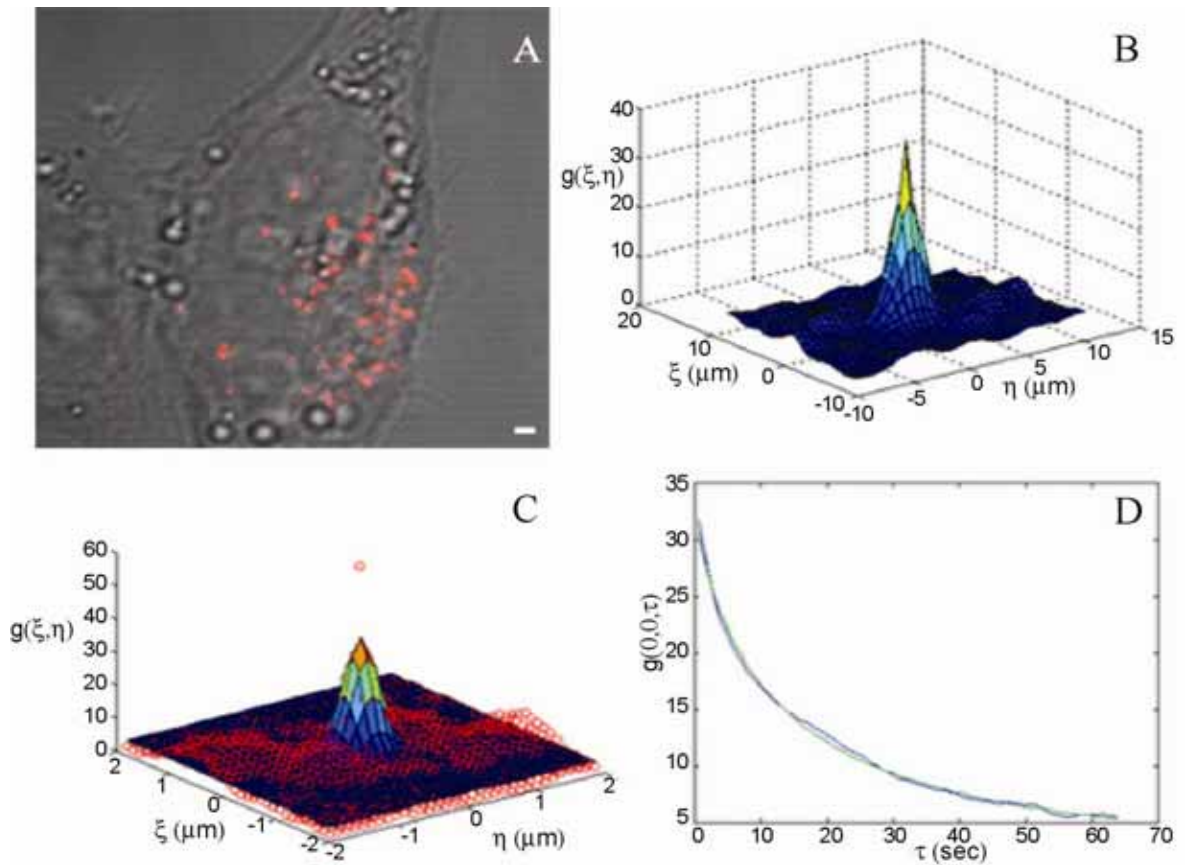


**Figure 2.4:** An example of temporal ICS analysis of intracellular polyplexes. (A) A sample image of 100 nm PEI polyplexes inside a HeLa cell. The polyplexes are likely endosomally located and can be transported on microtubules (see text). The image series contains two hundred images. Scale bar = 1  $\mu\text{m}$ . (B) The raw average spatial correlation trace (shown in blue) for the first hundred images from (A), taken at 1.25 Hz. (C) A Gaussian least squares fit, depicted by red circles, to the data from part B.  $\eta$  and  $\xi$  are evaluated from -2 to +2 for ease of calculation. (D) The temporal autocorrelation trace for the data in (B) and (C). The green line is the best fit (by minimizing the residual, not shown) using the velocity plus diffusion equation (Equation 8).

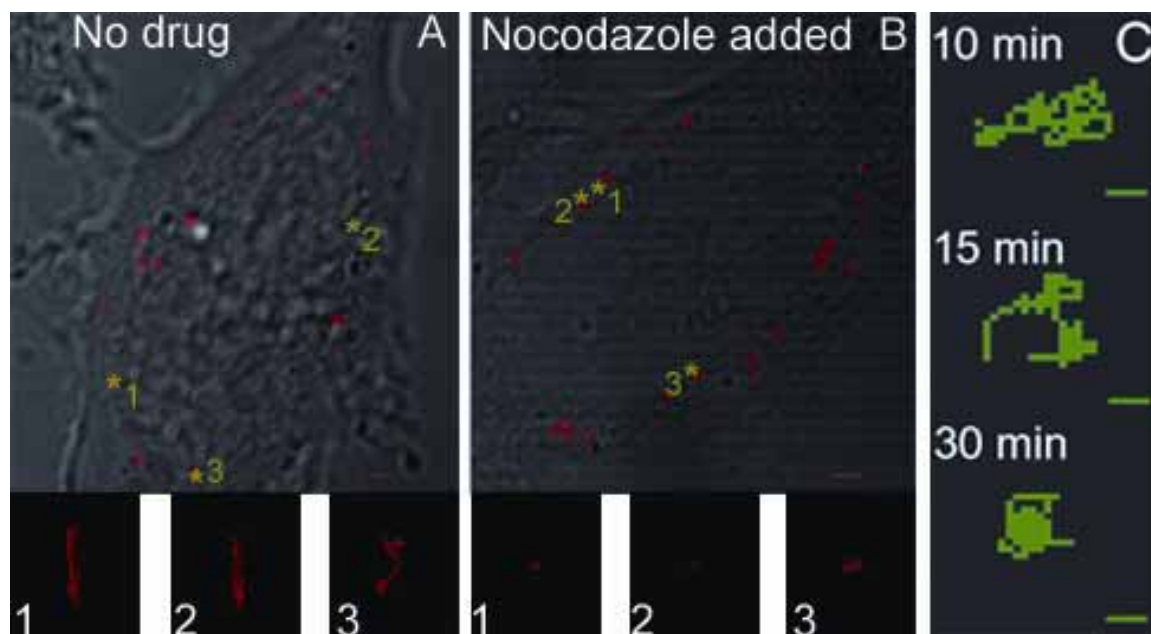


**Figure 2.5:** The effects of nocodazole on intracellular directed transport. (A) 100-second trajectories of three 162 nm cyclodextrin polyplexes in untreated cells. While not all intracellular polyplexes are transported in this manner over the course of visualization, many will have directed motion for about ten seconds before stalling again, as demonstrated in these trajectories. (B) 100-second trajectories of three polyplexes in cells that were treated with nocodazole (final concentration 30  $\mu\text{M}$ ) after allowing polyplex uptake. These images were taken after one hour of incubation in nocodazole. The three trajectories shown are representative of almost all particles seen in the cell; they do not exhibit directed motion as seen in A. The scale bars in A and B are 1  $\mu\text{m}$  long. (C) Time course of nocodazole effect on polyplex trajectories. Representative trajectories are given after 10, 15, and 30 minutes of incubation in 30  $\mu\text{M}$  nocodazole. The maximum trajectories of the polyplexes significantly decreases over time as the drug takes effect. Scale bars = 0.5  $\mu\text{m}$ .

## **2.7 Appendix A: Comparison of ICS to Single/Multiple Particle Tracking Methods**

Recent reviews have nicely described these single/multiple particle tracking (SPT/MPT) methods in detail [32, 42]. Briefly, the idea behind the particle tracking methods is to measure the trajectory of each fluorescent particle or object individually by calculating the centroid of each object and determining how this centroid moves as a function of time. For an image series with only one particle, this does not pose too difficult a problem; however, very few samples contain only one object. Rather, there are often multiple particles within a given field, and difficulty arises in automatically distinguishing between particles that are too close. Often, the trajectories can be erroneously calculated because of nearby neighbors, and manual correction is required to repair the trajectories. The main advantage of particle tracking methods is the ability to gain information about each individual particle. However, many studies that use MPT methods report average values; in these cases, the statistical accuracy of MPT is strongly dependent upon how many points are included in the trajectory.

Image correlation spectroscopy involves using statistical averaging methods to determine the average behavior of many particles within a given field. ICS involves both a spatial and temporal component. The spatial component can be used to count the number of fluorescent objects per image in a large image series, while the temporal component provides the dynamic information. Because ICS does not track individual particles directly, images can be analyzed with no post-processing. An additional advantage of ICS is that it does not assume any a priori knowledge of what the trajectories might look like. With MPT, there are often many additional variables that

need to be specified for automated tracking but are not reported in the resulting equations or data. In ICS, we need only the variables that are required for the fit equations, as described in the previous section.

Another major advantage of ICS is that it can process data in the presence of more noise than with MPT while maintaining greater accuracy. Because noise is randomly distributed, with no spatial or temporal pattern, it can more easily be distinguished from signal and removed accordingly. The time scales of MPT and ICS are dependent upon the ability to generate microscopic images and the processing ability of the computer; there is no theoretical limit to the amount of data that can be analyzed by either technique.

While MPT appears to be the more straightforward approach for data analysis, in many cases ICS would work equally well or potentially better than particle tracking methods - especially when average values are desired. Additionally, it can be harder to separate the diffusion and directed motion components from a single MSD plot than in ICS. Here we have described three common scenarios for transport (diffusion, flow superimposed upon diffusion, and flow alternating with diffusion). The physical significance of the transport parameters from the temporal component of ICS is dependent on how closely these fit functions match the calculated correlation curve. MPT is helpful in cases where one desires information about individual trajectories; otherwise, ICS might actually be an easier method for obtaining similar information, as it does not require manual corrections for trajectory errors.

We have performed a comparison between ICS and MPT for a data set of 500 nm microspheres diffusing in a 30% sucrose solution (100 images, taken at 3.3 Hz). The predicted diffusion coefficient (by the Stokes-Einstein equation) is  $2.58 \times 10^{-13} \text{ m}^2/\text{sec}$ .

We first took this data set and added varying levels of noise such that the signal/noise (S/N) ratio varied from 1 to 10,000. This data is plotted in figure S3. We were able to obtain reasonable diffusion coefficients using ICS to S/N ratios as low as 3, with no additional thresholding. For MPT, data with S/N ratios less than 5 could not be analyzed. From this analysis, we found that ICS analysis yielded results that were slightly closer to the Stokes-Einstein predicted value and that ICS could still be utilized to analyze data with lower S/N ratios than SPT.

We next varied the number of images analyzed per image set (from 25 images to 150 images, taken at 3.3 Hz, with S/N ratio of 5) to determine how the image count affected analysis and the resulting diffusion values; this data is plotted in figure S4. For ICS analysis, the measured diffusion value initially increased slightly with an increasing number of images, but then did not show improvement past 75 images. For MPT analysis, the measured diffusion value approached the Stokes-Einstein value as the number of images increased; however, the measured value still remained higher than the predicted value for all trials.

In performing these analyses, we found that the MPT algorithms required more internal corrections and tinkering to achieve the final result<sup>1</sup>. It was often necessary to adjust the automatic tracking results and remove spurious tracks; for a field of hundreds of particles, this can be prohibitively time-consuming. In contrast, ICS did not require such post-processing corrections and yielded similar results. More detailed information

---

<sup>1</sup> The tinkering necessary for MPT includes specifying noise threshold (greater than for ICS), optimizing particle size, and indicating maximum excursion radius. The latter two are not required for ICS.

about ICS and MPT can be found in Petersen et al. [17] and Suh et al. [6, 42], respectively.

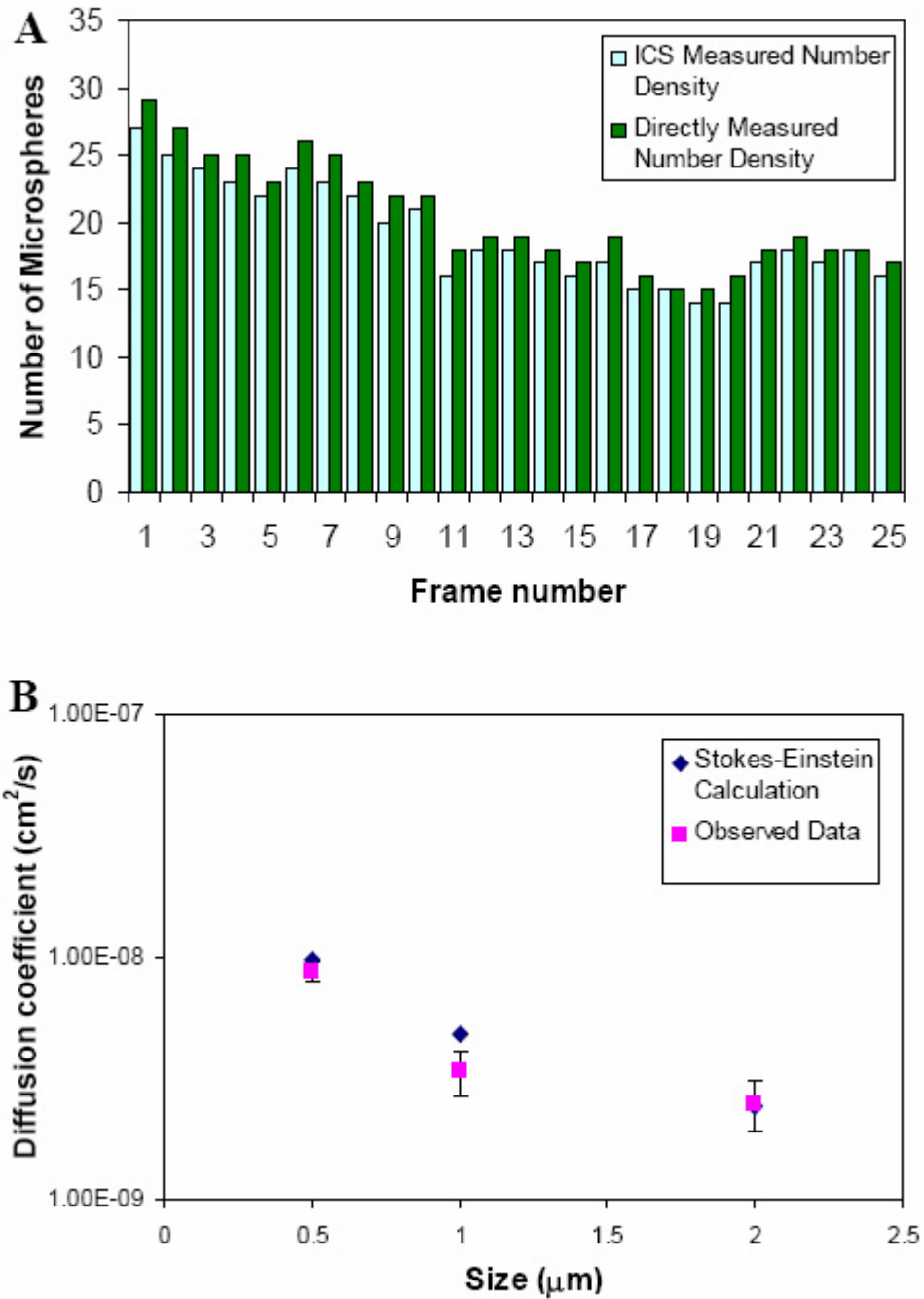


**Figure S1:** (A) A histogram of number density of microspheres for an image series of 25 frames. The ICS measured number density is shown in light blue, while the directly counted number is shown in dark green. The average error between the measured ICS value and the directly counted value is 6.2% for this series. (B) Graph of diffusion coefficients for microspheres of various diameters ( $n=7$  for each data point). The blue diamond data points show the theoretical diffusion coefficients expected for beads of different sizes diffusing in pure water, as determined from the Stokes-Einstein equation ( $D=kT/6\pi\eta r$ , where  $\eta$  is the viscosity of the solution and  $r$  the radius of the particle). The

pink square data points show the diffusion coefficient values obtained for a series of beads in pure water as determined from least squares fitting to Equation S8.

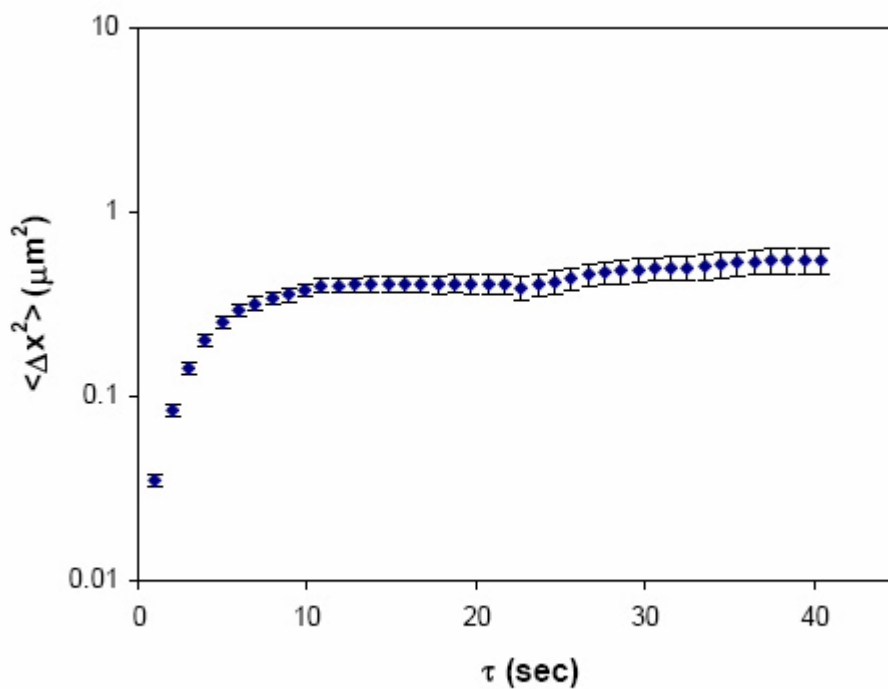


**Figure S2:** Plot of the average mean square displacement versus  $\tau$  for 65 particles from the 100-nm PEI data set using single particle tracking analysis. The slope of the MSD curve drops noticeably after ten seconds correlation time, as also determined from correlation analysis curve fits.

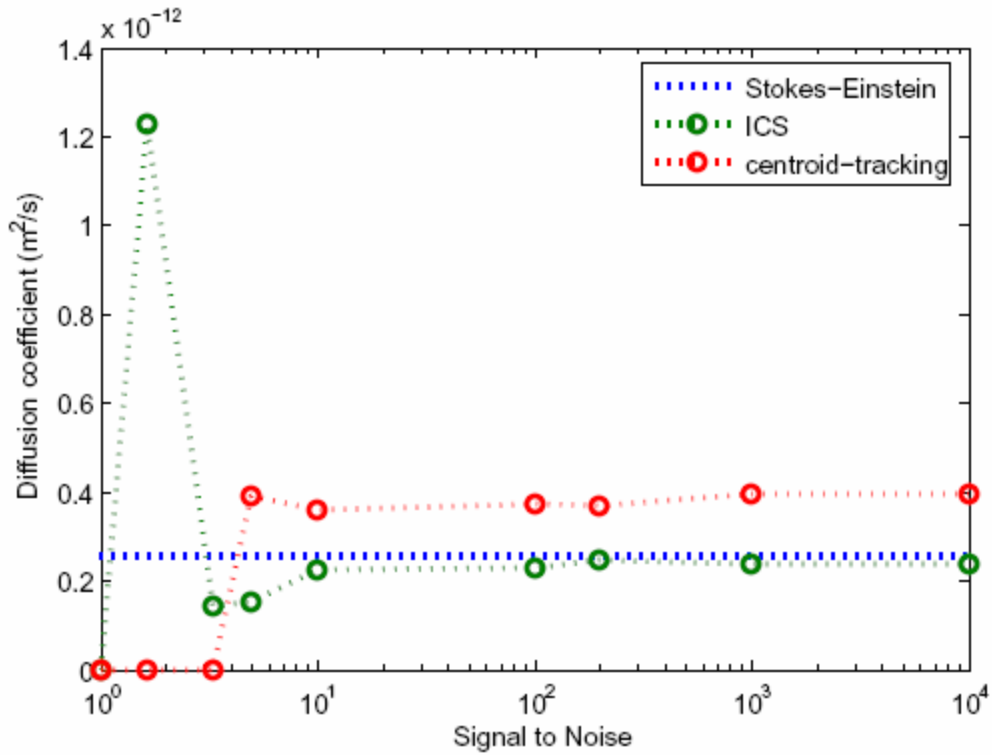


**Figure S3:** Plot of diffusion coefficient versus S/N ratio for ICS analysis (blue diamonds) and MPT analysis (pink squares) for 500 nm diameter microspheres diffusing in 30% sucrose solution. The Stokes-Einstein value is  $2.58 \times 10^{-13} \text{ m}^2/\text{sec}$ . Images were taken at 3.3 Hz. At low S/N values, the data cannot be meaningfully analyzed (signified by zero values for D in this graph).

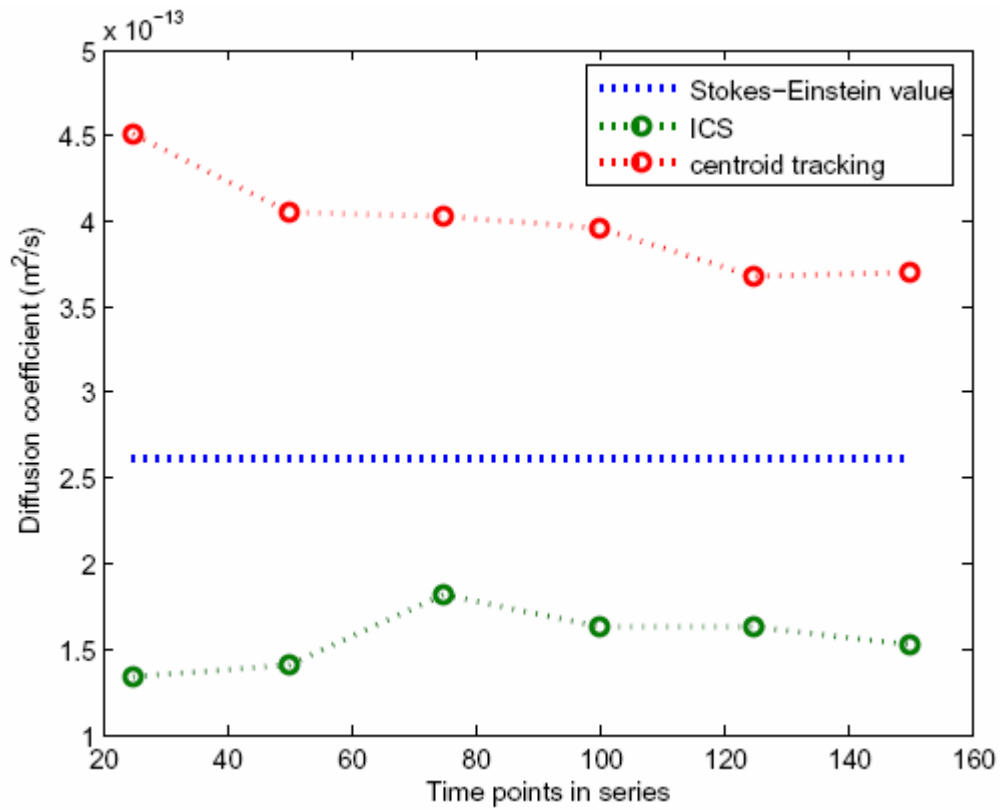


**Figure S4:** Plot of diffusion coefficient versus number of images analyzed for S/N ratio of 5 for ICS analysis (blue diamonds) and MPT analysis (pink squares) for 500 nm diameter microspheres diffusing in 30% sucrose solution. Images were taken at 3.3 Hz.

## 2.8 References

1. Herz, A.V., S. Bonhoeffer, R.M. Anderson, R.M. May, and M.A. Nowak, *Viral dynamics in vivo: limitations on estimates of intracellular delay and virus decay*. Proc Natl Acad Sci U S A, 1996. **93**(14): p. 7247-51.
2. Poranen, M.M., R. Daugelavicius, and D.H. Bamford, *Common principles in viral entry*. Annu Rev Microbiol, 2002. **56**: p. 521-38.
3. Roizman, B., *The function of herpes simplex virus genes: a primer for genetic engineering of novel vectors*. Proc Natl Acad Sci U S A, 1996. **93**(21): p. 11307-12.
4. Boussif, O., F. Lezoualc'h, M.A. Zanta, M.D. Mergny, D. Scherman, B. Demeneix, and J.P. Behr, *A versatile vector for gene and oligonucleotide transfer into cells in culture and in vivo: polyethylenimine*. Proc Natl Acad Sci U S A, 1995. **92**(16): p. 7297-301.
5. Luo, D. and W.M. Saltzman, *Synthetic DNA delivery systems*. Nat Biotechnol, 2000. **18**(1): p. 33-7.
6. Suh, J., D. Wirtz, and J. Hanes, *Efficient active transport of gene nanocarriers to the cell nucleus*. Proc Natl Acad Sci U S A, 2003. **100**(7): p. 3878-82.
7. Gerlich, D., J. Beaudouin, M. Gebhard, J. Ellenberg, and R. Eils, *Four-dimensional imaging and quantitative reconstruction to analyse complex spatiotemporal processes in live cells*. Nat Cell Biol, 2001. **3**(9): p. 852-5.
8. Lakadamyali, M., M.J. Rust, H.P. Babcock, and X. Zhuang, *Visualizing infection of individual influenza viruses*. Proc Natl Acad Sci U S A, 2003. **100**(16): p. 9280-5.
9. Arrio-Dupont, M., G. Foucault, M. Vacher, P.F. Devaux, and S. Cribier, *Translational diffusion of globular proteins in the cytoplasm of cultured muscle cells*. Biophys J, 2000. **78**(2): p. 901-7.
10. Luby-Phelps, K., P.E. Castle, D.L. Taylor, and F. Lanni, *Hindered diffusion of inert tracer particles in the cytoplasm of mouse 3T3 cells*. Proc Natl Acad Sci U S A, 1987. **84**(14): p. 4910-3.
11. Lukacs, G.L., P. Haggie, O. Seksek, D. Lechardeur, N. Freedman, and A.S. Verkman, *Size-dependent DNA mobility in cytoplasm and nucleus*. J Biol Chem, 2000. **275**(3): p. 1625-9.

12. Seksek, O., J. Biwersi, and A.S. Verkman, *Translational diffusion of macromolecule-sized solutes in cytoplasm and nucleus*. J Cell Biol, 1997. **138**(1): p. 131-42.
13. Verkman, A.S., *Solute and macromolecule diffusion in cellular aqueous compartments*. Trends Biochem Sci, 2002. **27**(1): p. 27-33.
14. Forrest, M.L. and D.W. Pack, *On the kinetics of polyplex endocytic trafficking: implications for gene delivery vector design*. Mol Ther, 2002. **6**(1): p. 57-66.
15. Ellis, R.J., *Macromolecular crowding: obvious but underappreciated*. Trends Biochem Sci, 2001. **26**(10): p. 597-604.
16. Ellis, R.J. and A.P. Minton, *Cell biology: join the crowd*. Nature, 2003. **425**(6953): p. 27-8.
17. Petersen, N.O., P.L. Hoddellius, P.W. Wiseman, O. Seger, and K.E. Magnusson, *Quantitation of membrane receptor distributions by image correlation spectroscopy: concept and application*. Biophys J, 1993. **65**(3): p. 1135-46.
18. Elson, E.L. and D. Magde, *Fluorescence Correlation Spectroscopy. I. Conceptual Basis and Theory*. Biopolymers, 1974. **13**(1): p. 1-27.
19. Magde, D., E.L. Elson, and W.W. Webb, *Thermodynamic fluctuations in a reacting system - Measurement by fluorescence correlation spectroscopy*. Phys Rev Lett, 1972. **29**(11): p. 705-708.
20. Magde, D., E.L. Elson, and W.W. Webb, *Fluorescence correlation spectroscopy. II. An experimental realization*. Biopolymers, 1974. **13**(1): p. 29-61.
21. Kettling, U., A. Koltermann, P. Schwille, and M. Eigen, *Real-time enzyme kinetics monitored by dual-color fluorescence cross-correlation spectroscopy*. Proc Natl Acad Sci U S A, 1998. **95**(4): p. 1416-20.
22. Schwille, P., U. Haupts, S. Maiti, and W.W. Webb, *Molecular dynamics in living cells observed by fluorescence correlation spectroscopy with one- and two-photon excitation*. Biophys J, 1999. **77**(4): p. 2251-65.
23. Schwille, P., J. Korfach, and W.W. Webb, *Fluorescence correlation spectroscopy with single-molecule sensitivity on cell and model membranes*. Cytometry, 1999. **36**(3): p. 176-82.
24. Wachsmuth, M., W. Waldeck, and J. Langowski, *Anomalous diffusion of fluorescent probes inside living cell nuclei investigated by spatially-resolved fluorescence correlation spectroscopy*. J Mol Biol, 2000. **298**(4): p. 677-89.

25. Petersen, N.O., *Scanning fluorescence correlation spectroscopy. I. Theory and simulation of aggregation measurements*. Biophys J, 1986. **49**(4): p. 809-15.
26. Thompson, N.L., A.M. Lieto, and N.W. Allen, *Recent advances in fluorescence correlation spectroscopy*. Curr Opin Struct Biol, 2002. **12**(5): p. 634-41.
27. Huang, Z. and N.L. Thompson, *Imaging fluorescence correlation spectroscopy: nonuniform IgE distributions on planar membranes*. Biophys J, 1996. **70**(4): p. 2001-7.
28. Rocheleau, J.V., P.W. Wiseman, and N.O. Petersen, *Isolation of bright aggregate fluctuations in a multipopulation image correlation spectroscopy system using intensity subtraction*. Biophys J, 2003. **84**(6): p. 4011-22.
29. Srivastava, M. and N.O. Petersen, *Image cross-correlation spectroscopy: A new experimental biophysical approach to measurement of flow diffusion of fluorescent molecules*. Methods Cell Sci., 1996. **18**: p. 47-54.
30. Wiseman, P.W., C.M. Brown, D.J. Webb, B. Hebert, N.L. Johnson, J.A. Squier, M.H. Ellisman, and A.F. Horwitz, *Spatial mapping of integrin interactions and dynamics during cell migration by image correlation microscopy*. J Cell Sci, 2004. **117**(Pt 23): p. 5521-34.
31. Wiseman, P.W., J.A. Squier, M.H. Ellisman, and K.R. Wilson, *Two-photon image correlation spectroscopy and image cross-correlation spectroscopy*. J Microsc, 2000. **200** (Pt 1): p. 14-25.
32. Saxton, M.J. and K. Jacobson, *Single-particle tracking: applications to membrane dynamics*. Annu Rev Biophys Biomol Struct, 1997. **26**: p. 373-99.
33. Lidke, D.S., P. Nagy, R. Heintzmann, D.J. Arndt-Jovin, J.N. Post, H.E. Grecco, E.A. Jares-Erijman, and T.M. Jovin, *Quantum dot ligands provide new insights into erbB/HER receptor-mediated signal transduction*. Nat Biotechnol, 2004. **22**(2): p. 198-203.
34. Caspi, A., R. Granek, and M. Elbaum, *Enhanced diffusion in active intracellular transport*. Phys Rev Lett, 2000. **85**(26 Pt 1): p. 5655-8.
35. Hasegawa, S., N. Hirashima, and M. Nakanishi, *Microtubule involvement in the intracellular dynamics for gene transfection mediated by cationic liposomes*. Gene Ther, 2001. **8**(21): p. 1669-73.
36. Ichikawa, T., M. Yamada, D. Homma, R.J. Cherry, I.E. Morrison, and S. Kawato, *Digital fluorescence imaging of trafficking of endosomes containing low-density lipoprotein in brain astroglial cells*. Biochem Biophys Res Commun, 2000. **269**(1): p. 25-30.

37. Caspi, A., R. Granek, and M. Elbaum, *Diffusion and directed motion in cellular transport*. Phys Rev E Stat Nonlin Soft Matter Phys, 2002. **66**(1 Pt 1): p. 011916.
38. Vazquez, J., A.S. Belmont, and J.W. Sedat, *Multiple regimes of constrained chromosome motion are regulated in the interphase Drosophila nucleus*. Curr Biol, 2001. **11**(16): p. 1227-39.
39. Suomalainen, M., M.Y. Nakano, S. Keller, K. Boucke, R.P. Stidwill, and U.F. Greber, *Microtubule-dependent plus- and minus end-directed motilities are competing processes for nuclear targeting of adenovirus*. J Cell Biol, 1999. **144**(4): p. 657-72.
40. Mishra, S., P. Webster, and M.E. Davis, *PEGylation significantly affects cellular uptake and intracellular trafficking of non-viral gene delivery particles*. Eur J Cell Biol, 2004. **83**(3): p. 97-111.
41. Magde, D., W.W. Webb, and E.L. Elson, *Fluorescence correlation spectroscopy. III. Uniform translation and laminar flow*. Biopolymers, 1978. **17**(2): p. 361-376.
42. Suh, J., M. Dawson, and J. Hanes, *Real-time multiple-particle tracking: applications to drug and gene delivery*. Adv Drug Deliv Rev, 2005. **57**(1): p. 63-78.

## **Chapter 3: Intracellular Transport Dynamics of Endosomes Containing DNA Polyplexes Along the Microtubule Network**

### **3.1 Abstract**

We have explored the transport of DNA polyplexes enclosed in endosomes within the cellular environment. The polyplex-loaded endosomes demonstrate enhanced diffusion at short timescales ( $t < 7$  s) with their mean squared displacement (MSD)  $\langle \Delta x(t)^2 \rangle$  scaling as  $t^{1.25}$ . For longer time intervals they exhibit subdiffusive transport and have an MSD scaling as  $t^{0.7}$ . This crossover from an enhanced diffusion to a subdiffusive regime can be explained by considering the action of motor proteins that actively transport these endosomes along the cellular microtubule network and the thermal bending modes of the microtubule network itself.

### 3.2 Introduction

Intracellular transport of organelles and endosomes is crucial for diverse processes such as neuronal signaling, protein secretion, and cell cycle regulation. Cargo is shuttled along the microtubule and actin polymeric transport networks by molecular motors bound to the surface of the organelles. These motors include the myosin family for travel along actin and the kinesin and dynein families for travel along the microtubule network. Many recent *in vitro* experiments have examined the mechanical and biophysical properties of these networks [1]. However, their role and organization is only beginning to be explored intracellularly. This current work focuses on microtubule-mediated transport of DNA-containing polyplexes within endosomes from the cell surface towards the nucleus and the incipient biophysical processes and timescales required for such transport.

Microtubules and the kinesin and dynein motor protein families are primarily responsible for localization of subcellular structures and for trafficking of cargo and vesicles from one location to another. These motors function by converting chemical energy derived from ATP hydrolysis into mechanical work and can be simultaneously present on vesicles and cargo, as shown by bidirectional organelle transport. Additionally, bidirectional switching during transport has been observed, leading to questions of how transport is orchestrated among the motors on the organelle surface [2, 3]. Recent studies have indicated that vesicles and endosomes contain both types of motors on their surfaces, and that the two may be regulated by dynactin or other proteins [4]. Such regulation enables them to engage cooperatively, allowing for processive motion for hundreds of nanometers in a single direction. However, intracellular organelle

motion can also appear disorganized, with the organelle appearing to wander randomly in the cytoplasm. Indeed, similar behavior has been seen for polyplexes internalized into endosomes [5].

Previous studies of intracellular transport along microtubules employed large micron-sized beads that were engulfed by endocytosis [6, 7]. However, most cellular endosomes are much smaller than this [8]. We therefore decided to examine microtubule-mediated endosomal transport of fluorescently labeled nonviral DNA-containing polyplexes ranging from 100-200 nm in diameter. Such polyplexes are often utilized for gene transfection and delivery; it is therefore critical to examine the cytoskeletal mechanics of endosome transport, including microtubule motor activities, to better understand the dynamics of this pathway. In this case, these endosomes, filled with labeled polyplexes, are transported by the microtubule network in a retrograde fashion, from the cell membrane towards the nucleus.

For this study, we used Cy5-labeled  $\beta$ -cyclodextrin ( $\beta$ -CD)/DNA polyplexes that were internalized into endosomes. The polyplexes were introduced into the media of growing HeLa cells, and their transport was subsequently imaged using confocal microscopy. The labeled polyplexes were used as markers for the endosomes. Measurements were made on a Zeiss 510 confocal microscope equipped with an oil-immersion 100X/1.4 NA objective. Images were taken at 2 Hz for 2-3 minutes continuously.

Prior work using 200 nm  $\beta$ -CD polyplexes within endosomes has shown that the average aggregate trajectories of such polyplexes is often random, though the individual polyplexes exhibit a diverse range of behaviors [5]. Here, we used multiple particle

tracking (MPT) [9] to simultaneously obtain information on a large number of individual polyplex-loaded endosomes as they traveled from the cell membrane towards the nucleus. We performed MPT on the acquired data frames using a correlation-based approach to identify particles and a local search algorithm to assemble individual trajectories from the acquired frames. The coordinate data from the trajectories was then used to compute the two-dimensional mean square displacements (MSD) as a function of time. The MSD plot for each trajectory was obtained by using all independent time segments of a given time scale. For small time scales there are many such independent intervals, which gives a more accurate estimation. At longer time intervals, there are fewer independent intervals leading to more uncertainty in parameter estimation.

### 3.3 Results and Discussion

The trajectories for 35 particles were averaged to generate the final MSD plot ( $\langle \Delta x(t)^2 \rangle$  vs.  $t$ ) in Figure 3.1, which shows two distinct regimes. At short timescales ( $t < 7$  s) the polyplex-containing endosomes demonstrate enhanced diffusion with a scaling exponent  $\alpha=1.25\pm 0.04$  so that  $\langle \Delta x(t)^2 \rangle \sim t^{1.25}$ . At longer timescales ( $t > 10$  s) these endosomes exhibit subdiffusive behavior with  $\alpha=0.7\pm 0.07$ . The variation in individual trajectories is larger in this regime since fewer independent time intervals are available to compute the MSD values for the trajectories.

The transition from enhanced diffusive ( $1 < \alpha < 2$ ) to subdiffusive ( $\alpha < 1$ ) transport can be explained using the framework described by Caspi et. al that utilizes a generalized Einstein relationship with time-dependent friction, which is a result of the non-Newtonian environment in the cell [6, 7]. This model considers the microtubules as a weakly

entangled network, and the movement of particles in this medium is affected by the equilibrium modes of the filaments. The motion of particles results in deformations of the microtubule network and in the process activates various bending modes of the filaments. Since the damping rate of each bending mode of the filaments is wavelength dependent, the effective drag experienced by the particle also becomes time-dependent.

The microtubule network can be considered a mesh of interconnecting segments, with the microtubules treated as a weakly entangled network. Binding of motors to these microtubules (when moving an endosome, for example) results in deformations of the microtubules, as mentioned. Now we can consider the MSD of a point along the microtubule network (Figure 3.2). Because the point is an integral part of the microtubule network, its motions are restricted by the neighboring points. Thus, the MSD of a point at a distance  $x$  along a given microtubule filament is given by

$$\langle \Delta h^2(x, t) \rangle = \langle [h(x, t) - h(x, 0)]^2 \rangle, \quad (1)$$

where  $h(x, t)$  is the location of a given point  $x$  along the microtubule filament at time  $t$ .

At short times, the transverse MSD of this point  $h$  along the filament can be written as

$$\langle \Delta h^2(x, t) \rangle \propto \frac{k_B T}{\eta^{3/4} \kappa^{1/4}} t^{3/4}, \quad (2)$$

where  $k_B$  is Boltzmann's constant,  $T$  is the absolute temperature,  $\eta$  is the viscosity of the medium, and  $\kappa$  is related to the persistence length of the microtubule. Thus, the thermal contribution to motion of a point along the MT relates as  $t^{0.75}$ . This equation holds in the absence of any driving force.

This treatment also holds for particles embedded in a polymeric network, for particles larger than the mesh size of the network. For such particles, we can describe the two-dimensional MSD due to thermal processes (with no driving force present),  $\langle x^2(t) \rangle_{TH}$ , using the Einstein relationship between thermal and force-dependent processes. In a case with no driving force, we find that

$$\frac{4k_B T}{\mu_e(t)} = \frac{d}{dt} \langle x^2(t) \rangle_{TH}, \quad (3)$$

where  $\mu_e$  is the time-dependent friction of the process. This in turn implies a time-dependent friction with scaling  $\mu(t) \sim t^{1/4}$  [7]. However, most intracellular objects are enclosed within endosomes or other vesicles and are consequently transported by the MT motors. The two types of motors, kinesin and dynein, drive the endosome in opposite directions. Thus, on long time scales, the mean driving force tends to zero. However, at short time scales, there is a significant component of this driving force which affects the net MSD of the endosomes. Using the time-dependent friction scaling in the presence of the applied motor driving force  $\langle x^2(t) \rangle_F$ , we find that the effect of this force on the MSD at short time scales can be calculated as

$$\langle x^2(t) \rangle_F = \frac{\langle F^2 \rangle}{\langle 4k_B T \rangle^2} \langle x^2(t) \rangle_{TH}^2 \propto t^{3/2}, \quad (4)$$

where  $\langle x^2(t) \rangle_{TH}$  is the two-dimensional MSD due solely to thermal processes (with no driving force present) and  $F$  is the driving force.

This equation holds for cases where the time of motion is short relative to the correlation time of the force, which is the time over which a given directional force lasts. Over long times, in which there may be many changes in the direction and magnitude of

the driving force, resulting in decorrelation of the driving force, we can write the MSD instead as

$$\langle x^2(t) \rangle_F = \int_0^t \frac{\langle F^2 \rangle \tau}{[\mu_e(t-t_1)]^2} dt_1 \propto t^{1/2}, \quad (5)$$

where  $\tau$  is the correlation time for the driving force.

Consequently, particles subjected to an external driving force can be shown to exhibit enhanced diffusive motion with  $t^{3/2}$  scaling for times that are small compared to the correlation time of the force and sub-diffusive motion with  $t^{1/2}$  scaling for longer timescales.

The correlation time of the driving force provides a crossover timescale and is a function of the interaction mechanism of the molecular motors with the endosome. For short time intervals, the microtubule motors are highly correlated and can apply continuous force for hundreds of steps (generally up to 10 seconds), leading to the observed enhanced diffusion behavior [2, 3]. However, at longer times, the motors' driving force is uncorrelated since many individual motors act on the endosome, leading to sub-diffusive motion. The crossover phenomenon between these two regimes of motion assumes an intimate contact between the particle and the surrounding microtubules, which is true for particles that are large compared to the tubule mesh size. Such particles effectively cannot “wobble” thermally and their motion is solely dependent on motor transport. The motion of such large particles is then dominated by the driving force exerted by multiple motors acting on it simultaneously. Particles that are small compared to mesh size can move without the action of motors in a restricted region, and their net motions are caused by a combination of thermal excitations and driving due to

motor proteins (see Figure 3.3). This results in a lower exponent, which would be expected to decrease as the size of the particle decreases, since smaller particles would be expected to “wobble” more within the MT mesh. Consequently, such wobbling would then result in an increased contribution of the thermal component to the MSD, which scales as  $t^{0.75}$ , and therefore an overall decreased time exponent.

However, at long times, the opposite would be true since the exponent due solely to the external driving force would be 0.5. In this case, for particles that can wiggle, the observed exponent will be between 0.5 and 0.75, the exponent due solely to thermal fluctuations. This value would decrease as the particle size increased, as larger particles would be less able to move within the MT network. The exact value of the exponent depends upon the size of the object relative to the mesh created by the microtubule network and the ambient temperature.

In our experiments, the polyplex size is between 100 and 200 nm, and we observe an exponent of 1.25 in the enhanced diffusion regime, which is less than that observed for micron-sized beads. The small polyplex-containing endosomes are not completely trapped by the microtubule mesh and can wiggle laterally due to thermal motions [5, 7]. This small thermal contribution causes a reduction in the exponent from the theoretically expected value of 1.5. In the sub-diffusive regime, decreasing the particle size is expected to increase the exponent (from  $\alpha=0.5$ ) since the contribution due to the thermal excitation increases. We also observe this trend and obtain an average exponent of 0.7 as compared to the theoretically predicted value of 0.5. To determine the role of interactions of the filamentous actin network with these endosomes, cells were treated latrunculin A in order to depolymerize actin, which should increase the mesh size and therefore the thermal

contribution to  $\alpha$ . We find that  $\alpha=1.02\pm 0.13$  for short times and  $\alpha=0.74\pm 0.09$  for long times, as predicted. Finally, to verify that these dynamics are primarily due to microtubule transport, cells were treated with nocodazole to depolymerize the microtubules. Long range endosome motions are not observed and enhanced diffusion is eliminated, with  $\alpha=0.74\pm 0.07$ , solely reflecting the subdiffusive thermal contribution to endosomal motion.

In this work, we have studied the intracellular transport of nonviral DNA-containing polyplexes within endosomes. The observed crossover behavior from enhanced diffusive to sub-diffusive transport is consistent with a time-dependent friction model for transport through semiflexible polymeric networks. Furthermore, the small size of the polyplexes (and other biologically significant organelles) relative to the microtubule mesh allows for a thermal contribution to motion resulting in modified exponents in both regimes. These results of polyplex dynamics are important for better understanding the endocytic pathway and transport mechanisms for similar sized objects within the intracellular milieu.

### **3.4 Materials and Methods**

#### *Cells*

HeLa cells were grown in 10-cm culture dishes (Becton-Dickinson) at 37°C in a humid 5% CO<sub>2</sub> atmosphere. Each dish held 10 mL of growth media (DMEM with 10% fetal bovine serum, 100 U/mL penicillin, 100 U/mL streptomycin, 10 mM HEPES, 0.1 mM non-essential amino acids, and 2 mM L-glutamine; Irvine Scientific). The cells were passaged once a week and plated onto cover slip-bottom tissue culture plates (Labtek) for

imaging experiments (1.5 mL per well). Cells were incubated for 24 hours before transfection.

### *DNA polyplexes*

$\beta$ -cyclodextrin-containing polymers (CD) were modified with adamantane-poly(ethylene glycol)5000 to prevent particle aggregation in the presence of salt. All DNA used to generate polyplexes was fluorescently labeled with Cy5 dye. To form  $\beta$ -CDP/DNA polyplexes, equal volumes of a 1 mg/mL  $\beta$ -CD polymer solution and a 0.1 mg/mL Cy5-labeled oligonucleotide solution (both in H<sub>2</sub>O) were incubated at room temperature for 30 minutes. The 25-kDa branched polyethyleneimine (PEI)/DNA polyplexes were formulated similarly. Equal volumes of a 0.067 mg/mL PEI solution and a 0.1 mg/mL Cy5-oligo solution (both in 20 mM HEPES, 50 mg/mL glucose) were incubated at room temperature for 30 minutes. Subsequently, 2  $\mu$ L of a 20 mg/mL mPEG5000-SPA (in H<sub>2</sub>O) was added and allowed to incubate at RT for another 15 minutes. Both the  $\beta$ -CDP/DNA and PEI/DNA complexes had a 5:1 nitrogen:phosphate ratio. The size of the polyplexes (dependent on the concentrations of precursor and DNA) was measured by dynamic light scattering (Brookhaven Instruments).

### *Fluorescence Microscopy*

An inverted Zeiss LSM 510 META confocal microscope was used for all fluorescence and brightfield measurements. All images were taken with a 100x/1.4 NA oil-immersion objective. Scan parameters (pixel time, scan area, and laser intensity) were varied to maximize the signal-to-noise ratio while minimizing frame time.

Excitation of Cy5 was achieved with the 633 nm He-Ne laser line. The fluorescence signal was detected through a variable confocal pinhole set to 1.5 Airy units, which was chosen to maximize the S/N ratio while minimizing out-of-plane light. At least two hundred consecutive images were taken of each cell at a frame rate of 2 Hz.

### *Multiple Particle Tracking*

Multiple particle tracking analysis was performed on the image series to simultaneously obtain mean square displacement (MSD) information on a large number of individual polyplex-loaded endosomes as they traversed the cell. MPT was performed on the image series using a correlation-based approach to identify particles and a local search algorithm to assemble individual trajectories from the acquired frames [9]. The coordinate data from the trajectories was then used to compute the two-dimensional mean square displacements (MSD) as a function of time. The MSD plot for each trajectory was obtained by using all independent time segments of a given time scale. All analyses were performed with custom-written routines using MATLAB software.

### **Acknowledgements**

We thank Kenneth Castelino for assistance in writing the MATLAB scripts for tracking the particles using MPT and Professor Arun Majumdar for helpful comments and discussion.

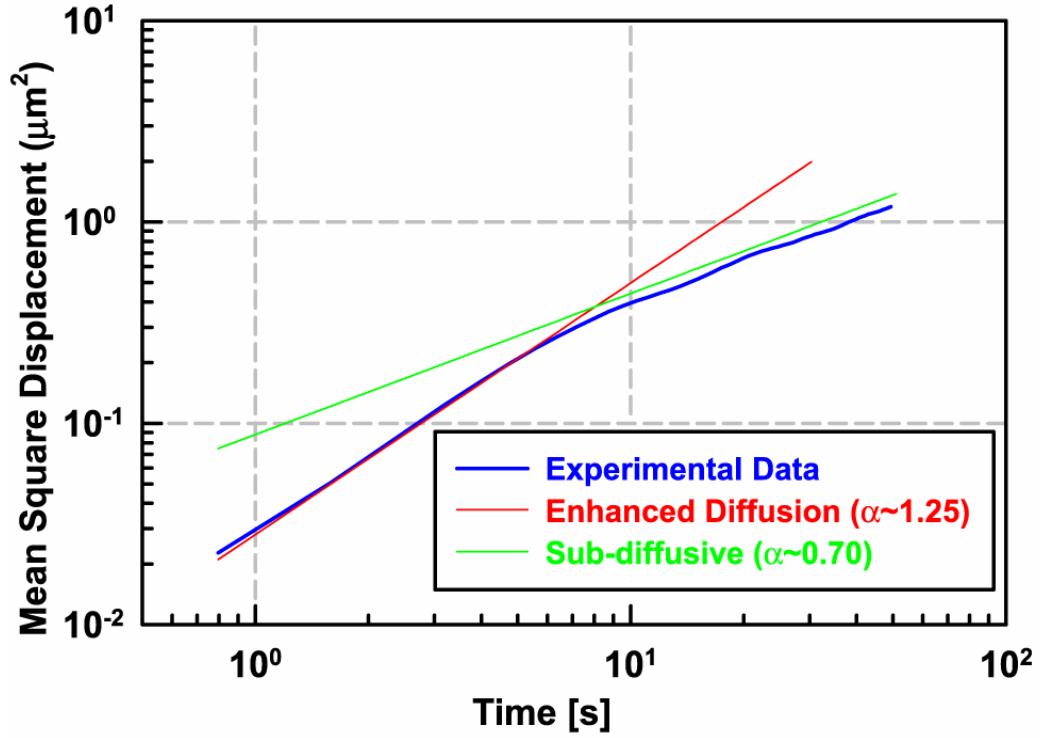


**Figure 3.1:** Plot of mean square displacement of polyplex-loaded endosomes as a function of time lag. Crossover from enhanced diffusive motion ( $\alpha > 1$ ) to subdiffusive motion ( $\alpha < 1$ ) occurs around seven seconds.

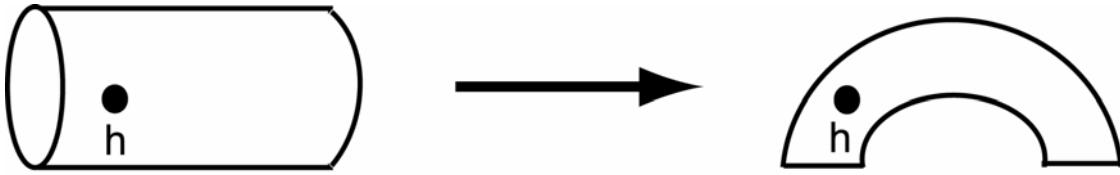


**Figure 3.2:** Cartoon of what happens to a given point,  $h$ , along a MT filament as thermal and other motions cause bending and deformation of the MT network. The overall movement of  $h$  is constrained by neighboring monomers.

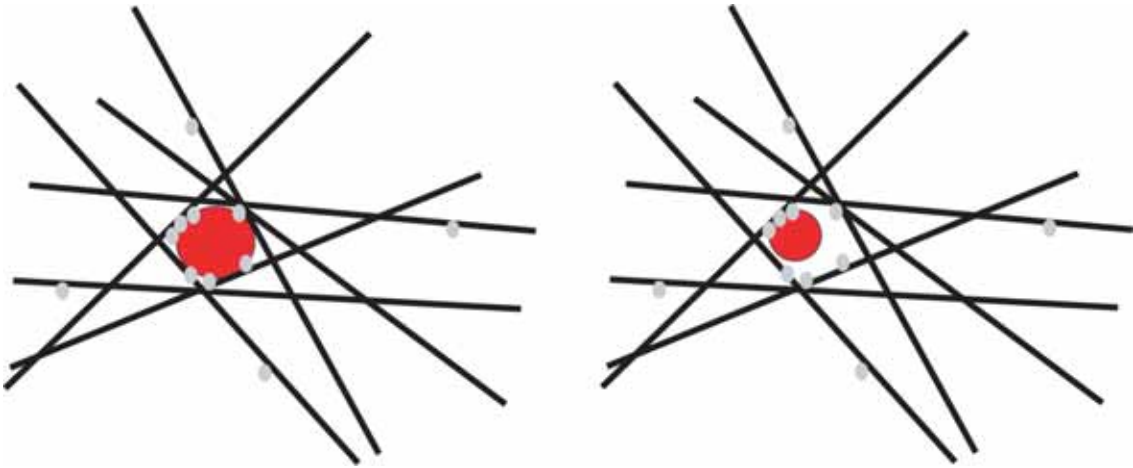


**Figure 3.3:** Schematic of particles embedded within the microtubule mesh. A large particle (left) is completely trapped in between the MT mesh and must push the filaments out of the way in order to move, while the smaller particle (right) can wiggle between the MT filaments.

### 3.5 References

1. Schliwa, M. and G. Woehlke, *Molecular motors*. Nature, 2003. **422**(6933): p. 759-65.
2. Gross, S.P., M.A. Welte, S.M. Block, and E.F. Wieschaus, *Coordination of opposite-polarity microtubule motors*. J Cell Biol, 2002. **156**(4): p. 715-24.
3. Kural, C., H. Kim, S. Syed, G. Goshima, V.I. Gelfand, and P.R. Selvin, *Kinesin and dynein move a peroxisome in vivo: a tug-of-war or coordinated movement?* Science, 2005. **308**(5727): p. 1469-72.
4. Welte, M.A., *Bidirectional transport along microtubules*. Curr Biol, 2004. **14**(13): p. R525-37.
5. Kulkarni, R.P., D.D. Wu, M.E. Davis, and S.E. Fraser, *Quantitating intracellular transport of polyplexes by spatio-temporal image correlation spectroscopy*. Proc Natl Acad Sci U S A, 2005. **102**(21): p. 7523-8.
6. Caspi, A., R. Granek, and M. Elbaum, *Enhanced diffusion in active intracellular transport*. Phys Rev Lett, 2000. **85**(26 Pt 1): p. 5655-8.
7. Caspi, A., R. Granek, and M. Elbaum, *Diffusion and directed motion in cellular transport*. Phys Rev E Stat Nonlin Soft Matter Phys, 2002. **66**(1 Pt 1): p. 011916.
8. Tolic-Norrelykke, I.M., E.L. Munteanu, G. Thon, L. Oddershede, and K. Berg-Sorensen, *Anomalous diffusion in living yeast cells*. Phys Rev Lett, 2004. **93**(7): p. 078102.
9. Suh, J., D. Wirtz, and J. Hanes, *Real-time intracellular transport of gene nanocarriers studied by multiple particle tracking*. Biotechnol Prog, 2004. **20**(2): p. 598-602.

## **Chapter 4: Single Cell Kinetics of Intracellular, Non-Viral, Nucleic Acid Delivery Vehicle Acidification and Trafficking**

### **4.1 Abstract**

Mechanistic understanding of the intracellular trafficking of non-viral nucleic acid delivery vehicles continues to remain elusive. A live, single cell-based assay is described here that is used to investigate and quantitate the spatiotemporal, intracellular pH microenvironment of polymeric-based nucleic acid delivery vehicles. Polycations such as polyethylenimine (PEI), poly-L-lysine (PLL), beta-cyclodextrin-containing polymers lacking or possessing imidazole termini (CDP or CDP-imid), and cyclodextrin-grafted PEI (CD-PEI) are used to deliver an oligonucleotide containing a single fluorophore with two emission lines that can be employed to measure the pH. Delivery vehicles were also sterically stabilized by addition of poly(ethylene glycol) (PEG) and investigated. The intracellular trafficking data obtained via this new methodology show that vectors such as PEI, CD-PEI, and CDP-imid can buffer the endocytic vesicles, while PLL and CDP do not. Additionally, the PEGylated vectors reveal the same buffering capacity as their unstabilized variants. Here, the live cell, spatiotemporal mapping of these behaviors is demonstrated and, when combined with cell uptake and luciferase expression data, shows that there is not a correlation between buffering capacity and gene expression.

## 4.2 Introduction

There is renewed interest in replacing viral vectors with biocompatible, polymeric vectors for gene delivery and potential gene therapy in humans because of recent difficulties and costs with viral delivery vectors [1, 2]. Although viruses can be useful for *ex vivo* gene delivery, they present many problems for systemic, *in vivo* use, including stimulation of immune responses, potential pathogenicity, lack of designable targeting to specific tissues and cell types, and cost of manufacturing. By comparison, the polymeric vectors can be prepared so that they do not elicit an immune response and are capable of carrying nucleic acids of virtually any size. Additionally, the synthetic delivery vehicles can be targeted to specific cells using appropriate ligands [3-6].

The delivery efficiency of non-viral vectors is much lower than with viral vectors. Increasing the intracellular delivery efficiency of non-viral vectors remains one of the major challenges in non-viral nucleic acid delivery. For effective delivery, the vector must first reach the cell of interest. Once internalized by receptor-mediated endocytosis, the delivery system should actively transport the nucleic acid out of the endocytic pathway and allow for movement into the nucleus. At some point during the delivery process, the non-viral vector must release the nucleic acid payload, although it is unclear where unpackaging should occur to enable the most effective delivery. Thus, the synthetic vector must perform multiple functions for effective intracellular trafficking [7-9].

An important process of the intracellular trafficking of non-viral delivery vehicles is their behavior in the endocytic pathway. The vehicles enter into this pathway by endocytosis and must escape in order to avoid degradation by the lysosomal system [10-

12]. Little is known about the spatiotemporal pH changes that the vectors face as they travel intracellularly or how these changes affect delivery and expression [13, 14]. Certain polymers, such as polyethyleneimine (PEI), are said to exhibit a “proton sponge” effect since they have titratable amine groups (pKa values in the range of 4-7) and have the ability to buffer pH changes as endocytic vesicles acidify [15]. Other polymers, such as poly-L-lysine (PLL) or beta-cyclodextrin-containing polymers (CDP), do not possess this ability [16]. Thus, it is important to understand how the delivery vectors respond to pH changes in the endocytic pathway and how those responses affect export to the cytoplasm to allow the cytoplasmic transport and nuclear delivery of the nucleic acid.

Prior studies examining endosomal pH changes utilized flow cytometry to look at averages of hundreds of cells simultaneously for different types of polyplexes (PLL and PEI) [10, 17] or employed an indirect approach that depended on colocalization of dextrans [18]. Here, we develop a new methodology to monitor the spatiotemporal pH experienced by nucleic acids in single cells using polymeric delivery vehicles. Our work differs from previous nucleic acid delivery studies in that we employ a single pH-sensitive fluorophore, SNARF-4F, directly conjugated to the nucleic acid of interest. This method avoids concerns about relative labeling density or interactions between multiple fluorophores, makes no assumptions regarding colocalization, and directly evaluates the pH microenvironment of the nucleic acid of interest. While valuable, previous studies involving average values from numerous cells do not offer the specificity of the single cell approach described below. Also, the delivery particles that are in different locations in the cell, or endocytosed at different times, cannot be distinguished by cell averaging methods. In contrast, the single cell analysis method we

present here using confocal laser scanning microscopy allows for direct examination of uptake of delivery particles in single cells in real time. Particles at different locations in the cell can easily be identified and pH differences quantified, as nuclear transport of all types of particles is rather slow and it can take on the order of tens of minutes for them to travel from the periphery of the cell to the nucleus.

Identifying pH differences as a function of delivery particle chemical composition and location within the cell will be important for a better understanding of how trafficking occurs and may assist in the design process and search for more efficient delivery vectors. Here, we show that the pH microenvironment can be correlated to transfection progression and particle location through direct visualization. This method allows for monitoring of the entire pathway from early internalization onwards and can be directly visualized in real time to measure individual differences among the cells.

### **4.3 Results**

#### **Fluorescence pH Assay**

The emission spectrum of SNARF-4F varies as a function of pH and has two peaks, one at 575 nm that increases in intensity as the pH declines, and one at 650 nm that increases in intensity as the pH increases; the crossover occurs at ~620 nm (Figure 4.1a). Thus, SNARF-4F can be used alone to monitor the pH in the range of 4-8 and is precisely the region useful for following the intracellular trafficking in cells when the trafficking involves the endocytic pathway. SNARF-4F was conjugated to the 5' end of an RNA phosphorothioate oligonucleotide, and the pH sensitivity of the conjugate was observed regardless of whether the labeled oligonucleotide was free in solution or was

bound by a cationic polymer and condensed into delivery particles. SNARF-4F signals are approximately the same pH value independent of whether or not they are conjugated to the nucleic acid, bound in a delivery vehicle, or present as free conjugate (Figure 4.1b). The labeled oligonucleotide was used to prepare particles with a variety of non-viral gene delivery vectors; for most systems examined, the resulting particles were  $\sim 100 \pm 25$  nm in size (Figure 4.2), and the oligonucleotide exhibited stability against serum when packaged in all the delivery particles (data not shown). The intracellular trafficking of these fluorescently-labeled particles were monitored in cultured cells as shown below.

To measure pH changes in cells via confocal microscopy, a META attachment was employed to separate the fluorescence emission into three wavelength bins (569-601, 601-633, and 633-687 nm). In order to generate a pH calibration curve, PLL and PEGylated CDP particles were prepared with the SNARF-4F RNA conjugate and were incubated in buffers with pH ranging from 4.2-8.1 and directly visualized under the microscope. The pH of the environment was quantitated by measuring the SNARF-4F emission in all three bins and sequentially calculating the ratios of all three bins compared to each other. The ratios did not differ significantly for PLL and PEGylated CDP particles in solution, and the data were combined to generate a single calibration curve. It was determined that the 633-687/569-601 nm ratio was the most sensitive to pH changes. An exponential curve was fit to these data points to determine an equation for calculating pH from the fluorescence intensity ratios, which was then used to determine intracellular endosomal pH values (Figure 4.1c).

By labeling the nucleic acids and not the delivery vectors, the assay determines the pH environment of the delivered nucleic acids whether bound to the delivery vector

or free in solution. It is relatively straightforward to directly visualize the SNARF-4F fluorescence when it is in a particle (Mishra et al. show high resolution TEM and fluorescent confocal microscopy results that confirm vesicle containment of intact particles using some of the vector systems employed here [19]), as the signal appears as a round cluster. Figure 4.3 shows an example of intact PLL polyplexes after 4 hours incubation and PEI polyplexes after 24 hours incubation imaged within different regions of the cell. The pH is depicted colorimetrically in this image; those polyplexes experiencing a lower pH environment appear more strongly blue colored whereas those experiencing a higher pH appear more strongly red colored. Diffuse staining indicative of unpackaged SNARF-oligonucleotide was not observed in these experiments, suggesting that unpackaged conjugate is diluted below the detection limit.

### **Intracellular pH Measurements**

HeLa cells were exposed to the delivery particles for 2 hours to allow for uptake and trafficking. While this time may seem long for endocytic processes, numerous reports have indicated that particle uptake and trafficking is notably slower [6, 10]. The media was then replaced to remove most of the free particles in solution and the cells were incubated for up to 24 hours before imaging. Because of the direct nature of our assay, it is not necessary to completely remove the free particles; in fact, particles that have entered more recently can be visualized and the endosomal pH values individually quantitated.

A major advantage of direct visualization is that different regions of an individual cell can be quantitated separately and not averaged into a bulk measurement. We have

found that early in the transfection process (less than 4 hours), there appear to be regional differences in pH values within the cell (Figures 4.3 and 4.4). Specifically, the cytoplasm can be divided into three regions – region I: within 2  $\mu\text{m}$  of the cell membrane; region II: the cytoplasmic region between the other regions; and region III: within 2  $\mu\text{m}$  of the nuclear membrane. We did not observe intact particles or labeled nucleic acids within the nucleus for any imaging condition. This is not unexpected for the CDP delivery systems, as Mishra et al. have shown that intact particles do not enter the nucleus (only released nucleic acids can be visualized in the nuclear compartment) [19].

As the particles are first internalized, their pH is uniformly high in region I for all examined classes of delivery vectors; however, the pH drops for PLL, CDP, and lipofectamine particles as they travel towards the nucleus (Figures 4.5 and 4.6). The reduction in pH for PLL is rather rapid and is complete by 2 hours after initial incubation for those particles that reach region II. For the CDP vector, particles in region I are still at neutral pH after four hours, those in region II are at an average pH of  $\sim 6.1$  with significant variability in pH, while those close to the nucleus have acidified by four hours to an average pH of 5.2. Lipofectamine particles also display such an acidification, reaching an average pH of 4.6 by 16 hours. Again, the average value does not tell a complete story; certain particles in region II have fully acidified, while others are slower to do so.

In contrast, PEI particles display relatively consistent pH values for each time point, independent of region. Over time, the PEI particles do acidify from pH  $\sim 6.6$  to pH 5.8; however, the decrease is not as prominent as for PLL or CDP, which have acidified in all three regions by 24 hours. Even at this time point, however, there are still a few

cells (~1-4%) that show particles that are not acidified, possibly because they have entered the cells only recently; these particles are indicated as being in region IV (see Figure 4.6). CD-IPEI exhibits acidification to pH ~5.5 rather quickly, even in region I. However, it does not fully acidify below this pH, even after 16 hours.

Although CDP particles do not buffer pH, modifications can be introduced to allow for buffering capacity. Conjugation of an imidazole group to the polymer termini produces CDP-imid, a vector that displays a limited buffering of pH. The acidification of CDP-imid particles occurs gradually, and even after 16 hours, the average endosomal pH was ~6.3. Further acidification was observed to occur, with the average pH reaching ~6 by 24 hours. Administration of chloroquine in conjunction with CDP particles resulted in a comparable buffering effect, with the pH remaining at ~6.6 even after 16 hours.

Three types of particles (CDP, CDP-imid, PEI) permitted facile comparison between PEGylated and unPEGylated variants. Interestingly, differences between PEGylated and unPEGylated variants of the same polyplex type were minor. For instance, at 16 hours after transfection, the average pH for PEGylated CDP-imid was ~6.4, while it was ~6.3 for the unPEGylated CDP-imid (Figure 4.4). Similar results were obtained for the other types of particles at each time point (data not shown).

### **Transfection Data**

To explore the implications of the buffering behavior on the gene delivery efficiency of the examined delivery vectors, the delivery of luciferase plasmid DNA was employed. The examined delivery vectors generate similarly-sized particles regardless of whether they are used to condense the SNARF-labeled oligonucleotide or plasmid DNA

(Figure 4.2). The gene delivery activity of the various delivery vectors was assessed by transfecting cells with firefly luciferase-expressing plasmid DNA and assaying for luciferase expression (Figure 4.7). DNA uptake by cells was quantified using fluorescently-labeled plasmid DNA and analysis by flow cytometry (Figure 4.8). The cellular fluorescence intensity can be correlated with relative uptake of plasmid DNA because the fluorescent label used (YOYO-1) was shown on a fluorimeter to be pH-insensitive (data not shown).

#### **4.4 Discussion**

The fluorescence-based pH assay described herein provides the ability to follow and track individual particles within cells over time and thus gives insight into the nature of their trafficking within the cell. The development of this methodology was enabled by the facile labeling of the oligonucleotide and by the preservation of the label's pH sensitivity even when the conjugated oligonucleotides were condensed into delivery particles. Here, only a single fluorophore is used per nucleic acid molecule, thus avoiding the issue of uneven labeling (of nucleic acids or within particles) that can be present with two-fluorophore experiments.

Individual cells are examined in this assay, and particles residing in different zones within a given cell can be visualized and their local pH environment examined. Specifically, a "pH map" of the delivery vectors can be determined as a function of the time-dependent spatial locations (i.e., close to the cell membrane, near the nucleus, or in between) of the vectors as they traverse the cell. The relevance of this approach is demonstrated, for example, by the small percentage of cells showing PEI particles in

region IV (those that are not acidified even after 24 hours). In a bulk assay, this information would be lost, with such individual differences combined into a statistical average. Here, we directly access spatiotemporal information and use it to refine models of intracellular trafficking of delivery particles.

The current model of delivery vehicle transport through the cell suggests that the particles are first internalized within endosomal compartments, after which the compartments mature from early endosomes to late endosomes and finally to lysosomes; the pH of these compartments progressively declines until reaching pH ~4.5 [10, 17, 20]. Our results support this model of trafficking through the endocytic pathway by demonstrating and quantifying the reduction in pH experienced by delivered nucleic acids as they move through the cell. The ability of the delivery vehicles to circumvent or alter the steps of the endocytic pathway is of interest for understanding how efficiencies and transport rates are affected. Specifically, those particles that contain titratable amines at pH values experienced in the endocytic pathway that range between approximately 4 and 7 (such as PEI) are thought to buffer the endosomal compartments and prevent maturation into lysosomes. The buffering thus affects delivery. It is believed that those polymers that can buffer act as “proton sponges” and promote osmotic swelling and lysis of endosomes. This lysis is speculated to allow endocytic pathway release that thus improves delivery efficiency [11, 15].

In general, these models have been developed without an assessment of the spatial and temporal localization of the relevant pH changes. Each endosome is an individual entity and acidifies at a different rate that is dependent upon cell type and other factors. Here, we specifically examine acidification within HeLa cells and find that spatial

differences are prominent for CDP and PLL particles at early times (before 4 hours). When these particles have trafficked for more than 12 hours, they reach a pH of roughly 4.8-5.0 and show little difference regardless of position within the cell. These low pH values suggest that the endosomes have fully acidified and are at the lysosomal stage. For PEI, the spatial localization is less important than temporal differences, and the pH values are relatively constant throughout the cell for a given time point. After 24 hours, the pH is ~5.8, indicating that full acidification does not occur. For CDP-imid particles, the pH values are also relatively constant throughout the cell for a particular time point; the imidazole group acts to buffer the pH (relative to CDP particles) and the pH remains above 6 for almost 24 hours (similar to PEI).

The uptake, intracellular trafficking, and gene delivery efficiency of PEGylated gene delivery particles differs from that of their unPEGylated variants [19]. Comparing PEGylated CDP, PEGylated CDP-imid, and PEGylated PEI particles to their unPEGylated variants, we observe no significant differences in the extent or kinetics of acidification. This result indicates the PEG coating does not affect acidification or progression through the endocytic pathway. Retention of buffering capacity with the PEGylated particles is significant because systemic *in vivo* administration of non-viral gene delivery particles will require PEGylation or other means of salt-stabilization.

The relatively high delivery efficiency of PEI has been linked to its ability to act as a “proton sponge,” and there is evidence to support this hypothesis [11, 15]. Improvements in non-viral transfection efficiency in the presence of chloroquine have also provided credence to the “proton sponge” hypothesis. It is shown here that chloroquine confers significant buffering activity to a vector system that otherwise

readily acidifies. However, by comparing vectors with and without pH buffering capacity, it is clear that buffering capacity alone does not necessarily correlate with gene delivery efficiency. Despite similar pH buffering capacity, the three types of PEGylated particles generate reduced expression relative to their unPEGylated variants. The terminal imidazole group confers significant pH buffering capacity to CDP-imid that is not present for CDP; at the charge ratio examined here, the buffering activity does not correlate with significant improvements in transfection efficiency. Conversely, the significant buffering capacity of PEI is not seen in CD-IPEI, but both vectors give strong expression, consistent with published results [21]. The lack of correlation between buffering and gene expression has been observed by others [13, 22]. Forrest et al. revealed that acetylated PEI gave both reduced buffering capacity and improved transfection efficiency relative to unmodified PEI [22]. Also, recent reports have shown that new polymeric vectors designed with buffering capacity do not necessarily perform well as gene delivery vectors [13, 23].

The data gathered here by a single-cell approach can be analyzed in aggregate for comparison with prior studies that have utilized flow cytometry to compile aggregate data. Our results in HeLa cells and those of Akinc and Langer in NIH 3T3 cells [17] both indicate that PEI shows a strong buffering capacity relative to PLL. This is consistent with a simple model where the titratable amines of PEI that are not present on PLL confer buffering capacity. In contrast, Forrest and Pack observed almost the opposite behavior, with PEI showing little to no buffering capacity as a function of cell line and PLL particles showing sharp variability as a function of cell line [10], including almost no reduction in pH in HepG2 cells even 15 hours after transfection. Of note, fluorescently-

labeled nucleic acids were utilized in our study and that of Akinc and Langer, while Forrest and Pack conducted their experiments by fluorescently-labeling the delivery vectors.

It has been widely observed that chloroquine treatment produces increases in transfection efficiency for many types of non-viral gene delivery particles [16, 24], as seen in this study with CDP particles. The mechanism of this improvement is unclear. One possibility is that high intracellular or intravesicular concentrations of chloroquine induce the unpackaging of delivered nucleic acids from delivery vectors [24, 25]. Chloroquine is also known to buffer the vesicles of the endocytic pathway [26], and this buffering may inhibit the transfer of endocytosed gene delivery particles to lysosomes. Our results do not resolve the questions surrounding this mechanism, but they do show that chloroquine treatment inhibits acidification of intracellular CDP particles in HeLa cells. In the bulk assay of Akinc and Langer, chloroquine buffered the average pH of PLL particles in NIH 3T3 cells. In contrast to our results, their data included a sharp fluctuation where the average pH of the intracellular PLL particles dropped sharply to pH ~4 in the first two hours before rising upward in the next two hours [17]. The kinetics of chloroquine uptake may differ for the two cell lines. Although Forrest and Pack did not observe buffering by PEI, their bulk assay showed significant buffering when PEI transfection was accompanied by chloroquine [10].

When acidification of endocytic vesicles is buffered by gene delivery particles, the vesicles still progress through the endocytic pathway. PEI, for example, is shown here to demonstrate strong buffering capacity in a gene delivery particle. Lecocq et al. used centrifugation methods to show that intracellular PEI eventually colocalizes with the

lysosomal marker cathepsin C [27]. Kichler et al. observed that in vitro reporter gene expression was impaired when endosome acidification was inhibited with bafilomycin A1, indicating that, despite its buffering activity, PEI relies on the acidification process for transfection [28]. Similarly, Singh et al. histidylated two cationic lipids to confer pH buffering and found that gene delivery with these lipids was less efficient in the presence of bafilomycin A1 [29].

Single-cell methods can supply new information on intracellular trafficking that will be useful in the design of improved gene delivery vectors. For example, various researchers have sought to enhance intracellular vector unpackaging by preparing acid-labile polycation-DNA particles [14, 30]. A detailed description of the spatial and temporal pH changes experienced by these particles in cells would indicate the probable intracellular location(s), timing, and extent of the particle degradation, thus facilitating refinement of the pH-sensitive vectors.

The compact, intense clusters of SNARF-4F fluorescence observed within cells are assumed to represent nucleic acids contained within vesicles. The small size of the SNARF-oligonucleotide suggests that the fluorescent signal from unpackaged intracellular oligonucleotides would appear diffuse. The absence of such diffuse staining could indicate that the majority of delivered nucleic acids remained within the delivery particles [19]. Alternatively, the unpackaged oligonucleotide may present a signal so diffuse that it is below the detection limit, or it may be rapidly degraded and/or expelled from cells.

One question that arises is why there might be any particles still remaining in region I (near the cell membrane) at 12 or even 24 hours after transfection. One plausible

explanation is that these particles have entered only a few hours earlier and have not had time to acidify. Particles in this category might have been stuck on the outer surface for hours before being endocytosed. However, this does not fully explain the existence of very low pH endosomes near the cell membrane. A second possibility is that such endosomes are trafficking very slowly towards the nucleus or are traveling in a random trajectory and have fully acidified but happen to be close to the membrane when imaged. The particles must be transported along microtubules within endosomes in order to navigate the cytoplasm; the trajectories of these endosomes are often stochastic [31, 32].

The advantages of the method presented here include the ability to directly visualize each cell and follow the internalization and endosome trafficking of delivery vehicles over time. This approach avoids or minimizes some of the problems of bulk imaging by flow cytometry that include quantitation of dead cells, presence of particles on the surface of the cell, and suppression of variability by intracellular region. The dynamics of the uptake and acidification process can be quantitated in both time and space, and any escape or other behavior can be monitored. By analyzing single cells, any variability in the process can be revealed and not buried in the overall average. This variability is especially evident at early times, as particles in certain spatial regions exhibit a broad range of pH values. We can also measure and segregate small subpopulations that would otherwise be combined into the statistical mean. Through the use of this assay, individual cells can be tracked for hours, and the spatial and temporal pH profile analyzed to better understand intracellular trafficking of non-viral gene delivery vectors. In summary, this new methodology has yielded data from which we have carried out further analyses of prior experiments performed in aggregate, quantified

the differences in buffering capacity among a variety of delivery vectors, revealed that PEGylation does not significantly affect buffering capacity, and verified that chloroquine can confer buffering to gene delivery particles. The results presented here raise further questions about the role of pH buffering in the endocytic pathway and its importance to gene delivery efficiency.

## 4.5 Materials and Methods

### *Labeled oligonucleotide*

A 21-base RNA phosphorothioate oligonucleotide was synthesized (Caltech Biological Synthesis Facility, Pasadena, CA) with sequence 5'-GACGUAACGGCCACAAGUUC-3'. The 5' end of the oligonucleotide was capped with the 5'-amino modifier 5 (Glen Research, Sterling, VA), supplying a 5' terminal primary amine to which an NHS-ester of the SNARF-4F fluorophore could be reacted. To carry out this reaction, the dry oligonucleotide was re-suspended in phosphate-buffered saline (pH 7.4). The pH-sensitive fluorescent molecule SNARF-4F-carboxylic acid (Molecular Probes, Eugene, OR) was converted to an NHS-ester by reaction with 1-ethyl-3-(3-dimethylaminopropyl)carbodiimide hydrochloride (EDC) (1:1 molar eq.) and N-hydroxysulfosuccinimide (sulfo-NHS) (5:1 molar eq.) in MES buffer (pH 6.0) for 15 minutes. Subsequently, the oligonucleotide was added to the reaction mixture (10:1 molar eq., SNARF-4F:oligonucleotide) and reacted for 2 hours at room temperature in the dark. The SNARF-4F-labeled oligonucleotide was purified from unreacted SNARF-4F with CentriSep 20 columns (Princeton Separations, Adelphia, NJ). In multiple reactions, the yield of labeled oligonucleotide was 50-60%.

*Delivery vectors*

The beta-cyclodextrin-containing polycation (CDP) and imidazole-terminated beta-cyclodextrin-containing polycation (CDP-imid) were synthesized as described previously [33]. Solutions of these cyclodextrin-containing polycations were prepared at 2.06 mg/mL in dH<sub>2</sub>O. 25 kDa branched polyethylenimine (bPEI) (Aldrich, Milwaukee, WI) solution was formulated at 0.067 mg/mL in 20 mM HEPES buffer with 5% glucose. Poly-L-lysine (Sigma) solution was prepared at 0.06 mg/mL in 0.3 M NaCl. Cyclodextrin-grafted linear polyethylenimine (CD-lPEI) was synthesized as described previously [21], and a solution was formulated at 10 mg/mL in dH<sub>2</sub>O. Lipofectamine (Invitrogen) was diluted to 0.025 mg/mL in Opti-MEM serum-free medium (Gibco/Invitrogen).

*Formulation of labeled complexes*

The SNARF-4F-labeled oligonucleotide was diluted in dH<sub>2</sub>O to a concentration of 0.1 mg/mL. Polycation-oligonucleotide complexes were prepared by adding a polycation solution (as described above) to an equal volume of SNARF-4F-oligonucleotide. Complexes were then incubated at room temperature for 30 minutes. These conditions produce complexes at an N/P ratio of 10/1 for CDP and CDP-imid, 5/1 for bPEI, and 3/1 for poly-L-lysine. Lipoplexes were prepared by adding lipofectamine at a concentration of 25 µg/mL in Opti-MEM to the nucleic acid at a concentration of 10 µg/mL in Opti-MEM.

### *PEGylation of complexes*

An adamantane-poly(ethylene glycol)5000 conjugate (AD-PEG) was prepared as previously described [33]. CDP complexes and CDP-imid complexes were salt-stabilized by the addition of 35 micrograms AD-PEG (100 mg/mL in dH<sub>2</sub>O) per microgram oligonucleotide. bPEI complexes were salt-stabilized by addition of 4 micrograms methoxy-PEG5000-succinimidyl propionate (Nektar, San Carlos, CA; 20 mg/mL in dH<sub>2</sub>O) per microgram oligonucleotide. Solutions were incubated at room temperature for an additional 30 minutes after PEGylation. For examples of these types of PEGylation methods and results of stabilization within cells see [21].

### *Cells*

HeLa cells were grown in 10-cm culture dishes (Becton-Dickinson) at 37°C in a humid 5% CO<sub>2</sub> atmosphere. Each dish held 10 mL of growth media which consisted of DMEM with 10% fetal bovine serum, 100 units/mL penicillin, 100 units/mL streptomycin, 10 mM HEPES, 0.1 mM non-essential amino acids, and 2 mM L-glutamine (Irvine Scientific). The cells were passaged once a week and plated onto glass-bottom tissue culture plates (Labtek) for each imaging experiment. The total medium volume per well was 0.7 mL after seeding, and the cells were incubated for 24 hours before transfection.

### *Fluorescence Microscopy*

An inverted Zeiss LSM 510 META confocal microscope was used for all fluorescence and brightfield measurements. A 63x oil objective (NA 1.4) was employed

for all measurements. Excitation of the SNARF fluorophore was achieved with the 543 nm line of the He-Ne laser line supplied with the microscope. The fluorescence signal was detected by the PMTs within the META detector after passing through a variable confocal pinhole set to 2 Airy units (chosen to maximize the S/N ratio while minimizing out-of-plane light). The META detector allows for the emitted wavelengths to be separated into  $\sim 10$  nm bins of light. For the SNARF-4F fluorophore, the collected emission light was separated into 3 distinct bins: 569-601 nm, 601-633 nm, and 633-687 nm.

#### *pH Calibration Assay*

Buffers with pH = 4.2, 5.0, 6.0, 7.0, and 8.0 were prepared as follows. The pH 4.2 and pH 5 buffers were made by adjusting the pH of a 0.2 M potassium acetate solution to the appropriate pH with glacial acetic acid. The pH 6.0 buffer was prepared by mixing 1.2 mL of 1 M  $\text{Na}_2\text{HPO}_4$  and 8.8 mL of 1 M  $\text{NaH}_2\text{PO}_4$ . The pH 7.0 buffer was formulated by mixing 5.8 mL of 1 M  $\text{Na}_2\text{HPO}_4$  and 4.2 mL of 1 M  $\text{NaH}_2\text{PO}_4$ . The pH 8.0 buffer was prepared by mixing 9.3 mL of 1 M  $\text{Na}_2\text{HPO}_4$  and 0.7 mL of 1 M  $\text{NaH}_2\text{PO}_4$ . The pH of these latter three buffers was adjusted with 6 M NaOH. To determine the pH calibration curve, PLL, CDP, and CDP-PEG particles were incubated as follows. 2  $\mu\text{L}$  of each polyplex solution (prepared as described above) were added to 100  $\mu\text{L}$  of each buffer and allowed to equilibrate for at least three hours. Each sample was then imaged under the microscope as described, and the intensity measurements for each of the three bins were collected. The intensity values were normalized with respect to the middle bin (601-633 nm emission light) to generate calibration curves for the different pH values.

The ratios of the intensity values of the 633-687 emission bin divided by those of the 569-601 emission bin do not differ significantly for all three types of particles at the same pH values; hence, we are able to use these ratios to determine intracellular pH.

### *In Vitro Transfection Imaging*

After 24 hours, the growth medium in each well was removed and replaced with an equal amount of Opti-MEM medium. 2  $\mu$ L of delivery particle-containing solution were then added to each well and placed in a 37°C incubator for 2 hours to allow for sufficient uptake. The cells were then imaged at 37°C, with the fluorescence emission collected into 3 channels as previously described. Cells with delivery particles at different locations and stages of transport were imaged to generate a “pH map” of the cell. Fluorescence intensity ratios were then calculated and compared to the calibrated pH values to determine the intracellular pH environment for each of the individual signals.

### *Plasmid uptake and expression*

The firefly-luciferase-expressing DNA plasmid pGL3-Control Vector (5256 bp) was obtained from Promega (Madison, WI) and amplified using the Ultramobius 1000 kit (Novagen). One day prior to transfection, HeLa cells were plated at a density of  $5 \times 10^4$  cells/mL in 24-well plates (1 mL/well). For transfection, polyplex solutions were diluted 10X in pre-warmed Opti-MEM serum-free medium (Invitrogen), while lipoplex solutions were applied as formulated (in Opti-MEM). Uptake was assessed four hours after transfection as described previously [19]. Briefly, cells were transfected in duplicate with

YOYO-1-labeled plasmid DNA, and the YOYO-1 fluorescence of viable cells was measured four hours after transfection using a FACScalibur instrument (Becton Dickinson, Franklin Lakes, NJ). Expression of firefly luciferase was assayed as previously described [34]. Briefly, the polyplex-containing medium was aspirated four hours after transfection and replaced with regular growth medium equal to the original volume, and luciferase assays were conducted in triplicate 48 hours after transfection.

### **Acknowledgements**

We thank Swaroop Mishra for the synthesis of the polyplexes used in this study and for conducting the FACS and luciferase expression assay data.

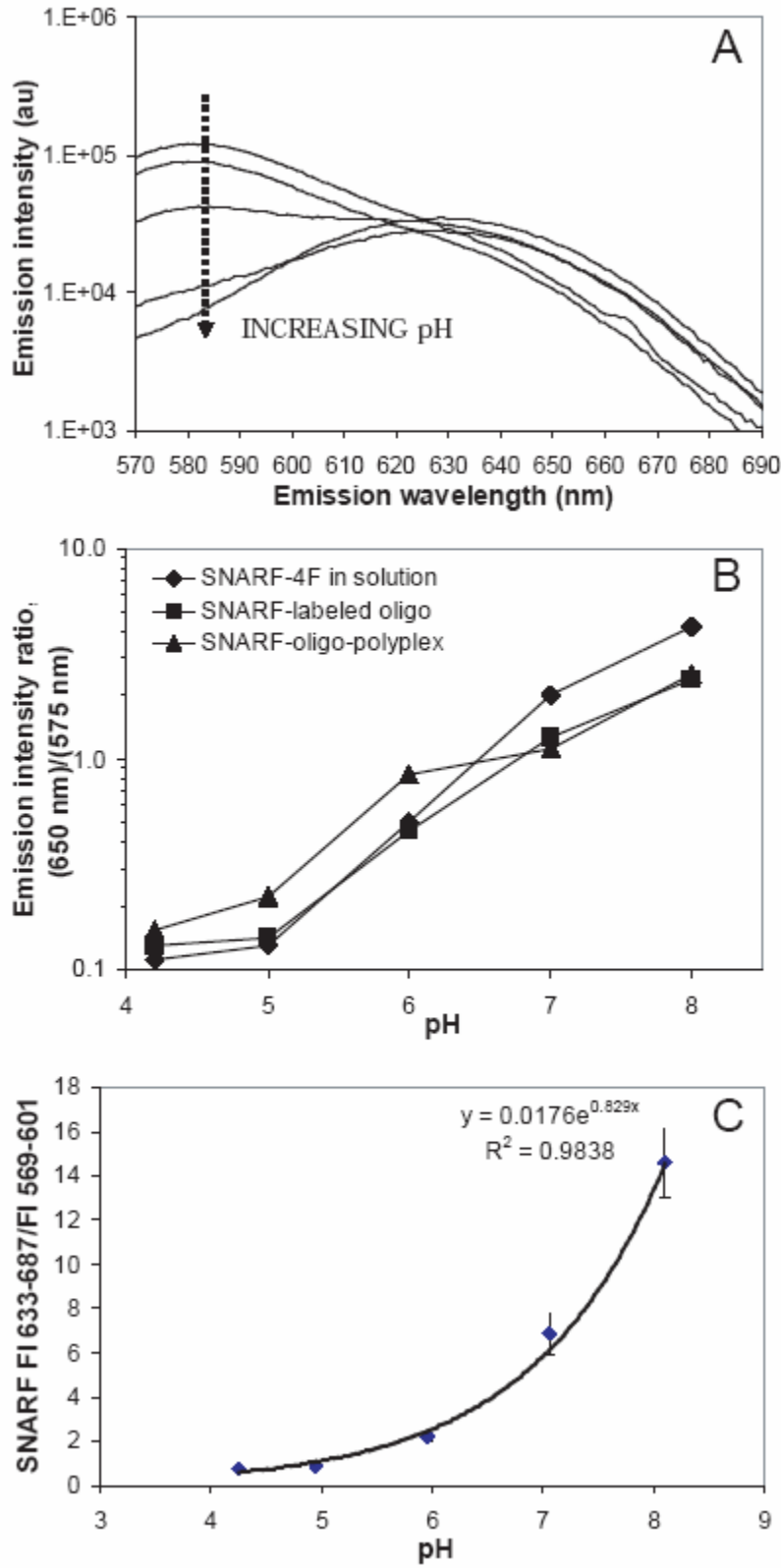
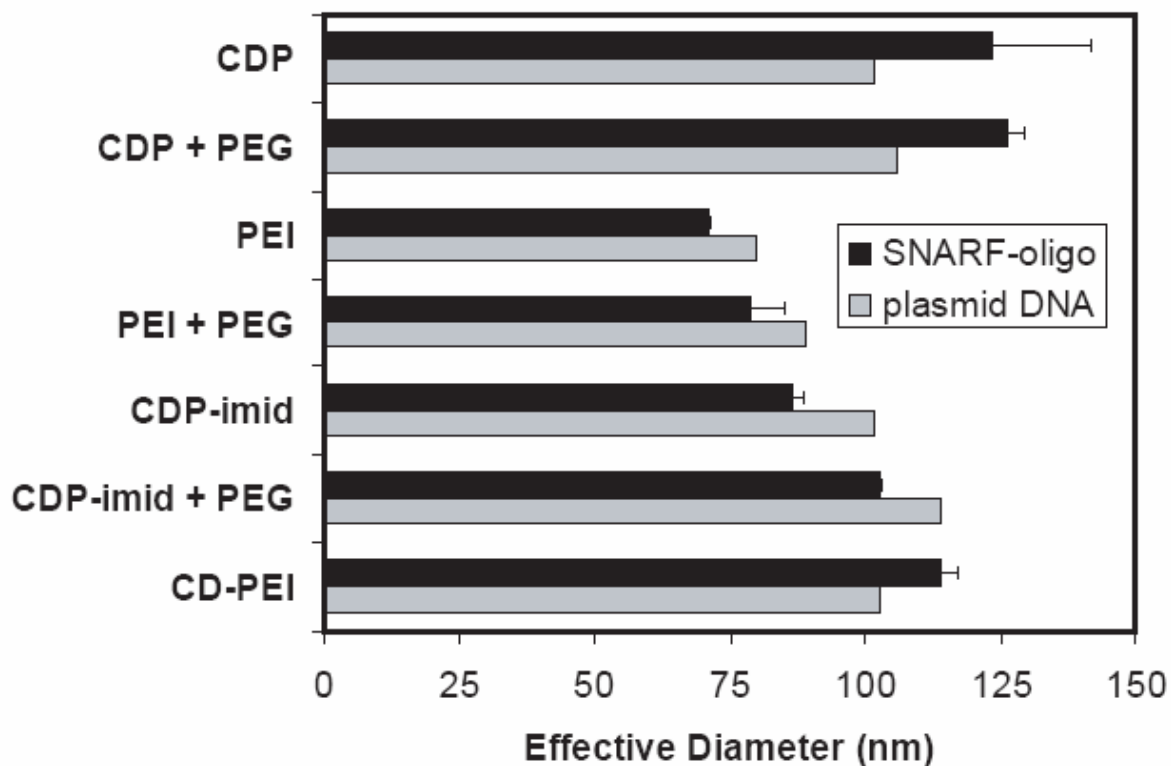
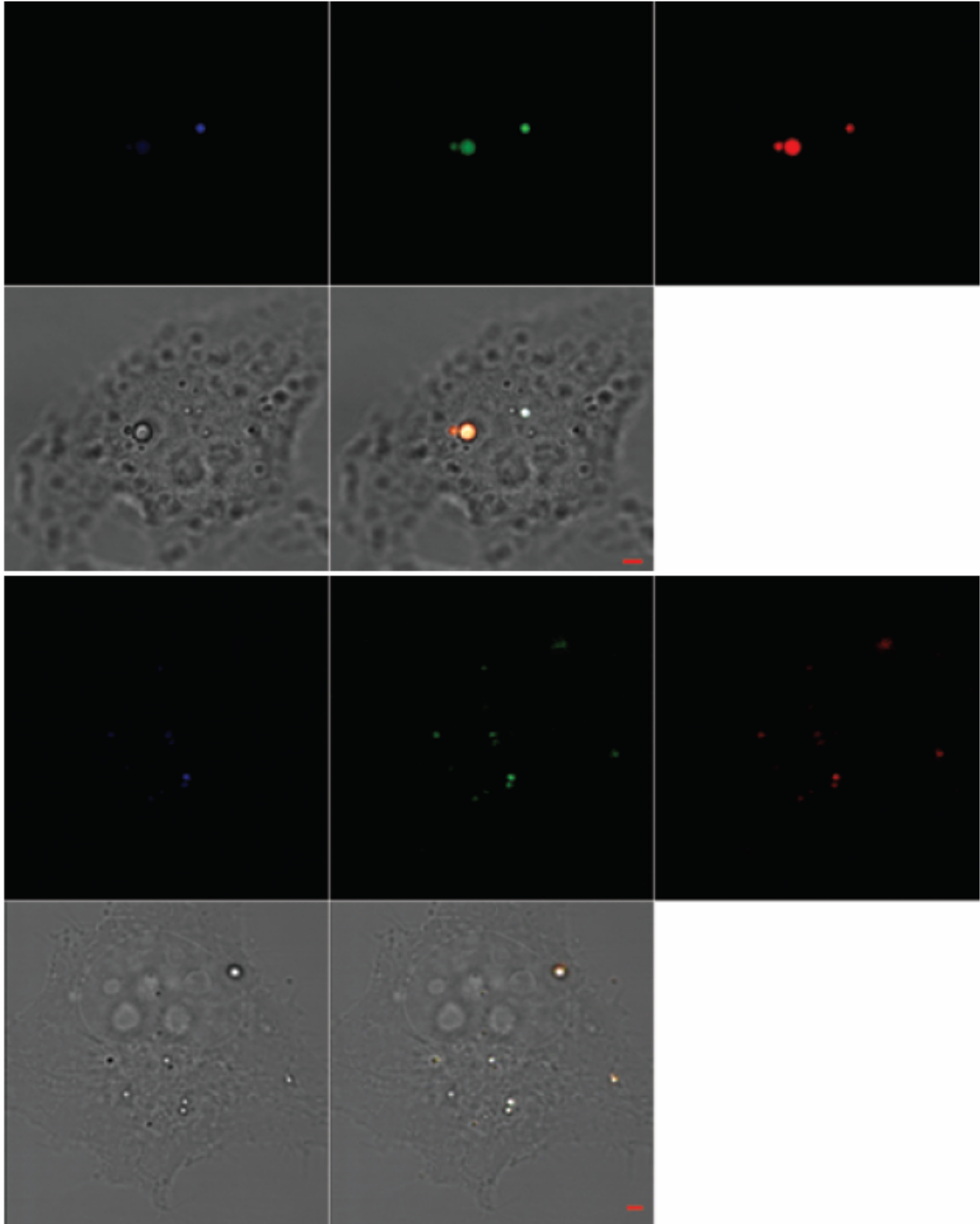


Figure 4.1:

- (a) Fluorescence emission spectra of SNARF-4F as a function of pH. At low pH values the peak at 595 nm is prominent, while the peak at 655 nm is low. As the pH rises, the 595 nm peak decreases in intensity, while the 655 nm peak rises to a maximum.
- (b) Ratio of emission intensities for SNARF-4F dye. Attaching the dye to oligonucleotides or complexing the labeled oligonucleotides into particles does not appreciably change the emission spectrum of the dye compared to free dye in solution.
- (c) Mean fluorescence signal from 633-687 nm divided by signal from 569-601 nm for SNARF-4F as a function of pH for different particles in buffered solutions (see text).



**Figure 4.2:** Average diameters of the various particles used in this study. Dynamic light scattering was employed to measure the effective diameters of the particles formulated. Most of these particles were formulated with an average effective diameter between 75-125 nm. Complexation of the polycation to either the SNARF-oligonucleotides or plasmid DNA resulted in particles of similar size.



**Figure 4.3:** (Top) Image of PLL particles within cells after two hours incubation. Blue represents the 569-601 nm channel, green the 601-633 nm channel, and red the 633-687 nm channel. In this case, the large spot has not acidified, while the smaller one to the right has acidified to pH 4.5. This image illustrates the inherent cell-cell variability of the uptake process, indicating that acidification does not occur uniformly or in a set time

window. (Bottom) Image of PEI particles in a cell after 24 hours incubation. The spots below the nucleus are at  $\sim$  pH 6, while the large one in the upper right corner is still at pH 7.5, suggesting that the particles in the upper right may have entered much later than the others. Scale bars = 1  $\mu$ m.

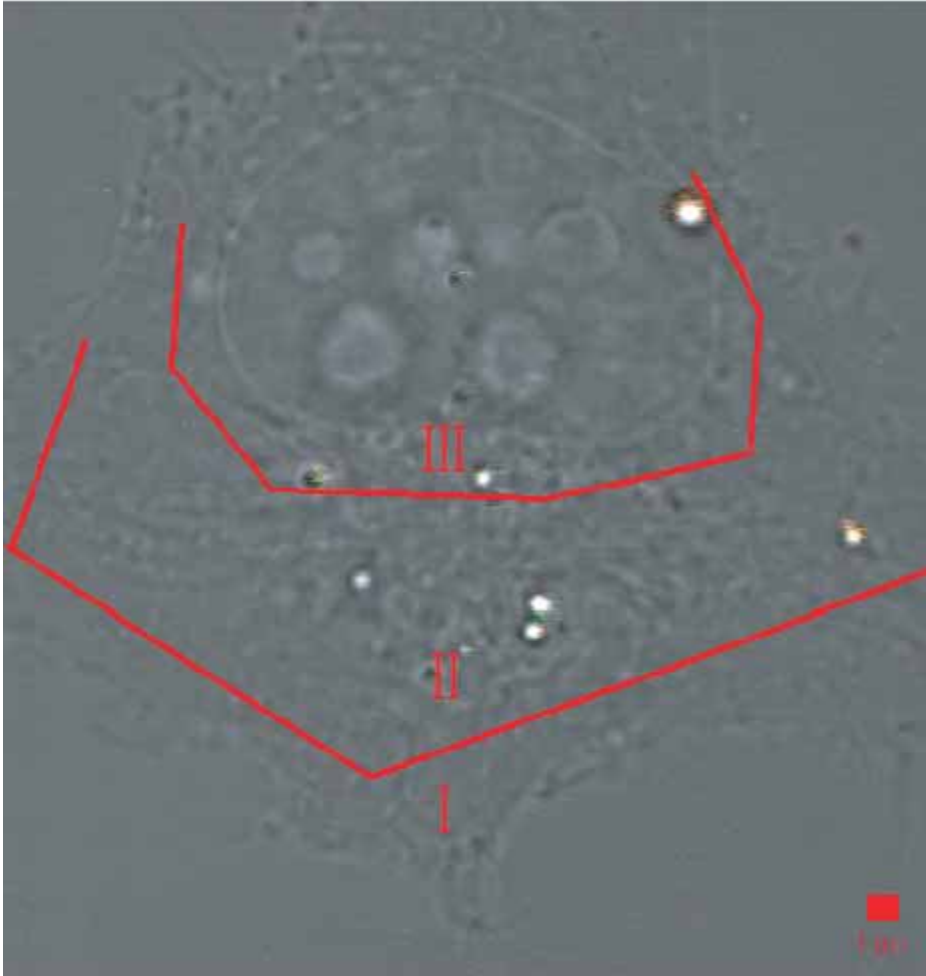


**Figure 4.4:** A schematic of a cell depicting the three regions (I, II, III) described in the text. Region I is the area of the cell within 2  $\mu\text{m}$  of the cell membrane, region III is the region within 2  $\mu\text{m}$  of the nucleus, and region II depicts the area in between. Scale bar = 1  $\mu\text{m}$ .

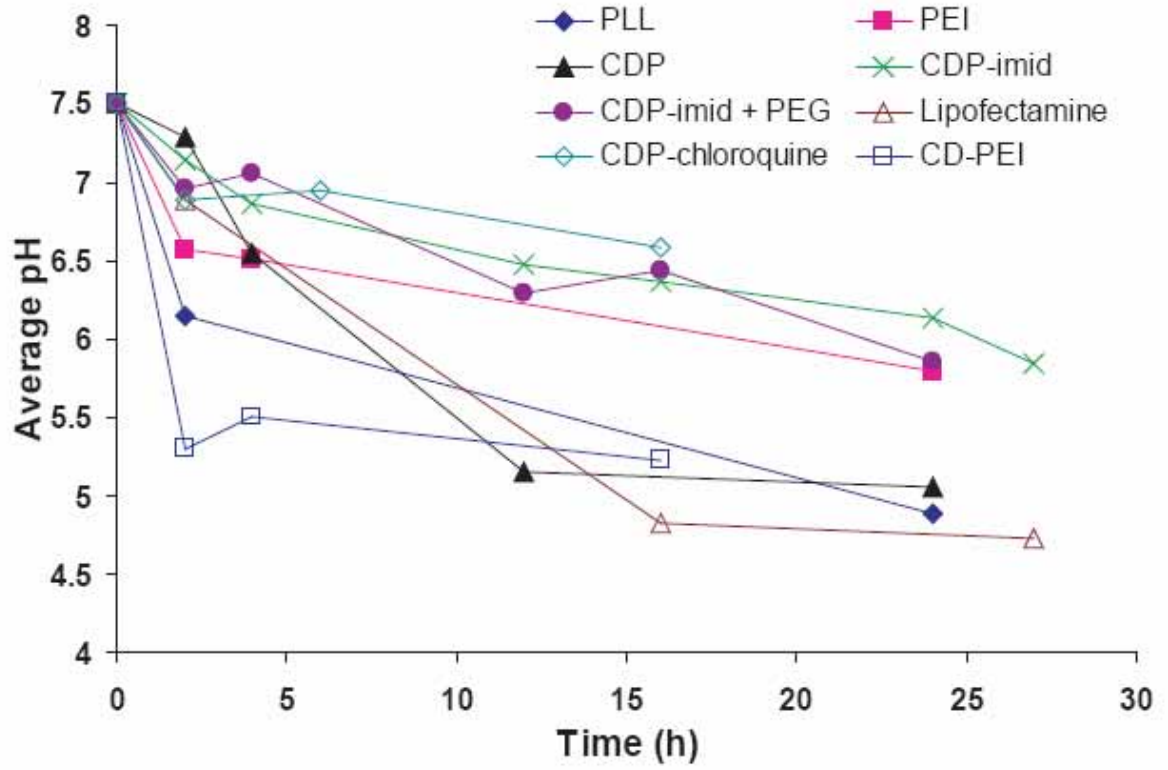


**Figure 4.5:** Plots of average pH of all cells and regions as a function of time.

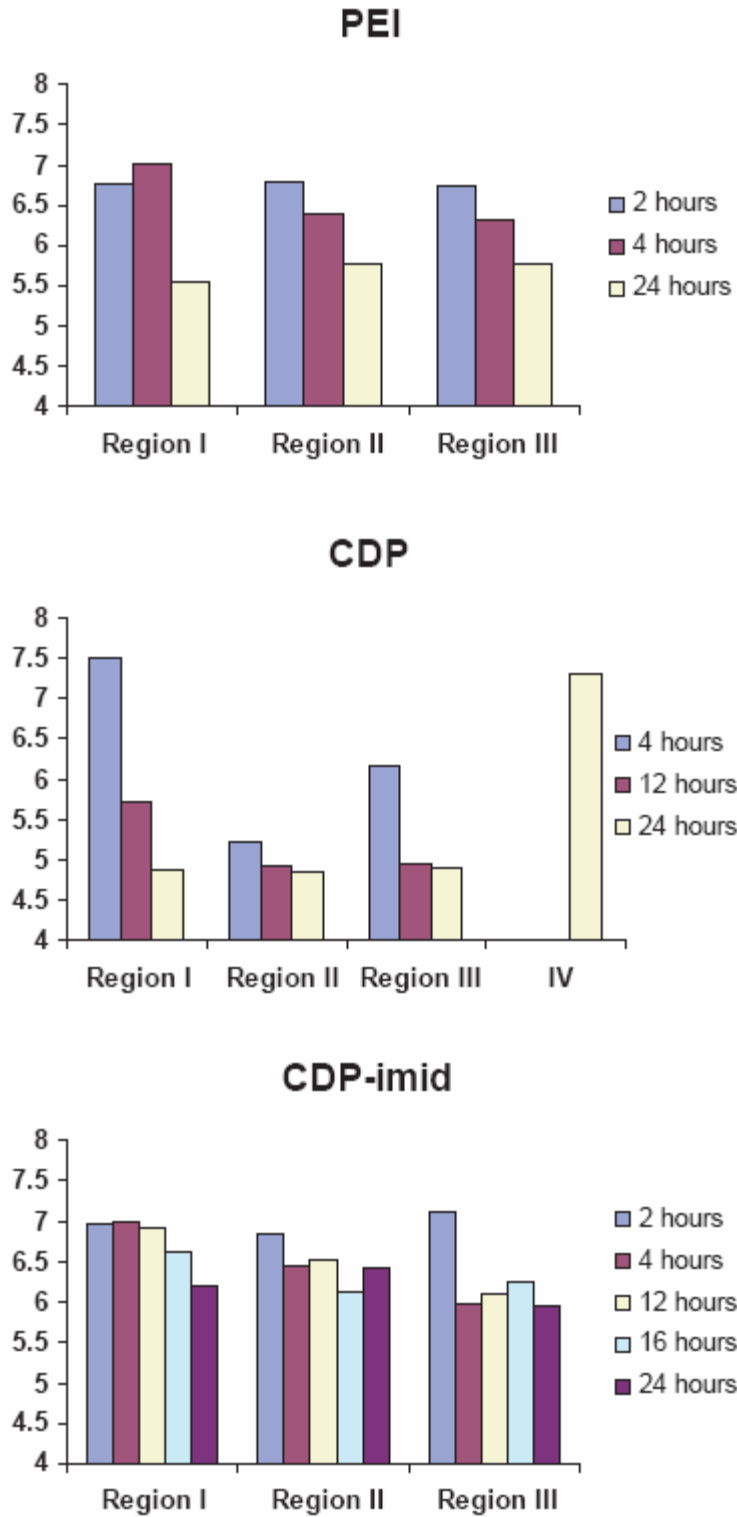


**Figure 4.6:** Regional pH values for PEI, CDP, and CDP-imidazole particles as a function of time and region within the cell. Greater variability can be seen for particles at earlier times and by region, highlighting the cell-to-cell variability inherent in these measurements.

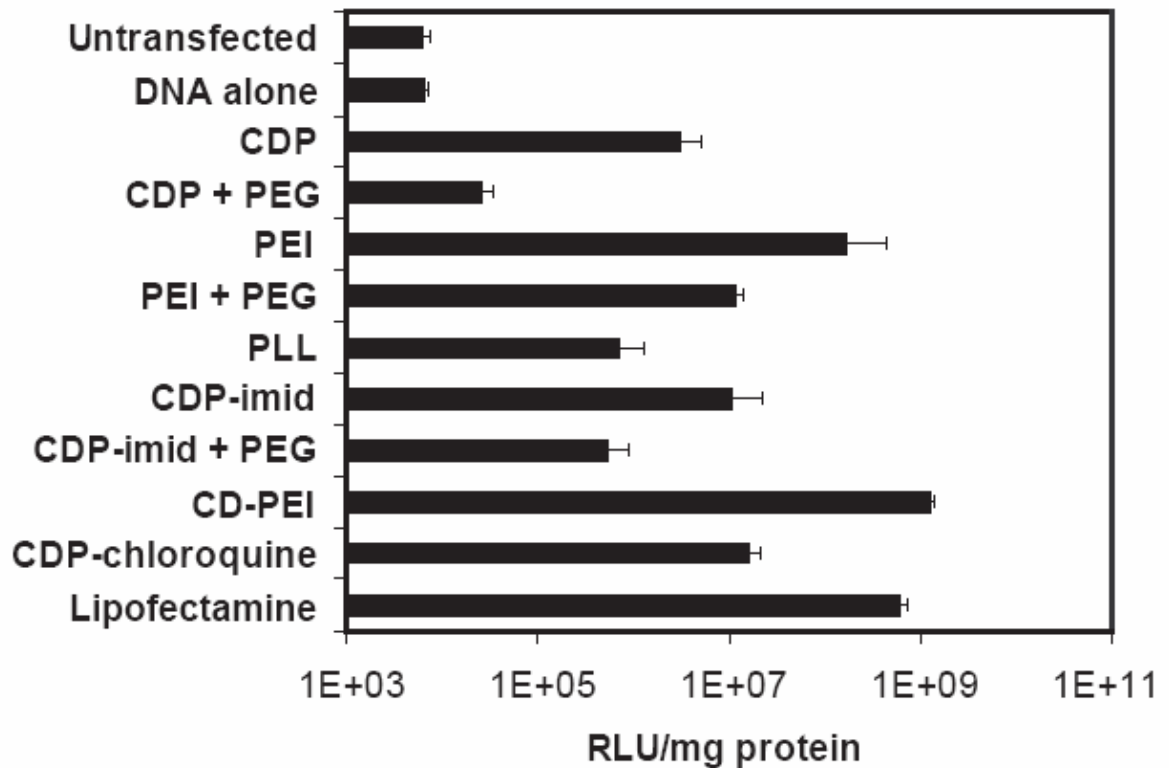


**Figure 4.7:** Gene delivery efficiency for each of the particles used in this study. The delivery vectors were complexed with plasmid DNA encoding luciferase and used to transfect HeLa cells. The relative luciferase expression varies markedly for each type of particle. In general, stabilizing particles through PEGylation resulted in lower luciferase expression.

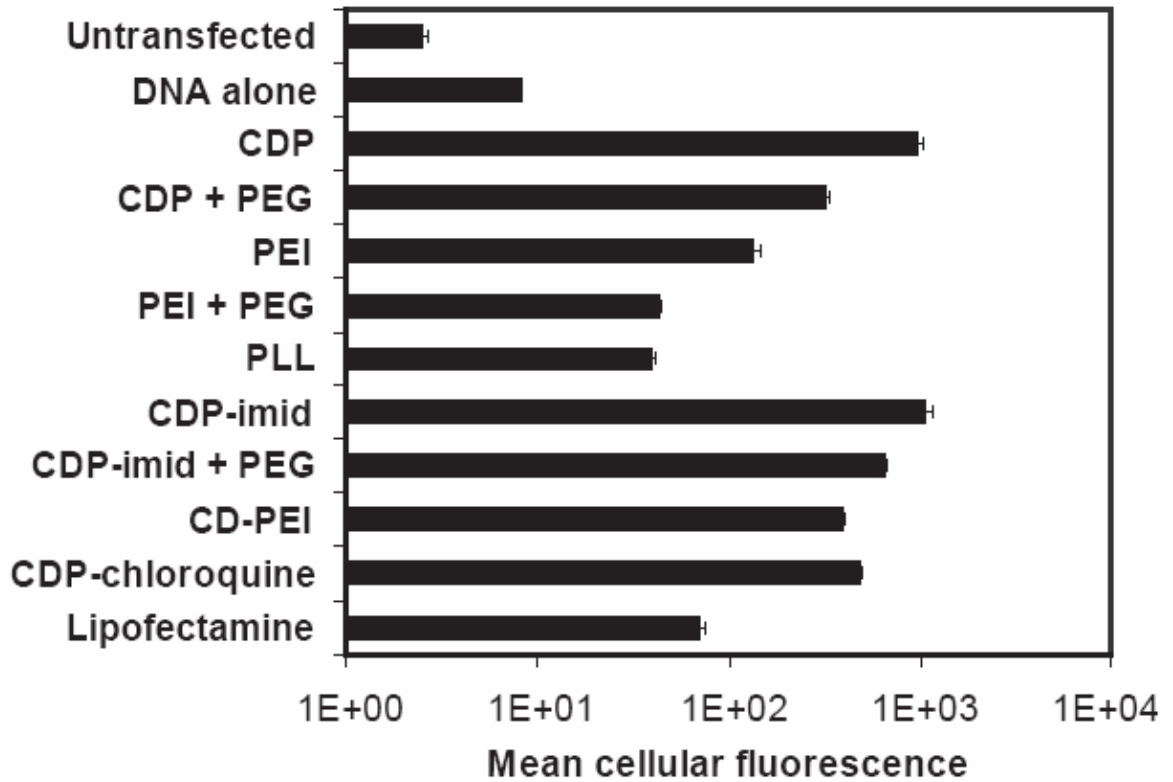


**Figure 4.8:** Measure of DNA uptake for each type of particle. Fluorescently labeled plasmid DNA was complexed with each type of delivery vector and administered to HeLa cells. After four hours, the cells were collected and analyzed by flow cytometry. The mean cellular fluorescence was used as a measure of DNA uptake.

## 4.6 References

1. Davis, M.E., *Non-viral gene delivery systems*. Curr Opin Biotechnol, 2002. **13**(2): p. 128-31.
2. Godbey, W.T. and A.G. Mikos, *Recent progress in gene delivery using non-viral transfer complexes*. J Control Release, 2001. **72**(1-3): p. 115-25.
3. Boussif, O., F. Lezoualc'h, M.A. Zanta, M.D. Mergny, D. Scherman, B. Demeneix, and J.P. Behr, *A versatile vector for gene and oligonucleotide transfer into cells in culture and in vivo: polyethylenimine*. Proc Natl Acad Sci U S A, 1995. **92**(16): p. 7297-301.
4. Luo, D. and W.M. Saltzman, *Synthetic DNA delivery systems*. Nat Biotechnol, 2000. **18**(1): p. 33-7.
5. Stayton, P.S., A.S. Hoffman, N. Murthy, C. Lackey, C. Cheung, P. Tan, L.A. Klumb, A. Chilkoti, F.S. Wilbur, and O.W. Press, *Molecular engineering of proteins and polymers for targeting and intracellular delivery of therapeutics*. J Control Release, 2000. **65**(1-2): p. 203-20.
6. Godbey, W.T., K.K. Wu, and A.G. Mikos, *Tracking the intracellular path of poly(ethylenimine)/DNA complexes for gene delivery*. Proc Natl Acad Sci U S A, 1999. **96**(9): p. 5177-81.
7. Bieber, T., W. Meissner, S. Kostin, A. Niemann, and H.P. Elsasser, *Intracellular route and transcriptional competence of polyethylenimine-DNA complexes*. J Control Release, 2002. **82**(2-3): p. 441-54.
8. Remy-Kristensen, A., J.P. Clamme, C. Vuilleumier, J.G. Kuhry, and Y. Mely, *Role of endocytosis in the transfection of L929 fibroblasts by polyethylenimine/DNA complexes*. Biochim Biophys Acta, 2001. **1514**(1): p. 21-32.
9. Hwang, S.J. and M.E. Davis, *Cationic polymers for gene delivery: designs for overcoming barriers to systemic administration*. Curr Opin Mol Ther, 2001. **3**(2): p. 183-91.
10. Forrest, M.L. and D.W. Pack, *On the kinetics of polyplex endocytic trafficking: implications for gene delivery vector design*. Mol Ther, 2002. **6**(1): p. 57-66.
11. Sonawane, N.D., F.C. Szoka, Jr., and A.S. Verkman, *Chloride accumulation and swelling in endosomes enhances DNA transfer by polyamine-DNA polyplexes*. J Biol Chem, 2003. **278**(45): p. 44826-31.

12. Akinc, A., D.M. Lynn, D.G. Anderson, and R. Langer, *Parallel synthesis and biophysical characterization of a degradable polymer library for gene delivery*. J Am Chem Soc, 2003. **125**(18): p. 5316-23.
13. Funhoff, A.M., C.F. van Nostrum, G.A. Koning, N.M. Schuurmans-Nieuwenbroek, D.J. Crommelin, and W.E. Hennink, *Endosomal escape of polymeric gene delivery complexes is not always enhanced by polymers buffering at low pH*. Biomacromolecules, 2004. **5**(1): p. 32-9.
14. Choi, J.S., J.A. MacKay, and F.C. Szoka, Jr., *Low-pH-sensitive PEG-stabilized plasmid-lipid nanoparticles: preparation and characterization*. Bioconjug Chem, 2003. **14**(2): p. 420-9.
15. Behr, J.P., *The proton sponge: A trick to enter cells the viruses did not exploit*. Chimia, 1997. **51**: p. 34-36.
16. Gonzalez, H., S.J. Hwang, and M.E. Davis, *New class of polymers for the delivery of macromolecular therapeutics*. Bioconjug Chem, 1999. **10**(6): p. 1068-74.
17. Akinc, A. and R. Langer, *Measuring the pH environment of DNA delivered using nonviral vectors: implications for lysosomal trafficking*. Biotechnol Bioeng, 2002. **78**(5): p. 503-8.
18. Chen, Q.R., L. Zhang, P.W. Luther, and A.J. Mixson, *Optimal transfection with the HK polymer depends on its degree of branching and the pH of endocytic vesicles*. Nucleic Acids Res, 2002. **30**(6): p. 1338-45.
19. Mishra, S., P. Webster, and M.E. Davis, *PEGylation significantly affects cellular uptake and intracellular trafficking of non-viral gene delivery particles*. Eur J Cell Biol, 2004. **83**(3): p. 97-111.
20. Sonawane, N.D., J.R. Thiagarajah, and A.S. Verkman, *Chloride concentration in endosomes measured using a ratioable fluorescent Cl<sup>-</sup> indicator: evidence for chloride accumulation during acidification*. J Biol Chem, 2002. **277**(7): p. 5506-13.
21. Pun, S.H., N.C. Bellocq, A. Liu, G. Jensen, T. Machermer, E. Quijano, T. Schlupe, S. Wen, H. Engler, J. Heidel, and M.E. Davis, *Cyclodextrin-modified polyethylenimine polymers for gene delivery*. Bioconjug Chem, 2004. **15**(4): p. 831-40.
22. Forrest, M.L., G.E. Meister, J.T. Koerber, and D.W. Pack, *Partial acetylation of polyethylenimine enhances in vitro gene delivery*. Pharm Res, 2004. **21**(2): p. 365-71.

23. Dubruel, P., B. Christiaens, M. Rosseneu, J. Vandekerckhove, J. Grooten, V. Goossens, and E. Schacht, *Buffering properties of cationic polymethacrylates are not the only key to successful gene delivery*. *Biomacromolecules*, 2004. **5**(2): p. 379-88.
24. Erbacher, P., A.C. Roche, M. Monsigny, and P. Midoux, *Putative role of chloroquine in gene transfer into a human hepatoma cell line by DNA/lactosylated polylysine complexes*. *Exp Cell Res*, 1996. **225**(1): p. 186-94.
25. Allison, J.L., R.L. O'Brien, and F.E. Hahn, *DNA: reaction with chloroquine*. *Science*, 1965. **149**(688): p. 1111-3.
26. Maxfield, F.R., *Weak bases and ionophores rapidly and reversibly raise the pH of endocytic vesicles in cultured mouse fibroblasts*. *J Cell Biol*, 1982. **95**(2 Pt 1): p. 676-81.
27. Lecocq, M., S. Wattiaux-De Coninck, N. Laurent, R. Wattiaux, and M. Jadot, *Uptake and intracellular fate of polyethylenimine in vivo*. *Biochem Biophys Res Commun*, 2000. **278**(2): p. 414-8.
28. Kichler, A., C. Leborgne, E. Coeytaux, and O. Danos, *Polyethylenimine-mediated gene delivery: a mechanistic study*. *J Gene Med*, 2001. **3**(2): p. 135-44.
29. Singh, R.S., C. Goncalves, P. Sandrin, C. Pichon, P. Midoux, and A. Chaudhuri, *On the gene delivery efficacies of pH-sensitive cationic lipids via endosomal protonation: a chemical biology investigation*. *Chem Biol*, 2004. **11**(5): p. 713-23.
30. Walker, G.F., C. Fella, J. Pelisek, J. Fahrmeir, S. Boeckle, M. Ogris, and E. Wagner, *Toward Synthetic Viruses: Endosomal pH-Triggered Deshielding of Targeted Polyplexes Greatly Enhances Gene Transfer in vitro and in vivo*. *Mol Ther*, 2005. **11**(3): p. 418-25.
31. Kulkarni, R.P., D. D. Wu, et al., *Quantitating intracellular transport of polyplexes by spatio-temporal image correlation spectroscopy*. In press, 2005.
32. Suh, J., D. Wirtz, and J. Hanes, *Efficient active transport of gene nanocarriers to the cell nucleus*. *Proc Natl Acad Sci U S A*, 2003. **100**(7): p. 3878-82.
33. Davis, M.E., S.H. Pun, N.C. Bellocq, T.M. Reineke, S.R. Popielarski, S. Mishra, and J.D. Heidel, *Self-assembling nucleic acid delivery vehicles via linear, water-soluble, cyclodextrin-containing polymers*. *Curr Med Chem*, 2004. **11**(2): p. 179-97.
34. Popielarski, S.R., S. Mishra, and M.E. Davis, *Structural effects of carbohydrate-containing polycations on gene delivery. 3. Cyclodextrin type and functionalization*. *Bioconjug Chem*, 2003. **14**(3): p. 672-8.

## **Chapter 5: Assessing *in vivo* differences in protein mobility between pioneer versus follower growth cones with multi-photon fluorescence recovery after photobleaching (FRAP)**

### **5.1 Abstract**

Navigating growth cones need to integrate, process, and respond to guidance signals, requiring dynamic information transfer within and between different compartments. Studies have shown that faced with different navigation challenges, growth cones display dynamic changes in growth kinetics and morphologies. However, it remains unknown if these are paralleled by differences in their internal molecular dynamics. To examine if there are protein mobility differences during guidance, we developed multi-photon fluorescence recovery after photobleaching (FRAP) methods to determine molecular diffusion rates in pathfinding growth cones *in vivo*. Actively navigating growth cones (leaders) have consistently longer recovery times compared to ones that are fasciculated and less actively navigating (followers). Pharmacological perturbations of the cytoskeleton point to actin as the primary modulator of diffusion in differently behaving growth cones. This approach provides a powerful means to quantify mobility of specific proteins in neurons *in vivo* and reveals that diffusion is important during axon navigation.

## 5.2 Introduction

Developing vertebrate brains are comprised of a small number of neuronal cell clusters and the axons connecting them [1-3]. Wiring this initial network of nerve cells involves guided extension of axons led by their navigating tips, called growth cones, towards their final targets [4]. In many cases, leader growth cones (pioneers) trail-blaze the initial paths, actively sensing guidance cues as they grow, while following axons (followers) largely progress along the leaders' tracks, simplifying their navigation challenges to more constrained explorations of their local environments [5]. The different navigation schemes employed by pioneers and followers are reflected in the differences in their external morphologies and behavior [5-9]. However, we do not know whether similar differences might also exist inside the growth cones, reflected in differences in protein mobility. Neither the kinetics of local protein movement nor the effects of cytoskeletal elements on protein mobility have been probed in growth cones *in vivo*. Localized diffusion differences in growth cones may be critical for delivery of molecular species into the growth cone tip, thus influencing the strength and extent of signaling cascades induced by activated guidance receptors and on cytoskeleton regulation associated with growth cone motility and guidance.

In the present study, we have developed a method for examining the dynamics of protein diffusion in developing neurons of live zebrafish embryos using one- and two-photon fluorescence recovery after photobleaching (FRAP) at selected time intervals during development. FRAP has been previously used to study the mobility, transport, and sub-cellular organization of fluorescently tagged molecular species in cultured cells [10-15], but rarely in a three dimensional embryo. In FRAP, a small region is bleached

using high intensity laser illumination; the recovery of fluorescence by diffusion of non-bleached fluorescent molecules into this area from the mobile fraction is then monitored using low-intensity illumination. Because recovery depends on the movement of unbleached fluorophores from the surrounding areas, we can calculate a diffusion constant,  $D$ , for those molecules [13, 16-18].

We have previously described the formation of the postoptic commissure (POC), a commissural axon tract connecting the ventro-rostral clusters of neurons across the midline in the zebrafish forebrain [5] (Figure 5.1a). A stable transgenic line of zebrafish using the *gata2::GFP* highlights the cluster of neurons that establish the POC [19]. These clusters make up an equivalence group of cells where the axon of one cell can substitute for another (followers can become leaders) [5]. Using timelapse imaging, followers can be observed while they grow along leaders and when they detach from them and grow on their own, allowing us to test for any differences in growth cones that might exist during these different navigation modes. Here, we combine FRAP measurements with timelapse analysis to explore the relationship between protein mobility and growth cone guidance by measuring the dynamics of cytoplasmic diffusion in early neurons and their growth cones. The results allow us to correlate regional diffusion measurements with growth cone behavior as POC axons establish the early commissural tract in a living embryo and test for linkage between the two. This approach can be used to quantitate other intracellular dynamics within the developing vertebrate embryo, thus providing a powerful tool for analyzing functional relationships between cellular behaviors and protein dynamics.

## 5.3 Results

### One- and Two-Photon FRAP in Small Cellular Compartments *in vivo*

As a reporter of intracellular protein mobility, we used the *gata2::GFP* transgenic line and measured the diffusion rates of GFP in different regions of young neurons (Figure 5.1a) with both one and two-photon FRAP microscopy. The high level of GFP expression allows the behavior of early POC axons and their growth cones to be observed *in vivo* as they navigate across the midline and interact with their surroundings and each other [5] (Figure 5.1a). We first examined the diffusion of cytosolic *gata2::GFP* expressing *vrc* neurons at 22-24 hours post fertilization (hpf) GFP in three main neuronal compartments: the cell body, the axon process, and the growth cone (Figure 5.1a, n=60 separate embryos). We analyzed lateral diffusion rates based on fluorescence recovery traces obtained from two-dimensional scans over time (Figure 5.1b, also see Figure 5.2). Due to the large nucleus, the cytoplasmic volume in early neurons is small, effectively reducing the cytoplasm to two-dimensions and thus allowing direct comparison of diffusion among the three compartments.

The FRAP measurements require that active structures such as growth cones remain in the same axial plane (z-dimension) to ensure that the signal does not result because of sample movement out of the focal plane. To assess the axial mobility of growth cones, we used depth-coded z-stacks of the same growth cone at different time-points. Four-dimensional (x, y, z and time) timelapse movies of early POC growth cones showed that early growth cones remain in the same axial plane for up to 2 minutes, which is sufficient time for FRAP measurements (Figure 5.1c). During this time, POC growth cones actively sample their environment as revealed by the appearance and disappearance

of individual filopodia (Figure 5.1c, arrows). Post-bleach traces in the three compartments (cell body, axon process, growth cone) showed rapid recovery, occurring on the order of seconds (Figure 5.3a-c), with diffusion being fastest in the cell body and slowest in the growth cone (Table 5.1). Control experiments using fixed *gata2::GFP* embryos showed no recovery as expected (data not shown). To verify that the observed diffusion was not affected by GFP expression levels or was specific to the vrc cells, we performed similar FRAP measurements using the *islet1::GFP* transgenic line [20] (which has lower GFP expression at this stage compared to the *gata2::GFP* fish) as well as neurons that belong to the dorso-rostral cluster in slightly older *gata2::GFP* embryos (27 hpf) and obtained similar diffusion values in all samples<sup>1</sup>.

To confirm that the observed GFP diffusion kinetics could be replicated by another similar-sized molecule, we examined the kinetics of YFP. To do this, we used *gata2::GFP* embryos injected with YFP mRNA and compared the GFP/YFP diffusion values; in these embryos YFP is expressed at a significantly lower level than GFP. For this experiment we utilized two-photon FRAP, allowing us to examine GFP/YFP recovery kinetics simultaneously<sup>2</sup>. We obtained virtually identical fluorescence recovery traces (Figure 5.3d) and diffusion values for both fluorescent species ( $0.92 \pm 0.16 \mu\text{m}^2/\text{sec}$  [GFP] and  $0.94 \pm 0.17 \mu\text{m}^2/\text{sec}$  [YFP],  $n=15$ ). The mobile fractions for GFP and YFP were similar, suggesting that both species are able to travel with the same degree of freedom inside the cell and thus are good reporters of diffusion in early neurons for other proteins of similar sizes. As the diffusion values for GFP and YFP obtained using two-photon

---

<sup>1</sup>Diffusion values were  $D=0.94 \pm 0.07 \mu\text{m}^2/\text{sec}$  in *islet1::GFP* positive neurons and  $D=0.96 \pm 0.15 \mu\text{m}^2/\text{sec}$  in neurons of the dorso-rostral cluster in the *gata2::GFP* line.

<sup>2</sup> This is due to the two-photon absorption cross sections of many common fluorophores (including the fluorescent proteins) being broad over the wavelength range of typical two-photon lasers (~750-950 nm).

FRAP are similar to the one-photon results obtained earlier (Table 5.1), we concluded that, for this experiment, out of focus light did not significantly perturb diffusion measurements. Two-photon illumination permits deeper penetration into the sample and reduced radiation outside of the focal plane of the laser beam, significantly reducing bleaching in the axial direction. Thus two-photon FRAP might be the method of choice for studying protein mobility in older or deeper tissues.

### **Leaders Have Slower Diffusion Kinetics than Followers**

To determine whether differences between leader and follower growth cones are reflected in cytoplasmic diffusion rates, we compared GFP diffusion in the two growth cone types. Leader growth cones consistently showed longer recovery times while follower growth cones had rapid recoveries. The typical recovery time of the leader growth cone was 6-8 s compared to 3-4 s for a follower growth cone. Thus, GFP diffusion was significantly slower in leader growth cones ( $0.28 \mu\text{m}^2\text{s}^{-1}$ , Table 5.1) compared to follower growth cones ( $0.55 \mu\text{m}^2\text{s}^{-1}$ , Table 5.1); both values were unchanged irrespective of growth cone position along the commissural tract.

The clear difference in diffusion kinetics between leaders and followers led us to ask if diffusion rate was dependent on axon fasciculation as this result suggested. To test this directly, we next examined off-tract follower growth cones, those that occasionally detach from other POC axons and begin to grow on their own. Once detached, such growth cones must pathfind as leaders or rejoin other axons in order to cross the midline. FRAP measurements revealed a striking decrease in GFP mobility in off-tract growth cones compared to regular follower growth cones. Off-tract growth cones had the slowest

recovery times, with an average diffusion of  $0.15 \mu\text{m}^2\text{s}^{-1}$  (Figure 5.4a, Table 5.1). This slow recovery time is consistent with the notion that the need to pathfind independently is reflected through cytoplasmic diffusion rates.

To confirm that differences in diffusion rate in growth cones were dynamically linked to the degree of growth cone interaction with its local environment versus with axon-axon interactions, we assayed the same follower growth cone as it grew away from or along other axons using timelapse analysis and FRAP (Figure 5.4b). Fluorescence recovery was slow at all points when the follower growth cone lost contact with other axons and therefore was responsive only to environmental cues (Figure 5.4b, pink lines). Both before losing contact and after reestablishing contact, recovery was rapid and the diffusion constant was similar to regular follower growth cones (that is those that grow along the leader axon) (Figure 5.4b, blue lines). These experiments indicate a strong correlation between GFP diffusion and axon interactions during pathfinding. Growth cones seen in axons that independently probe their environments have significantly slower diffusion values compared to growth cones that wrap around other axons.

### **Differences between Leaders and Followers Depend on the Actin Cytoskeleton**

The observed differences in GFP mobility suggest the presence of a diffusion restriction that is either more extensive or longer lasting in those growth cones displaying slower rates. Previous measurements have shown that the actin network can slow diffusion of dextrans in cultured neurons [21]. The leading edge of the growth cone contains a meshwork of actin bundles that project radially into the filopodia [22]. Cytochalasins are well characterized actin depolymerizing agents [23, 24] used to study

the effects of the actin on diffusion in *Dictyostelium* and cultured neurons [25, 26]. To examine whether the actin network affects diffusion in the growth cone, we assayed the resulting recovery after cytochalasin B treatment. Growth cones in embryos injected with cytochalasin B began to lose filopodia and became less motile compared to uninjected embryos. Cytochalasin B significantly increased the diffusion rate in both leader and off-tract growth cones, resulting in all growth cones having similar recovery kinetics (Figure 5.3c, Table 5.1). Similar results were obtained with latrunculin A, another actin depolymerizing agent (data not shown).

To further elucidate the role of actin, we examined the diffusion and recovery kinetics of YFP-actin in leader versus follower growth cones. The YFP-actin exists in both a filamentous, polymerized form and a freely diffusible globular form. As expected, we see a slight reduction in diffusion between GFP versus YFP-actin because the polymerized actin cannot rapidly recover when bleached. YFP-actin diffusion values were about ten percent slower than for pure GFP, mostly reflecting the presence of polymerized actin that is slower to turn over. However, the major difference between leaders and followers can be seen in the mobile fraction (R) of YFP-actin (Table 5.2). For followers, we found R to be  $49 \pm 13$  %, while it was  $61 \pm 11$  % in leaders. The increase in recovery fraction between the two indicates that there is greater turnover of YFP-actin in leaders versus followers, even though the time scale of recovery is slower. This indicates that leader growth cones experience greater polymerization and depolymerization of YFP-actin as compared to followers; the increased turnover results in a greater quantity of YFP-actin that is free to diffuse and recover fluorescence after the bleach. These results, along with the observed increase in GFP mobility upon actin

depolymerization in leaders, strongly suggest that actin plays a role in modulating local diffusion in growth cones *in vivo*.

The microtubule scaffold is the other important cytoskeletal network in the central region of the growth cone and axon process and is employed for organelle transport and structural integrity [27]. To determine how this network affects diffusion in growth cones, we treated the embryos with nocodazole, a drug that depolymerizes microtubules and is effective for microtubule destabilization in zebrafish [28]. Nocodazole treatment caused progressive growth cone collapse. However, fluorescence recovery traces did not reveal a significant effect on either recovery times or diffusion values, although small decreases did occur (Figure 5.4d, Table 5.1), suggesting that the microtubule network does not play a direct role in modulating local diffusion rates in growth cones *in vivo*. The nocodazole result is insightful, however, as it provides direct evidence that diffusion rate in the growth cone is not directly linked to growth cone shape *in vivo*, which until this experiment was a distinct possibility.

## **5.4 Discussion**

### **Quantitative One- and Two-Photon FRAP Measurements *in vivo***

The results described above clearly demonstrate the power and promise of one- and two-photon FRAP combined with timelapse imaging for measuring diffusion and transport kinetics of molecules and complexes within developing neurons *in vivo*. These methods allow for both qualitative and quantitative analysis of macromolecular transport parameters that can in turn be directly linked to cellular behaviors. Specifically, here we demonstrate this by measuring GFP diffusion kinetics in young neurons and show that

these kinetics are not only different between the main neuronal compartments (cell body, axon, and growth cone) but also that they differ depending on the level of active pathfinding. Both one- and two-photon FRAP can be used for sensitive measurements of protein diffusion in small compartments, up to the diffraction limited laser spot size. Furthermore, the laser pulses do not significantly physically damage the embryos, as the examined cells continue to grow normally. Indeed, the same cell can be repeatedly examined by FRAP with no observable behavioral defects.

The benefits of two-photon FRAP include the ability to penetrate deeper into tissues (up to  $\sim 500 \mu\text{m}$ ), reduced radiation outside of the focal plane of the beam, and the broad spectral absorption of many common fluorophores. Because of this broad excitation maxima, there are many potential wavelengths that can be used to excite a given dye molecule, which can allow for photobleaching of multiple species simultaneously, if desired, as demonstrated here with the GFP/YFP bleach experiments. An optimal excitation wavelength can thus be identified which allows for maximal fluorophore excitation while avoiding two photon damage of sensitive intracellular structures (such as pigment granules). This study establishes the feasibility of multi-photon FRAP within the living embryo and will allow for quantitation of additional developmental events. The broad applicability of this technique towards many different cell types and fluorophores of choice marks a significant step in the ability to probe the dynamics of biological systems *in vivo*.

### **Protein Dynamics in Growth Cones**

Our results demonstrate significant differences in internal diffusion dynamics of *in vivo* growth cones when they face different navigation challenges. Cytoplasmic diffusion rates are slower when growth cones are actively navigating, whether they are true leaders or off-tract followers. Specifically, the observed differences in GFP mobility suggest the presence of transient diffusion restrictions within the neuronal cytoplasm; perturbation of the actin and tubulin networks point to actin as the primary modulator of the diffusion differences. Depolymerization of actin abolished differences in GFP mobility among the different growth cone types, while depolymerization of tubulin did not. The leading edge of the growth cone is actin-rich; as the growth cone navigates through its environment, there is significant turnover of this actin.

The organization and rearrangement of the cytoskeleton have long been known to play critical roles in growth cone motility and navigation. Cytoskeletal processes underlie the constant flux within the growth cone, including surface presentation of guidance receptors and new protein synthesis/delivery [29]. In the simplest scenario, this suggests that in addition to external differences in morphology between leader and follower growth cones, the intracellular cytoskeletal structures might also be different. The finding that off-tract followers resemble leaders in their diffusion characteristics suggests a dynamic link between the actin network and guidance signaling that can alter internal growth cone structure and diffusion rates.

Recently, specific guidance cues have been shown to directly affect the actin and microtubule cytoskeletons [30]. An interesting possibility is that in addition to its role in mobility, the actin network in growth cones sets up transient boundaries that effectively

limit diffusion on time scales which temporally affect delivery and local concentrations of molecules critical for growth or signal response. The actin network creates a mesh with a given pore size; changing the pore size of the actin cytoskeleton may be important for mobility and dynamic organization of the neuron. Such control of the actin network could serve as a mechanism for amplifying local guidance signals, helping growth cones navigate, and ultimately controlling nervous system wiring and development.

In the present stage of developmental neurobiology, we are increasingly more interested not only in the function of proteins but also their mobilities and understanding how these processes are interrelated. Until now, however, such studies have been largely restricted to *in vitro* systems. The approach shown here is an exciting step forward in our ability to directly observe and measure protein movement in cells of living embryos.

## 5.5 Methods

### *Fish maintenance*

Raising and spawning of adult zebrafish were performed as outlined in the Zebrafish Book [31] and in accordance with the animal care guidelines of the California Institute of Technology.

### *Embryo Preparation and Pharmacological Treatments*

Embryos at 20-22 hours post fertilization (hpf) were anesthetized with tricaine in sedative amounts (0.01%) and embedded in a drop of 1-1.2% ultralow melt agarose on a cover slip-bottom petri dish in 30% danieau/0.01% tricane/0.15 mM Phenylthiourea (PTU). Pharmacological inhibitors of cytoskeleton components were injected into the neural tube of zebrafish embryos between 18-24 (hpf) and embryos were allowed to recover for 10-20 min at 28°C. Nocodazole (Sigma) was used at a concentration of 20-40  $\mu$ M, and cytochalasin B (Sigma) was used at 4  $\mu$ g/mL. Embryos were subsequently remounted in an inverted position to allow imaging of commissural axons. Injected embryos were imaged for a maximum of 30 min.

### *Imaging details*

All imaging was performed using an Inverted 510 META Zeiss Confocal Scanning Microscope with a Plan-Neofluar 40X/1.3 NA objective. Temperature was maintained at 28-29°C throughout the imaging experiment. GFP positive cells were excited with a 30mW Argon laser using the 488 nm excitation line with a 505LP Chroma filter and a pinhole setting of 1.2-1.5 Airy units.

*FRAP measurements and analysis*

100 images (512 x 512) were acquired in a continuous timelapse mode at the maximal scanning rate. Five images were acquired before the bleach to obtain a fluorescence baseline. For all *in vivo* photobleaching experiments, a circular region, 1 $\mu$ m in radius, was defined and photobleached at full laser power (100% transmission, 5-7 pulses). Fluorescence recovery was monitored by scanning the whole field of interest at low laser power (1-2% transmission) and the fluorescence intensity recovery traces recorded. Typically less than 3% of total fluorescence was lost during the entire recovery phase. The bleaching characteristics of the laser beam were determined by bleaching a spot in an immobile specimen of fluorescein using the same laser and objective settings. From this data, the beam profile and  $1/e^2$  beam radius were determined.

Diffusion coefficients for GFP were determined by classical FRAP analysis as previously described [16, 17, 32]. The fluorescence recovers according to the following equation:

$$\frac{F(t)}{F_p} = \sum_{n=0}^{\infty} \left[ \left( \frac{(-K)^n}{n!} \right) \left( \frac{1}{1 + n(1 + 2t/\tau_D)} \right) \right], \quad (1)$$

where  $F(t)$  is the fluorescence intensity at time  $t$  after the bleach pulse,  $F_p$  is the fluorescence intensity immediately prior to bleach,  $\tau_d$  is the characteristic diffusion time, and  $K$  is a parameter related to the degree of bleaching:

$$\frac{F_o}{F_p} = \frac{(1 - e^{-K})}{K}, \quad (2)$$

where  $F_o$  is the fluorescence intensity immediately after the bleach. The  $K$  parameter was determined for each trace. The FRAP recovery curves were then used to determine the

half time of recovery ( $\tau_{1/2}$ ).  $\tau_{1/2}$  is related to the characteristic diffusion time  $\tau_d$  by the following relation:

$$\tau_{1/2} = \gamma\tau_d, \quad (3)$$

where  $\gamma$  is a function of the beam shape and the extent of bleaching. Typically, for diffusive processes, when  $K < 1.5$ ,  $\gamma = 1.1$ . The diffusion constant can then be found from the following relation:

$$D = w^2/4\tau_d, \quad (4)$$

where  $w$  is the  $1/e^2$  beam radius as determined previously.

Diffusion coefficients for GFP were categorized by the structure of the neuron measured (cell body, process, leader growth cone, or follower growth cone).

#### *Two-photon FRAP measurements and analysis*

Diffusion coefficients for GFP and YFP were determined by two-photon FRAP analysis, as previously described [33]. Two-photon FRAP measurements were performed using a Zeiss LSM 510 META confocal microscope with a Coherent Chameleon two-photon Ti:Sapphire laser. Both GFP and YFP were simultaneously bleached using 900-nm light with a 40X/1.3 NA Apochromat objective. Cell body compartment was chosen based on the YFP expression being strongest in this region, allowing both proteins to be excited. The bleaching characteristics of the laser beam were determined by bleaching a spot in an immobile specimen of fluorescein using the same laser and objective settings as for the two-photon in vivo imaging. From this data, the  $1/e^2$  axial ( $w_z$ ) and radial ( $w_r$ ) beam dimensions were determined.

For all in vivo two-photon photobleaching experiments, a circular region, 1.4  $\mu\text{m}$  in radius, was defined and photobleached at full laser power (100% power, 100% transmission, 7-9 pulses), and fluorescence recovery was monitored by scanning the whole field of interest at low laser power after the bleach (100% power, 10% transmission). In these FRAP experiments, typically less than 5% of total fluorescence was lost during the entire recovery phase. The fluorescence intensity recovery traces were recorded; the fluorescence recovers according to the following equation:

$$\frac{F(t)}{F_p} = \sum_{n=0}^{\infty} \left[ \left( \frac{2^{3/2} (-\beta)^n}{n!} \right) \left( \frac{1}{2 + 2n(1 + 2t/\tau_D)} \right) \left( \frac{1}{(2 + 2n + (4nt/R\tau_D))^{1/2}} \right) \right], \quad (5)$$

where  $F(t)$ ,  $F_p$ , and  $\tau_d$  are as before,  $R$  is the square of the ratio of the radial to axial beam dimensions ( $R \equiv w_z^2/w_r^2$ ), and  $\beta$  is a parameter related to the degree of bleaching:

$$\frac{F_o}{F_p} = \sum_{n=0}^{\infty} \frac{(-\beta)^n}{n!} \frac{1}{(1+n)^{3/2}}, \quad (6)$$

where  $F_o$  is the fluorescence intensity immediately after the bleach. The  $\beta$  parameter was determined for each trace. From fits of the collected data to these equations, the diffusion constant can then be found from the following relation (for two-photon FRAP):

$$D = w_r^2/8\tau_d, \quad (7)$$

where  $w_r$  is the  $1/e^2$  radial beam dimension as determined previously.

### *Data Analysis*

The  $D$  coefficients for each category were compared for significance using GraphPad InStat 3.0 Software. In cases where control diffusion rate was compared to

more than one perturbation, the p value was recalculated to adjust for multiple comparisons. Values of  $p < 0.001$  were considered significant.

### **Acknowledgements**

Magdalena Bak-Maier performed many of the initial zebrafish experiments, including the initial GFP diffusion data and the actin and cytochalasin perturbations. We thank David Koos and Helen McBride for helpful discussion and comments.

**Table 5.1: GFP Diffusion Rates in Different Neuronal Compartments and Growth Cones**

	Wild type			Cytochalasin B			Nocodazole		
	N	Diffusion ( $\mu\text{m}^2/\text{sec}$ )	S.D.	N	Diffusion ( $\mu\text{m}^2/\text{sec}$ )	S.D.	N	Diffusion ( $\mu\text{m}^2/\text{sec}$ )	S.D.
<b>Leader G.C.</b>	20	0.28 <sup>*</sup>	0.11	27	0.67 <sup>†</sup>	0.19	17	0.32	0.11
<b>Follower G.C.</b>	22	0.55 <sup>*</sup>	0.27	23	0.67	0.23	34	0.54	0.20
<b>Off-tract G.C.</b>	9	0.15 <sup>*</sup>	0.05	16	0.37 <sup>†</sup>	0.17	17	0.21	0.11
<b>Axon</b>	23	0.71 <sup>*</sup>	0.16	19	0.87 <sup>†</sup>	0.21	21	0.90 <sup>†</sup>	0.21
<b>Cell Body</b>	29	0.96 <sup>*</sup>	0.22	8	0.94	0.18	9	1.12	0.18

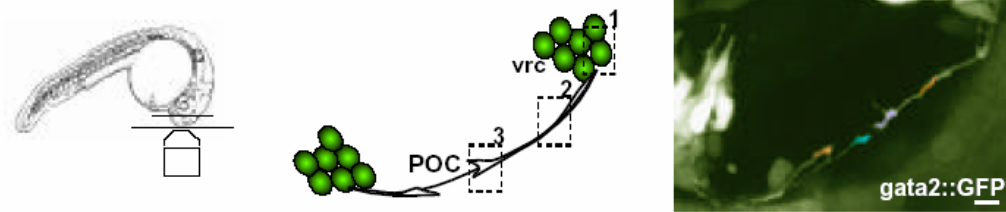
Diffusion coefficients for GFP in various compartments of the developing zebrafish neurons are listed above. For examining the effects of actin and microtubule networks, zebrafish were injected either with cytochalasin B or nocodazole, and the diffusion coefficients for GFP were measured by region. The p values were generated by comparing across wild type compartments for differences in diffusion ( $p < 0.001^*$ , ANOVA followed by Tukey-Kramer Multiple Comparison Test). The effect of cytochalasin B or nocodazole on diffusion for each compartment was compared with wild type using Student's T-test with  $p < 0.001$  noted<sup>†</sup>. G.C. = growth cone.

**Table 5.2: GFP and YFP-actin diffusion rates and recovery fractions in leader and follower neurons**

	<b>Leader g.c. (n=17)</b>	<b>Follower g.c (n=19)</b>
<b>GFP Diffusion (<math>\mu\text{m}^2/\text{s}</math>)</b> (p<.0001)	0.31 $\pm$ 0.17	0.60 $\pm$ 0.19
<b>GFP Mobile Fraction (%)</b> (p=.005)	64 $\pm$ 11	52 $\pm$ 13
<b>YFP-actin diffusion (<math>\mu\text{m}^2/\text{s}</math>)</b> (p<.0001)	0.28 $\pm$ 0.14	0.54 $\pm$ 0.17
<b>YFP-actin Mobile Fraction (%)</b> (p=.005)	61 $\pm$ 11	49 $\pm$ 13

Diffusion coefficients and mobile fractions for YFP-actin in leader and follower growth cones are listed above. The p values were generated by comparing measurements between leaders and followers using Student's t-test.

### a Image Acquisition



### b Quantitative FRAP Analysis

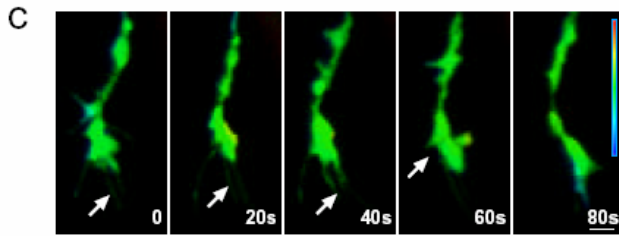
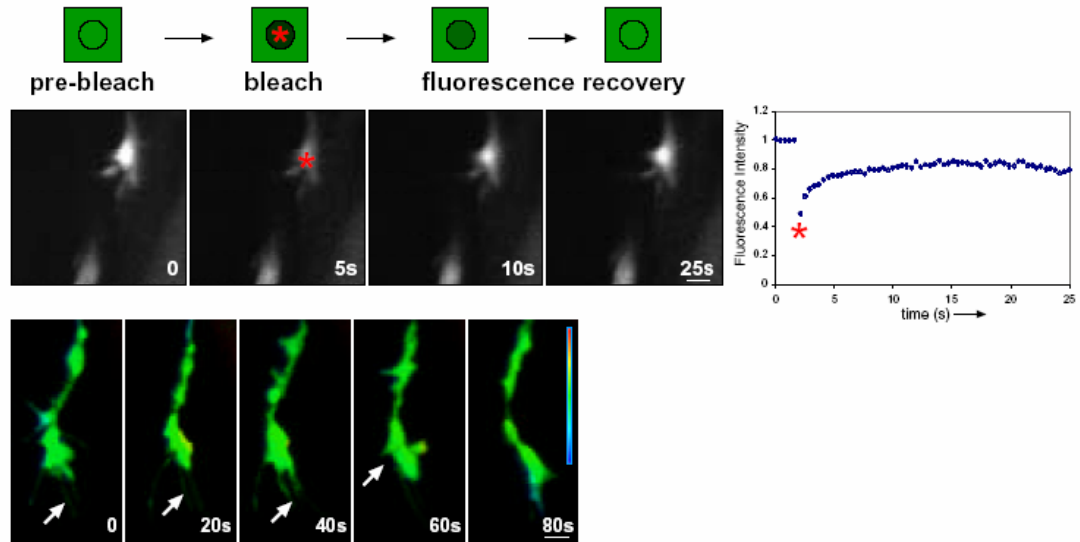


**Figure 5.1:** Single and two-photon FRAP analysis.

(a) (left) Schematic showing embryo preparation for imaging and FRAP analysis. (middle) Diagram of the postoptic commissure (POC) axon tract showing the three regions of the *gata2::GFP* neurons where FRAP measurements were taken: (1) cell body, (2) axon process and (3) growth cone. Ventro-rostral cluster (vrc). (right) 23hpf *gata2::GFP* embryo showing GFP positive vrc cells and early POC axons growing to midline. Individual POC growth cones have been highlighted by color. Black regions correspond to non-fluorescing cells.

(b) The image sequence represents a typical FRAP experiment performed on a leader growth cone. Pre-bleach sequences are acquired to provide baseline fluorescence, followed by the bleach (star). Fluorescence recovery is then recorded as a function of time and can be plotted as shown on the right. The mobile fraction can be calculated by finding the fluorescence intensity after the bleach divided by the initial fluorescence intensity (pre-bleach), normalized to the lowest intensity value right after the bleach.

(c) Depth coded z-stack of a leader growth cone showing no significant change in the axial position of the growth cone during the length of a typical FRAP experiment. Arrows indicate filopodia.

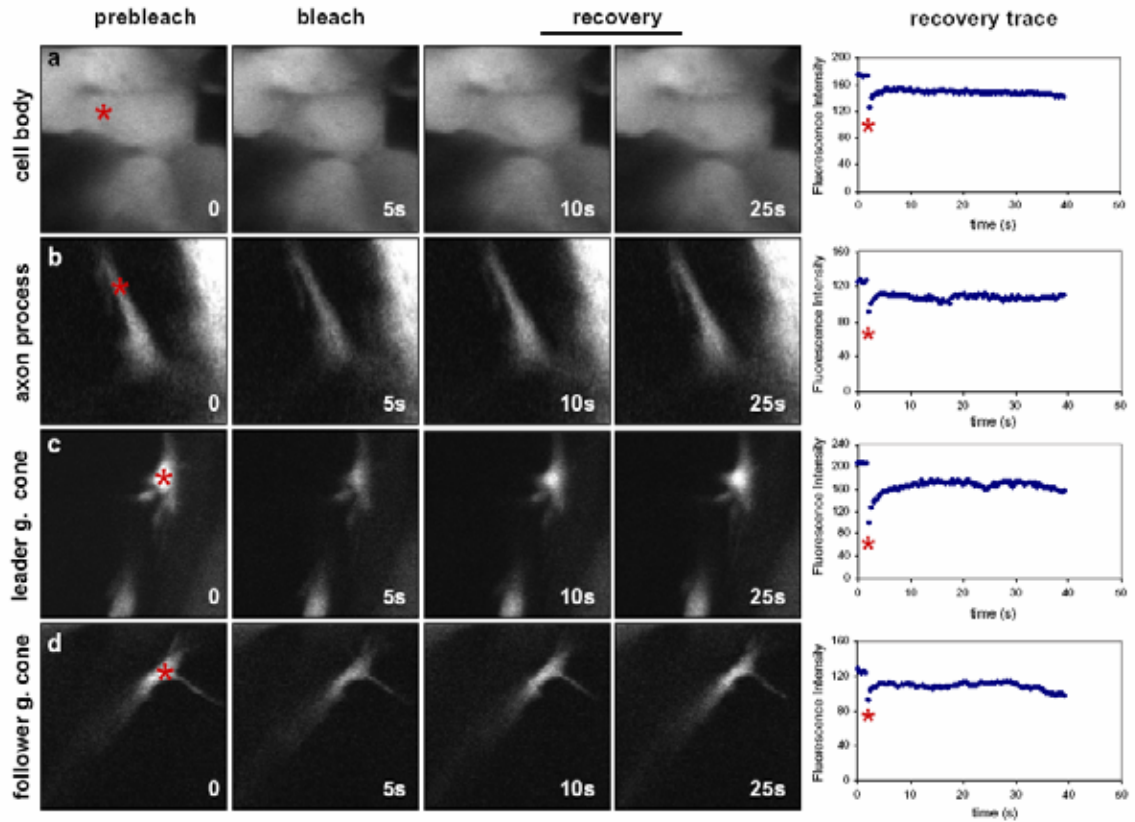


**Figure 5.2:** Further examples of typical FRAP experiments performed on different compartments of neurons (cell body, process, and two general types of growth cones: leader and follower). Leader growth cone is the same as in Figure 5.1.

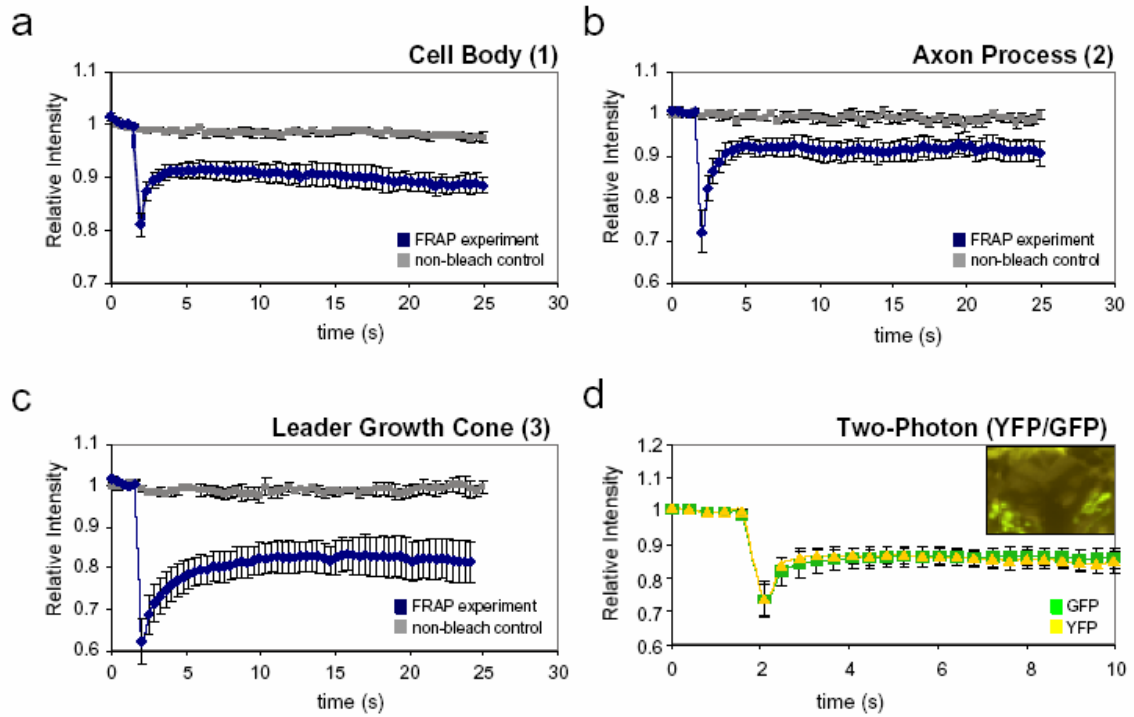


**Figure 5.3:** Average fluorescence recovery traces obtained with either single or two-photon FRAP imaging in different compartments of young neurons in vivo. (a) cell body, (b) axon process, (c) leader growth cone. The non-bleached control for each compartment is plotted in gray. (d) YFP/GFP cell-body two-photon comparison. The YFP average trace was normalized to the GFP. Scale bar = 10  $\mu\text{m}$ .

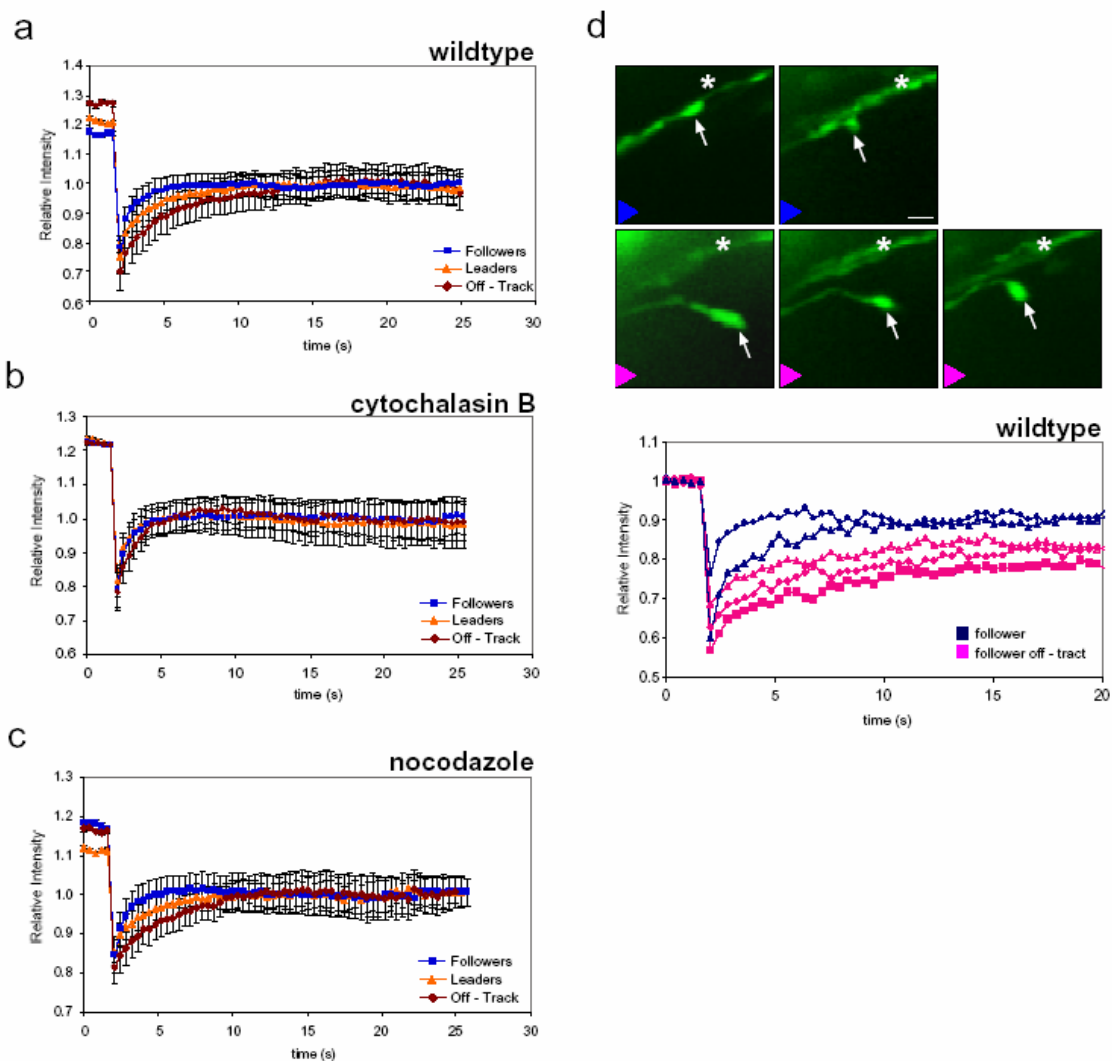


**Figure 5.4:** Measurement of diffusion in growth cones.

(a) Average fluorescence recovery traces in follower, leader, and follower off-track wild type growth cones. All traces have been normalized to the final recovery level post-bleach to illustrate the differences in diffusion kinetics.

(b-c) Effects of cytochalasin B (b) and nocodazole (c) on GFP diffusion in growth cones as assayed by FRAP analysis.

(d) Dynamic differences in GFP diffusion visualized in a single follower growth cone (arrow) as it either associates with other POC axons (star) or grows away from them. Fluorescence recovery traces corresponding to these events are plotted below. Blue traces correspond to growth cone in contact with the POC axons, pink traces when the growth cone traveled away from the POC.

## 5.6 References

1. Chitnis, A.B. and J.Y. Kuwada, *Axonogenesis in the brain of zebrafish embryos*. J Neurosci, 1990. **10**(6): p. 1892-905.
2. Mastick, G.S. and S.S. Easter, Jr., *Initial organization of neurons and tracts in the embryonic mouse fore- and midbrain*. Dev Biol, 1996. **173**(1): p. 79-94.
3. Wilson, S.W., L.S. Ross, T. Parrett, and S.S. Easter, Jr., *The development of a simple scaffold of axon tracts in the brain of the embryonic zebrafish, Brachydanio rerio*. Development, 1990. **108**(1): p. 121-45.
4. Tessier-Lavigne, M. and C.S. Goodman, *The molecular biology of axon guidance*. Science, 1996. **274**(5290): p. 1123-33.
5. Bak, M. and S.E. Fraser, *Axon fasciculation and differences in midline kinetics between pioneer and follower axons within commissural fascicles*. Development, 2003. **130**(20): p. 4999-5008.
6. Bovolenta, P. and J. Dodd, *Guidance of commissural growth cones at the floor plate in embryonic rat spinal cord*. Development, 1990. **109**(2): p. 435-47.
7. Bovolenta, P. and C. Mason, *Growth cone morphology varies with position in the developing mouse visual pathway from retina to first targets*. J Neurosci, 1987. **7**(5): p. 1447-60.
8. McConnell, S.K., A. Ghosh, and C.J. Shatz, *Subplate neurons pioneer the first axon pathway from the cerebral cortex*. Science, 1989. **245**(4921): p. 978-82.
9. Myers, P.Z. and M.J. Bastiani, *Growth cone dynamics during the migration of an identified commissural growth cone*. J Neurosci, 1993. **13**(1): p. 127-43.
10. Cheutin, T., A.J. McNairn, T. Jenuwein, D.M. Gilbert, P.B. Singh, and T. Misteli, *Maintenance of stable heterochromatin domains by dynamic HP1 binding*. Science, 2003. **299**(5607): p. 721-5.
11. Coscoy, S., F. Waharte, A. Gautreau, M. Martin, D. Louvard, P. Mangeat, M. Arpin, and F. Amblard, *Molecular analysis of microscopic ezrin dynamics by two-photon FRAP*. Proc Natl Acad Sci U S A, 2002. **99**(20): p. 12813-8.
12. Festenstein, R., S.N. Pagakis, K. Hiragami, D. Lyon, A. Verreault, B. Sekkali, and D. Kioussis, *Modulation of heterochromatin protein 1 dynamics in primary Mammalian cells*. Science, 2003. **299**(5607): p. 719-21.
13. Lippincott-Schwartz, J., E. Snapp, and A. Kenworthy, *Studying protein dynamics in living cells*. Nat Rev Mol Cell Biol, 2001. **2**(6): p. 444-56.

14. Nehls, S., E.L. Snapp, N.B. Cole, K.J. Zaal, A.K. Kenworthy, T.H. Roberts, J. Ellenberg, J.F. Presley, E. Siggia, and J. Lippincott-Schwartz, *Dynamics and retention of misfolded proteins in native ER membranes*. Nat Cell Biol, 2000. **2**(5): p. 288-95.
15. Phair, R.D. and T. Misteli, *High mobility of proteins in the mammalian cell nucleus*. Nature, 2000. **404**(6778): p. 604-9.
16. Axelrod, D., D.E. Koppel, J. Schlessinger, E. Elson, and W.W. Webb, *Mobility measurement by analysis of fluorescence photobleaching recovery kinetics*. Biophys J, 1976. **16**(9): p. 1055-69.
17. Klonis, N., M. Rug, I. Harper, M. Wickham, A. Cowman, and L. Tilley, *Fluorescence photobleaching analysis for the study of cellular dynamics*. Eur Biophys J, 2002. **31**(1): p. 36-51.
18. White, J. and E. Stelzer, *Photobleaching GFP reveals protein dynamics inside live cells*. Trends Cell Biol, 1999. **9**(2): p. 61-5.
19. Meng, A., H. Tang, B.A. Ong, M.J. Farrell, and S. Lin, *Promoter analysis in living zebrafish embryos identifies a cis-acting motif required for neuronal expression of GATA-2*. Proc Natl Acad Sci U S A, 1997. **94**(12): p. 6267-72.
20. Higashijima, S., Y. Hotta, and H. Okamoto, *Visualization of cranial motor neurons in live transgenic zebrafish expressing green fluorescent protein under the control of the islet-1 promoter/enhancer*. J Neurosci, 2000. **20**(1): p. 206-18.
21. Popov, S. and M. Poo, *Diffusional transport of macromolecules in developing nerve processes*. The Journal of Neuroscience, 1992. **12**: p. 77-85.
22. Dent, E.W. and F. Gertler, *Cytoskeletal dynamics and transport in growth cone motility and axon guidance*. Neuron, 2003. **40**: p. 209-227.
23. Flanagan, M.D. and S. Lin, *Cytochalasins block actin filament elongation by binding to high affinity sites associated with F-actin*. Journal of Biological Chemistry, 1980. **255**: p. 835-838.
24. Brown, S.S. and J.A. Spudich, *Mechanism of action of cytochalasin: evidence that it binds to actin filaments*. Journal of Cell Biology, 1980. **88**: p. 487-491.
25. Forscher, P. and S. Smith, *Actions of cytochalasins on the organization of actin filaments and microtubules in a neuronal growth cone*. The Journal of Cell Biology, 1988. **107**: p. 1505-1516.

26. Potma, E., W. de Boeij, L. Bosgraaf, J. Reelofs, P. van Haastert, and D. Wiersma, *Reduced protein diffusion rate by cytoskeleton in vegetative and polarized Dictyostelium cells*. Biophysical Journal, 2001. **81**: p. 2010-2019.
27. Dent, E.W. and F.B. Gertler, *Cytoskeletal dynamics and transport in growth cone motility and axon guidance*. Neuron, 2003. **40**(2): p. 209-27.
28. Solnica-Krezel, L. and W. Driever, *Microtubule arrays of the zebrafish yolk cell: organization and function during epiboly*. Development, 1994. **120**(9): p. 2443-55.
29. Campbell, D.S. and C.E. Holt, *Chemotropic responses of retinal growth cones mediated by rapid local protein synthesis and degradation*. Neuron, 2001. **32**(6): p. 1013-26.
30. Gallo, G. and P.C. Letourneau, *Regulation of growth cone actin filaments by guidance cues*. J Neurobiol, 2004. **58**(1): p. 92-102.
31. Westerfield, M., *The Zebrafish Book*. 1993, Eugene: University of Oregon Press.
32. Koppel, D.E., D. Axelrod, J. Schlessinger, E.L. Elson, and W.W. Webb, *Dynamics of fluorescence marker concentration as a probe of mobility*. Biophys J, 1976. **16**(11): p. 1315-29.
33. Brown, E.B., E.S. Wu, W. Zipfel, and W.W. Webb, *Measurement of molecular diffusion in solution by multiphoton fluorescence photobleaching recovery*. Biophys J, 1999. **77**(5): p. 2837-49.

## **Chapter 6: Conclusions**

### **6.1 Thesis Summary**

This thesis has described experiments to quantitatively measure fundamental intracellular transport characteristics, including active microtubule transport of endosomes and passive cytoplasmic diffusion of protein molecules. Our work has specifically involved examining the endosomal transport of non-viral DNA polyplexes from the cell membrane towards the nucleus. Characterization of the kinetics of this process reveals that there are two regimes of transport – a highly processive, directed motion that lasts up to ten seconds, and a more random motion for longer times. Both regimes are dependent on microtubule motors. Multiple particle tracking of the individual trajectories of polyplexes reveals that the results can be described using a model that accounts for both the thermal bending motions of the microtubules themselves and the force generation capacity of the kinesin and dynein motors.

We have additionally examined the internal pH characteristics of these polyplex-loaded endosomes as they travel through the cytoplasm. The specific pH characteristics of each type of polyplex strongly depend on the buffering capacity of the polymer used in the complex. However, we found that delivery efficiency is not correlated to buffering capacity and that PEGylation of the polyplexes does not affect buffering capacity. This contradicts the hypothesis that the ability of a polyplex to buffer pH changes leads to greater transfection efficiencies.

Finally, we have quantified free diffusion of GFP molecules in growth cones of neurons of the post-optic commissure (POC) in the developing zebrafish embryo using multi-photon FRAP. We found significant differences in GFP diffusion rate among

leader, follower, and off-tract follower growth cones; these differences were abolished by depolymerization of the actin network. Furthermore, direct labeling of actin-YFP in these growth cones revealed that the recovery fraction in leaders was greater than for followers, lending further support to the idea that there is greater turnover of the actin network in leaders. These data indicate that differences in diffusion rate may serve as a mechanism for amplifying local guidance signals or signal response, which would ultimately control nervous system wiring and development.

## **6.2 Future Directions**

The studies described in this thesis elicit a number of followup questions and experiments that would further illuminate the dynamics of cytoplasmic processes and the cytoskeleton. Four such experiments are described below; exploring these issues will further our understanding of these complex systems.

We first began by exploring the nature of cytoplasmic transport of polyplex-loaded endosomes in HeLa cells and found that such transport appeared like a random process. However, it is known that other endosomally transported objects, such as viruses, do not exhibit such behavior. One potential question is to explore the differences between viruses and non-viral vectors that result in this differential in transport. It is thought that surface proteins on the virus can modulate the transport process; for example, Suomalainen et al. have shown that adenoviruses can directly engage the dynein motor [1]. If the factors that result in transport differences can be identified, then they can be added to nonviral systems to improve gene delivery rates. Others have shown that ligands can be incorporated into the external surfaces of these polyplexes to achieve

specific cell-type targeting [2, 3]. Adding specific ligands that can directly engage the microtubule motors would likely reduce cell membrane-to-nucleus transit times.

A related issue is how viruses achieve such sensitive and specific gene delivery in target cells. One major problem of gene therapy is that the viral vectors currently used may potentially generate harmful immune responses in the patient, while the non-viral vectors experience significant barriers to delivery [4, 5]. We have shown that pH buffering may not be as significant a barrier as previously believed, but the main barriers to efficient delivery still remain unknown. Once polyplexes are unpackaged in the cytoplasm, the DNA is subject to degradation if it cannot get to the nucleus rapidly. Strategies to improve rates of DNA unpackaging and delivery to the nucleus will be necessary in order for such nonviral vectors to be viable for gene therapy.

Understanding the mechanisms of coupling among the different microtubule-mediated motors as they transport cargo within the cell is another area for exploration. How do different motors along a given endosome communicate with each other? Recent studies have identified the presence of the factors dynactin and Klarsicht that likely regulate the activities of the motors; for example, when kinesin is active, dynein is silenced [6, 7]. However, the question of how multiple kinesins or dyneins coordinate to move in a given direction remains unresolved [8]. Experiments and calculations indicate that even one motor is sufficient to transport a 500-nm-sized vesicle along the microtubule network [9]. Additional motors do not increase the maximum speed. There must be some mechanism to coordinate the activities of these motors. Further studies in this area would involve potentially expressing the putative factors *in vitro* and then adding them sequentially to a solution and determining which ones were necessary for

motor coupling or perhaps expressing CFP fusions of the different factors along with YFP-kinesin/dynein within the cell and examining the colocalization and FRET signals. By using fluorescence resonance energy transfer, we can probe the nanoscale dynamics and interactions of these proteins.

Finally, there are a number of potential experiments to further explore our exciting findings in developing zebrafish growth cones. The first issue is to track the kinetics of specific guidance molecules and determine how they interact with the growth cones *in vivo* as neuronal development progresses. Thanks to recent advances in imaging technologies, receptor clusters or even individual receptors can be visualized with high spatial and temporal resolution [10]. The growth cones grow based upon these guidance cues; it would be interesting to note the differences in interactions between leaders and followers, the relevant time scales of such interactions, and any kinetic changes such as receptor insertion or removal from the cell membrane. For example, a recent study has indicated that RhoA and Sema3A are important molecules for maintaining the axonal actin cytoskeleton and allowing pathfinding [11], and another indicates that Engrailed-2 (En-2), a homeodomain transcription factor that can be internalized by axons, modulates local protein synthesis and axon guidance [12].

We have shown that the actin cytoskeleton may play an important role in modulating internal diffusion kinetics in leader versus follower growth cones. It would be interesting to look at the ultrastructure of the growth cone using electron microscopy and determine the distribution and arrangement of actin filaments in this confined structure. Perhaps differences in the actin network between leaders and followers can be directly visualized using EM reconstruction. Additionally, it would be quite useful to

determine which other intramolecular factors play a role in modulating the noted diffusion differences. Perhaps certain actin binding proteins are more active in leaders than followers, and they keep the actin structure relatively more stable compared to followers. This would allow for slower filopodial kinetics, which has already been demonstrated, and for less rapid turnover of actin. Probing the kinetics of these processes would help improve our understanding of the dynamics of neuronal growth and function.

### **6.3 Concluding Remarks**

It is clear that we need more information about the biophysical mechanisms of cellular processes in order to better elucidate and predict the behavior of such systems. Issues such as cytoplasmic crowding and transport mechanisms and rates are critical for understanding how cells regulate internal conditions and how perturbations might affect their functioning; such results are applicable to fields as diverse as gene therapy or systems biology. In this work we have begun some explorations into aspects regarding protein diffusion and microtubule-mediated endosomal transport in crowded environments, though much remains to be discovered. The results reported here provide a good stepping stone towards a more complete understanding of the mechanics of the cytoskeleton and its role in cellular homeostasis.

## 6.4 References

1. Suomalainen, M., M.Y. Nakano, S. Keller, K. Boucke, R.P. Stidwill, and U.F. Greber, *Microtubule-dependent plus- and minus end-directed motilities are competing processes for nuclear targeting of adenovirus*. J Cell Biol, 1999. **144**(4): p. 657-72.
2. Bellocq, N.C., S.H. Pun, G.S. Jensen, and M.E. Davis, *Transferrin-containing, cyclodextrin polymer-based particles for tumor-targeted gene delivery*. Bioconjug Chem, 2003. **14**(6): p. 1122-32.
3. Popielarski, S.R., S.H. Pun, and M.E. Davis, *A nanoparticle-based model delivery system to guide the rational design of gene delivery to the liver. 1. Synthesis and characterization*. Bioconjug Chem, 2005. **16**(5): p. 1063-70.
4. Luo, D. and W.M. Saltzman, *Synthetic DNA delivery systems*. Nat Biotechnol, 2000. **18**(1): p. 33-7.
5. Schaffer, D.V., N.A. Fidelman, N. Dan, and D.A. Lauffenburger, *Vector unpacking as a potential barrier for receptor-mediated polyplex gene delivery*. Biotechnol Bioeng, 2000. **67**(5): p. 598-606.
6. Gross, S.P., M.A. Welte, S.M. Block, and E.F. Wieschaus, *Coordination of opposite-polarity microtubule motors*. J Cell Biol, 2002. **156**(4): p. 715-24.
7. Welte, M.A., *Bidirectional transport along microtubules*. Curr Biol, 2004. **14**(13): p. R525-37.
8. Mallik, R. and S.P. Gross, *Molecular motors: strategies to get along*. Curr Biol, 2004. **14**(22): p. R971-82.
9. Howard, J., *Mechanics of Motor Proteins and the Cytoskeleton*. 2001, Boston: Sinauer Associates.
10. Dahan, M., S. Levi, C. Luccardini, P. Rostaing, B. Riveau, and A. Triller, *Diffusion dynamics of glycine receptors revealed by single-quantum dot tracking*. Science, 2003. **302**(5644): p. 442-5.
11. Wu, K.Y., U. Hengst, L.J. Cox, E.Z. Macosko, A. Jeromin, E.R. Urquhart, and S.R. Jaffrey, *Local translation of RhoA regulates growth cone collapse*. Nature, 2005. **436**(7053): p. 1020-4.

12. Brunet, I., C. Weinl, M. Piper, A. Trembleau, M. Volovitch, W. Harris, A. Prochiantz, and C. Holt, *The transcription factor Engrailed-2 guides retinal axons*. *Nature*, 2005. **438**(7064): p. 94-8.